Experimental Characterization of Flow Dynamics of Pulsed-Chemical Vapour Deposition

Silviu I. Baluti

A thesis submitted in partial fulfilment
of the requirements for the degree of
Master of Engineering
in
Mechanical Engineering
at the
University of Canterbury,
Christchurch, New Zealand.
15 April 2005

Acknowledgements

Eighteen months of long hours work is now contained into this tome. It was fulfilled with the support of people involved with it either directly, or indirectly. They are those to whom I dedicate this thesis.

My thanks and gratitude to my thesis advisor, Dr. Susan Krumdieck. You helped me with the scientific work, and have always been there to solve issues related to my course study and experimental work. I was impressed by your knowledge, sense of humour and diplomacy. Hope you are pleased with the amount of work done during this period and its quality. Thank you for organising the research and for insuring the funds required to finalise my bit of work.

Regards to my course lecturers Dr. Alan Tucker and Dr. Pat Jordan. I will remember what you've taught me, not just thermodynamics and fluid dynamics principles.

My old friend Leo Markus. Thank you for the help during my most difficult period here. Thank you for helping me to crack-down on the analytical models. I've learned from you great deal of scientific things, and what real life and friendly support are about.

I have to thank my family, my patience wife and children that spent an impressive amount of time without me around. You had to wait me coming late at night, after long days of struggle with theoretical flow dynamics and vacuum theory concepts, or stubborn experiments. You always trusted me, and can see now that your trust wasn't in vane.

The laboratory technicians and workshop tradesmen, thanks for helping me making things work.

To my friends Gwenda, Graham, Lindsey and Mary Ellen. Thank you for the help during this one year and a half. Hope I'll return at least part of it.

Contents

List of figures

List of tables

Abstract

This research is a study of the precursor mass transport, the first variable that affects the film deposition rate, uniformity, coverage, and microstructure of resulted films on substrates inside Chemical Vapour Deposition (CVD) reactors. The Pulsed-CVD reactant flow field uniformities in pulse flow were compared to equivalent steady flow regimes. For mass limited transport CVD processes this represents an important matter, as precursor flux increase leads directly to increased deposition rates.

The objective of the research was to develop design relations and define operational parameter ranges to achieve flow field uniformity through experimental investigations.

Metered gaseous N_2 reactant quantities were injected at equal time intervals into the continuously evacuated reactor. The resulting reactor pressure cycle crosses all the three pressure flow regimes, from viscous, to transition and finally to molecular flow. Non-dimensional flow parameters for this unique pulse pressure flow regime were developed from first principles and were studied for relation to design and operation of Pulsed-CVD equipment and processes.

Because of the reactor low pressures and non-steady conditions, temperature induced buoyancy driven flows have low effect on the flow field dynamics of the gaseous N_2 flow (low Grashof number). Thus this research into pulsed pressure flow field uniformity was conducted for isothermal reactor conditions, without the heater powered.

For the reactor flow field uniformity determination, the naphthalene sublimation technique has been employed. This method is usually employed in viscous flow for the determination of the convective heat transfer coefficient through the heat and mass transfer analogy. In this research a method was developed to use the sublimation rate of several samples placed at different locations in the reactor volume to measure the relative convective and pressure conditions, and thus the uniformity of the reactor flow field.

Experiments have been run by subsequently varying the pulsing cycle length, the reactor pressure (implicitly the injected reactant mass), and the deposition substrate geometry. The rest of the deposition variables have been kept constant.

The experimental results show that cycle time greater than or equal to four times the reactor molecular time constant lead to best pulse flow uniformities, and that for these cycle times the 3D flow field uniformities in pulse flow regimes are always better than in equivalent steady flow ones. Comparable uniformities in both flows between stacked wafer substrates have been determined, with slightly better uniformities in pulse flow than in equivalent steady flow experiments.

In order to determine the steady flow field uniformities inside the experimental reactor, as well as when varying its geometrical characteristics, the gas flow was simulated using the finite volume Computational Fluid Dynamics (CFD) method and the commercial software Fluent 6.1.

Design and process parameters are proposed, and the reactor pressure is analytically modelled for the pulse flow regime.

Chapter 1

Introduction

1.1 Thin films applications and materials

“Chemical Vapor Deposition (CVD) is a synthesis process in which the chemical constituents react in the vapor phase near or on a heated substrate to form a solid deposit” [5, p. 2].

CVD processing is a major technical area that is continuously developing, including new materials, technologies, and equipments. Products are being studied and developed at an impressive rate given the fact that there is almost no modern activity that won’t make use of the thin film products obtained through this technique.

The main application of CVD technology is the production of semiconductors and related electronic components: conductors, insulators and diffusion barriers. It comprises three quarters of total CVD production.

Other CVD applications include the optoelectronic and ferroelectric, optical, wear and corrosion-resistant, cutting–tool applications, fiber, powder and monolithic.

Most elements in the periodic table are used in the preparation of the CVD precursors, in the endeavour of obtaining best film characteristics at low prices, with minimum technology associated risks.

The range of deposited materials and their applications using the CVD technique are almost limitless. Even deposition of pure metals is reported. A comprehensive list of these applications can be found in appendix A.

1.2 Pulsed-CVD process summary

Deposition of thin film materials in high technology industrial applications is done by using either Physical Vapour Deposition (PVD) or CVD systems. Actual industrial CVD reactors function in steady pressure regimes, with the reactants being transported to the deposition surface (substrate) by diffusion through a continuous flow of carrier gas. These are steady pressure CVD reactors that work either at atmospheric pressure (APCVD) where high film growth rates are achieved but film uniformity and microstructure control are a challenge, or at low pressures (LPCVD) where low growth rates and good uniformities are achieved. Low conversion efficiencies are a problem in both these types of systems.

Small scale research reactors in which the source reactants (precursors) are pulsed into the steady flow carrier gas have also been developed [25-28], but these are steady pressure CVD reactors as well.

The Pulsed-CVD reactor conditions are unique to the CVD technology. In this new technique, metered reactant quantities are injected at equal time intervals in a continuously evacuated reactor. The new Pulsed-CVD combines the fore- mentioned positive characteristics, achieving, by cyclic forward and backwards pressure variation, high film growth rates and conversion efficiency with good deposition uniformity, composition and microstructure control. Not only does Pulsed-CVD offer optimum uniformities at the horizontal substrate level, but this study experimentally proves that the reactor pulse 3D flow field uniformities are almost 100 % better than the equivalent steady flow field uniformities. It is also known from previous research [21, 22] that under optimal deposition conditions the system reaches conversion efficiencies of over 90%, and that the microstructure control is comparable to that of LPCVD systems.

The second interest in Pulsed-CVD is the possibility of its industrial scaling. Given the viscous flow fields at the substrate, none of the currently used CVD reactors can be designed and industrially scaled. For each of these systems an important amount of time and computational fluid dynamics work is required in order to obtain desired film uniformities and morphologies, each piece of industrially used equipment being individually developed. For the Pulsed-CVD, dimensionless reactor design and process control parameters are proposed.

The technical innovation introduced by the Pulsed-CVD system is the fact that it alternates the introduction of a large precursor vapour dose in the reactor at the beginning of pulse cycle injection times, followed by reaction product evacuation. This gives the ad-atoms in the film sufficient residence time to equilibrate to the substrate surface during the pulse cycle pump-down period. This physical characteristic offers the Pulsed-CVD process the unique advantage of high deposition rates at very good film uniformity.

Added to the pulsed pressure, another system novelty is the ultrasonic nozzle whose power and timing are computer controlled, and which during the deposition process produces very fine precursor droplets (15 μm diameter) that rapidly evaporate at the low reactor pressure. This gives the Pulsed-CVD system the advantage of not needing the carrier gas flow to transport the precursor vapours to the reactor.

During each pressure cycle the precursor flow inside the reactor crosses all three pressure flow regimes, from viscous flow at high injection pressures, to transition flow during the evacuation of the reactor, and finally to molecular flow at the end of the evacuation period at pressures close to the reactor ultimate pressure.

The Pulsed-CVD reactor pressure time variation curve is represented in figure 1.1. In the dynamic systems theory [14], they are called stable limit cycles.

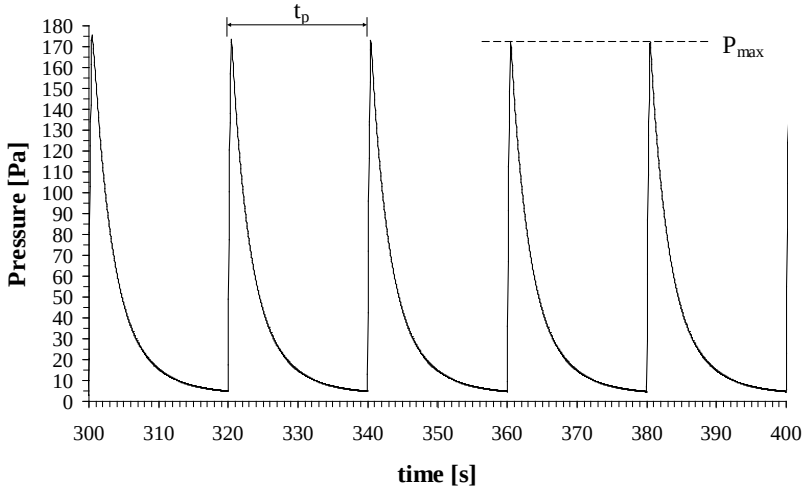

Figure 1.1 Stable limit pulse flow cycles

The three Pulsed-CVD process variables are the cycle time t_p, the cycle maximum pressure P_{max} and the reactor/heater geometries. Experiments were cared to investigate flow uniformity as function of these parameters.

During normal functioning, the injected vapour molecules are deposited on the substrate that lies on the top of a heater installed at the reactor base or on stacked wafers through heat activated thermal decomposition of a precursor chemical compound.

A schematic overview of the reactor for single heater and stacked wafer configurations is represented in figure 1.2.

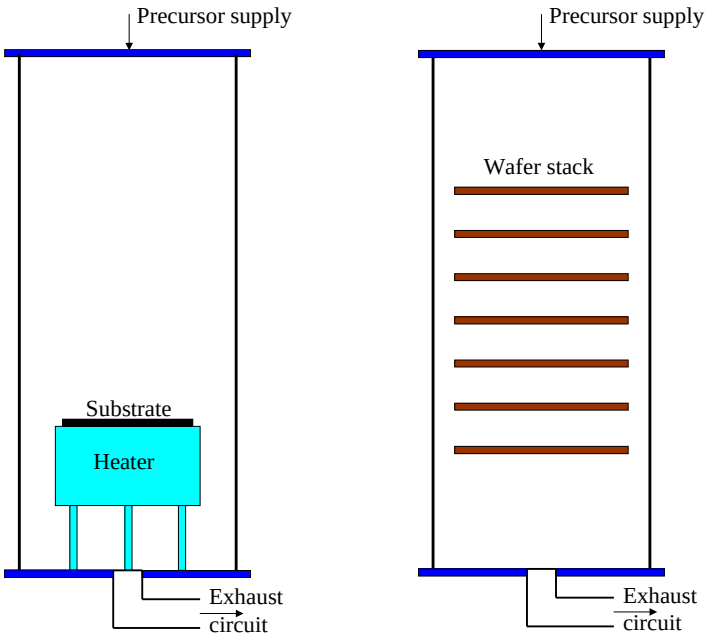

Figure 1.2 Schematic overview of the Pulsed-CVD process for single heater and stacked wafer configurations

This research studies the 3D flow field uniformity inside Pulsed-CVD reactors. The pulse experiments flow field uniformities are compared with the uniformities in equivalent steady flow regimes; that is comparing the flow uniformities when equal amounts of reactants are introduced inside the reactor either in pulse or steady flow. It is shown that the pulse flow 3D flow field uniformities are almost 100 % better than the ones in equivalent steady flow. The optimum cycle time in order to achieve the best flow uniformities is also determined. In addition, the flow field uniformities at substrates situated in horizontal parallel stacks are compared for the two flow regimes.

Besides proving that Pulsed-CVD can produce uniform mass transport at high flux rate, this research provides new insights into designing reactors by using proposed dimensionless design parameters. This will minimize industrial reactors design and scale-up time, thus lowering the production costs.

1.3 Research motivation

The overall purpose of this study is to compare the flow field uniformities during pulse flow and equivalent steady flow experiments, as well as the proposal of new reactor design and process parameters.

The steady flow field uniformities inside the experimental reactor, as well as when varying its geometrical characteristics, have been simulated using the finite volume CFD method.

The naphthalene sublimation technique has been employed to experimentally determine the flow field uniformities inside the reactor. Naphthalene ($C_{10}H_8$) sublimes at room temperature, has a low toxicity and good casting and machining properties. This technique is usually employed in viscous flow for the indirect determination of the convective heat transfer coefficient. It is used here as no flow visualization techniques like using TiO_2 smoke, interferometry, laser induced fluorescence (LIF), or other spectral excitation and adsorption techniques are possible for the Pulsed-CVD low pressures and are unsuitable to its unsteady conditions.

The research continues the work done by H. Raatz and Y. Lee. In their work [31], in order to see the liquid atomisation, they have injected fluorescent ethyl alcohol with water into the reactor, focused a strong light beam towards the injection and deposition areas and videotaped the process. The results were quite poor; especially bellow the injection zone, where the liquid droplets evaporated and the particles became too far apart to be seen. They also concluded that schlieren methods would not give more conclusive results, especially inside unsteady low-density gas flow.

The flow tagging visualisation techniques by adding foreign material to the flowing fluid can not be applied in unsteady flows. “These methods give excellent results in stationary flows,

but the errors can be enormous for unsteady flows, owing to the finite size of the particles." [34, pp. 2, 3].

The low-density flows can be visualized with methods using the radiative characteristics of some gases. The direct radiation allows visualization of flow fields at a density which is one or two orders of magnitude below the sensitivity limit of a schlieren system.

A first method would be the gas molecules excitation by electron beams. In this method the electron beam must be moved with constant speed through the gas flow. This only can be done in steady flows. Also, the electron beam technique remains a qualitative method, "allowing one just to discriminate between regimes of reduced or increased gas density" [34, p. 243].

The electric glow discharge can be used in a certain gas density range, where "the emitted light intensity increases with the number of exciting collisions, and therefore, with the level of the gas density. This however holds up to a particular value of the gas density where the free path length of the electrons becomes too small, and the electrons gain insufficient energy between collisions for excitation" [34 – p.245]. The method is similar to the previous one and can not give a quantitative data interpretation.

The naphthalene film thickness technique can be used for uniformity determination on flat surfaces, not for 3D flow uniformity interpretation. Even more, given that the boundary conditions of thin film mass transfer are not exactly similar once the clear patches appear, the initial isothermal condition is not satisfied anymore since the clear patches are adiabatic and lead to errors in the mass transfer data.

A measurement method was developed in previous research [31] involving casting of small (10 mm diameter, 14 mm high), smooth naphthalene cylinders. During experiments, six of these cylinders have been hung on a thin stainless steel wire frame or in between wafer stacks. The flow uniformities have been determined by comparing the cylinders specific sublimations for the duration of each experiment. The experimental apparatus set-ups and experimental procedures, as well as the analytical equations for the uniformity calculation and the Pulsed-CVD reactor pressures are detailed in dedicated chapters.

1.4 Thesis organization

The thesis is organised into chapters for background, theory, experimental and results. Chapter 2 gives background on current CVD processing, focusing on the critical parameters for high quality and low cost. Chapter 3 shows the theory behind the flow field measurement method. Chapter 4 contains the experimental apparatus description. Chapter 5 details the experimental method. Chapter 6 presents the theoretical background of the Pulsed-CVD. In Chapter 7 the reactor time constant is determined both analytically and experimentally. The naphthalene samples uniformity and uniformity error analysis are given in Chapter 8. Chapter 9 contains the pulse cycle pressures analytical model development. CFD simulations and results are included in Chapter 10. Chapter 11 gives the experimental data interpretation. In Chapter 12 research conclusions and future work are included.

Chapter 2

CVD technology background

This chapter presents the principles of CVD systems used in thin film deposition for industrial applications, their characteristics, and the main steps of the thin films deposition process. Emphasis is on the reactant transport to the substrate, as this is what determines the reactor flow field that makes the subject of this research. At the end of the chapter, the CVD technology advantages and disadvantages are summarized.

2.1 CVD processes

“CVD methods are among the most versatile deposition techniques because a wide range of chemical reactants and reactions can be used to deposit a large number of different types of films for a wide range of applications” [7, p.1-24].

The CVD systems are divided into thermal CVD, plasma enhanced CVD, laser and photo CVD, chemical vapour infiltration (CVI), and fluidized bed CVD. The thermal CVD systems used in industry are presented, as this study was done on a CVD system of this type. No reference is made to the rest of the systems, other than saying that technical improvements brought by Pulsed-CVD technologies would equally apply to the transport processes in any CVD system.

CVD equipment should be capable to:

1. Deliver metered reactant quantities to the substrate
2. Raise the substrate temperature to the chemical reaction required temperature
3. Evacuate reaction products and depleted gases

The thermal CVD systems can be divided into hot-wall and cold-wall reactors.

In cold-wall reactors the substrate is directly heated by induction or radiant heating. The rest of the reactor remains cool, so that the reactor walls remain uncoated during the deposition process. Figure 2.1 is a schematic representation of the pancake cold-wall reactor.

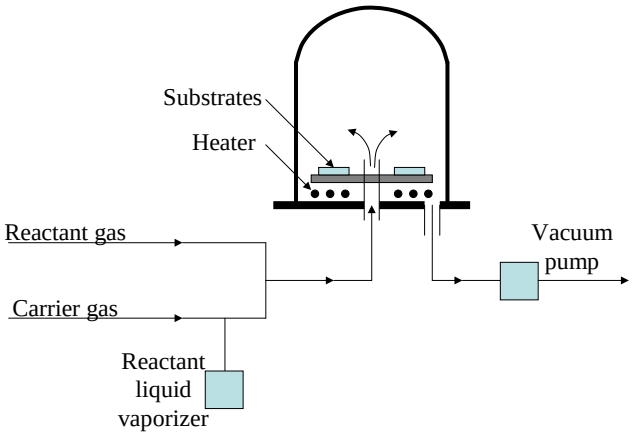

Figure 2.1 Pancake cold-wall CVD reactor

The temperature in hot-wall reactors can be easily controlled, but deposition occurs inside the reactor walls as well as on the substrates. Figure 2.2 shows the horizontal and the barrel hot-wall reactors. Observe that the susceptors are tilted towards the gas inlet. This is a common practice in steady flow reactors; it is employed in order to achieve equal boundary layer thicknesses above all deposition wafers, thus uniform deposited films.

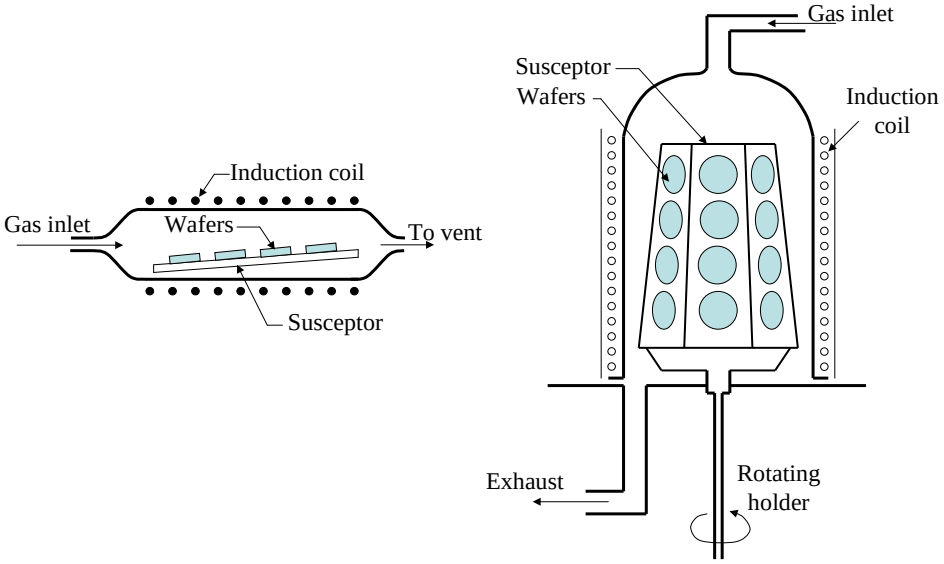

Figure 2.2 Horizontal and barrel steady flow, hot-wall CVD reactors

A second division can be made if considering the constant pressures the steady flow CVD reactors are working at. There are two categories: atmospheric and low pressure CVD reactors. The reactants and reaction products diffuse through the boundary layers. In LPCVD reactors the deposition quality is improved, with better uniformity and step coverage. Also, in LPCVD the stoichiometry and contamination control are improved, and fewer pinhole defects are detected. Another advantage is that inside the LPCVD reactor the deposition wafers can be stacked more densely than inside the APCVD reactor; batches of one hundred wafers or more can be processed at the same time.

2.2 CVD kinetics and mass-transport mechanisms

CVD reactions must be both thermodynamically and kinetically favourable. Part of the CVD kinetics of interest in this study is the influence of total gas flow rate on the formation rate of the solid reaction product (the thin film). In order to properly understand how this parameter is affecting the deposition rate, a brief explanation of the CVD kinetics and mass-transport mechanisms is necessary.

Most of the CVD deposition reactions are heterogeneous, and the overall deposition rate is controlled by the slowest of the eight concerned processes.

Figure 2.3 is the schematic representation of these processes in a steady flow reactor:

1. Reactant transport close to the substrate
2. Reactant diffusion (boundary layer mass transport) to the substrate
3. Reactant adsorption to the substrate
4. Surface chemical reaction (dissociation)
5. Surface diffusion (migration) and lattice incorporation
6. Reaction gaseous product desorption
7. Product diffusion (through the boundary layers) away from the substrate
8. Product evacuation (transport outside the deposition zone) through the gas carrier flow

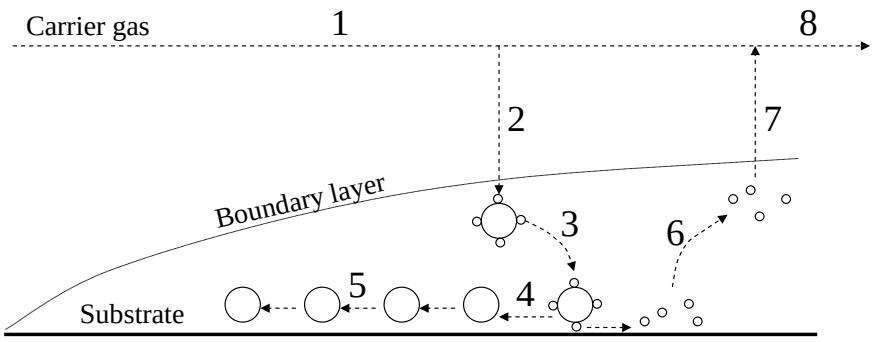

Figure 2.3 CVD kinetics in steady flow CVD reactors

In the steady flow CVD systems, the reactant mass transport is achieved by convection using a steady flow carrier gas. For pressures higher than 1 kPa this generates, in most of the typical size steady flow CVD reactors, a viscous flow regime. In this flow regime gas flow velocity gradients appear with the formation of non-uniform boundary layers. This strongly affects the reactant diffusion through it, with associated influences on the deposited film uniformity. Because the reactants and the products must pass through the boundary layer, low values of the boundary layer thickness are desirable.

Uniformity is the major reason the steady flow LPCVD reactors have been developed; even if the film growth rate decreases, the film uniformity is much improved as reactant diffusion is made through much thinner and uniform boundary layers given the reactant gas flow development in transition and molecular flow regimes. Gaseous diffusion is improved here by the low reactor pressure values as well.

Good film uniformities at high growth rates can not be achieved in most conventional CVD systems. Optimization of film deposition requires a good understanding of the gas transport in these reactors. This involves major work spent with CFD simulations in each one of the industrial APCVD or LPCVD steady flow reactors.

Pulsed-CVD is different; here the reactants are injected in metered quantities inside the reactor at equal interval times, through an ultrasonic nozzle that transforms the liquid reactant into a mist of very fine droplets, with average diameters of 15 μm that evaporates in less than 5 μs when entering the reactor vessel [17, 19].

In Pulsed-CVD reactors the boundary layers that form at the substrate surfaces are thin. This is one reason why the films deposited by this technique have good uniformities (another reason is the flow field uniformity, as will be shown in this research). Also, by injecting sufficiently high amounts of reactant, high growth rates can be achieved.

2.3 CVD technology - advantages and disadvantages

Given the important capabilities of the CVD, it is used, as shown in introduction, in an extremely large number of industrial applications. The CVD technology main advantages are:

1. Produces adherent, high density pure films with good covering characteristics; good step coverage, coverage of small 3D substrates
2. Cheaper than the PVD processes when high film growth rates are required
3. Adaptation to different deposition processes and reactants

However, the steady flow CVD systems are not perfect. Their main disadvantages are:

1. The high temperatures the substrates must be heated for the chemical reaction to take place (over 600 ^{0}C)
2. Toxic and/or hazardous reactants or products
3. Low conversion efficiencies
4. Film uniformity and growth rates problems

Many of these disadvantages are solved by the Pulsed-CVD. They are related to the film uniformities and growth rates, that are directly related to the substrate temperature uniformity and reactor flow field; conversion efficiency, studied in previous work [21, 22]; as well as the reactant and product toxicity, problem solved by making use of metal organic precursors.

2.4 Conclusion

None of the actual CVD technologies can totally overcome the deposition film uniformity issues at the same time with the film growth rates and film uniform deposition on large 3D

substrates. The industrial CVD technology can be improved by making use of Pulsed-CVD reactors not only by reducing the deposition costs, but also by overcoming many of the steady flow CVD reactors, the APCVD high film growth rates and the LPCVD good film uniformities, in order to produce lees expensive films with controllable morphologies. By developing and better understanding the Pulsed-CVD theoretical principles, an industrially scalable system can be obtained. Not only that, but the technical innovations included into the Pulsed-CVD will allow uniform film depositions with very good growth rates on large 3D substrates. This hasn't been achieved with any other previous CVD technology.

Chapter 3

Flow field measurement

3.1 Theoretical background

The heat and mass transfer analogy theory [11] offers the connection between the convection heat transfer coefficient h and the convection mass transfer coefficient h_m. This can be deduced from the thermal and concentration boundary layers normalized equations.

The dimensionless variables are defined as:

$$x^* = \frac{x}{L};\ y^* = \frac{y}{L};\ u^* = \frac{u}{V} \text{ and } v^* = \frac{v}{V} \tag{3.1}$$

where x and y are the position coordinates in the boundary layer, L is the boundary layer characteristic length (i.e. the length of a flat plate), u and v are the parallel and normal flow direction fluid velocities, and V is the fluid velocity upstream of the surface. Bulk fluid temperature and concentration boundary conditions are used for dimensionless dependent variables:

$$T^* = \frac{T - T_S}{T_\infty - T_S} \text{ and } C_A{}^* = \frac{C_A - C_{A,S}}{C_{A,\infty} - C_{A,S}} \tag{3.2}$$

with T_S / T_∞ the surface/free stream (bulk fluid) temperatures, and C_{AS} / $C_{A\infty}$ the surface/free stream species A concentrations. The simplified forms of the energy and species continuity equations (for the steady two dimensional flow of an incompressible fluid with constant properties) are given as:

$$u\frac{\partial T}{\partial x} + v\frac{\partial T}{\partial y} = \alpha\frac{\partial^2 T}{\partial y^2} + \frac{\nu}{c_p}\left(\frac{\partial u}{\partial y}\right)^2 \tag{3.3}$$

$$u\frac{\partial C_A}{\partial x}+v\frac{\partial C_A}{\partial y}=D_{AB}\frac{\partial^2 C_A}{\partial y^2} \tag{3.4}$$

The viscous dissipation in the last term of equation 3.3 can be neglected for non-sonic or high-speed motion of lubricating oils flow. The term $\alpha = k_f /\rho c_p$ is the fluid thermal diffusivity with k_f the fluid thermal conductivity, $\nu = \mu /\rho$ is the fluid kinematic viscosity with μ the fluid dynamic viscosity, and D_{AB} is the binary diffusion coefficient. The following thermal and concentration boundary layer dimensionless equations can be deduced:

$$u^*\frac{\partial T^*}{\partial x^*}+v^*\frac{\partial T^*}{\partial y^*}=\frac{\alpha}{VL}\frac{\partial^2 T^*}{\partial y^{*2}} \tag{3.5}$$

$$u^*\frac{\partial C_A{}^*}{\partial x^*}+v^*\frac{\partial C_A{}^*}{\partial y^*}=\frac{D_{AB}}{VL}\frac{\partial^2 C_A{}^*}{\partial y^{*2}} \tag{3.6}$$

By replacing in equations 3.5 and 3.6 the Reynolds, Prandtl and Schmidt numbers:

$$\mathrm{Re}_L=\frac{VL}{\nu};\ \mathrm{Pr}=\frac{\nu}{\alpha};\ Sc=\frac{\nu}{D_{AB}},$$

the following equations result:

$$u^*\frac{\partial T^*}{\partial x^*}+v^*\frac{\partial T^*}{\partial y^*}=\frac{1}{\mathrm{Re}_L\,\mathrm{Pr}}\frac{\partial^2 T^*}{\partial y^{*2}} \tag{3.7}$$

$$u^*\frac{\partial C_A{}^*}{\partial x^*}+v^*\frac{\partial C_A{}^*}{\partial y^*}=\frac{1}{\mathrm{Re}_L\,Sc}\frac{\partial^2 C_A{}^*}{\partial y^{*2}} \tag{3.8}$$

It can be seen that the above equations have similar form advection (left-hand side) and diffusion (right-hand side) terms, so that the processes they describe are analogous.

By combining the previous equations with the Nusselt and Sherwood numbers relations:

$$Nu=\frac{hL}{k_f}=+\left.\frac{\partial T^*}{\partial y^*}\right|_{y^*=0} \tag{3.9}$$

$$Sh = \frac{h_m L}{D_{AB}} = + \left. \frac{\partial C_A *}{\partial y *} \right|_{y*=0} \tag{3.10}$$

from equations 3.7 and 3.9, and knowing that Nu is proportional to $P_r{}^n$, it results:

$$Nu = f(x*, \mathrm{Re}_L)\,\mathrm{Pr}^n \tag{3.11}$$

In the same manner, from equations 3.8 and 3.10, and knowing that Sh is proportional to $S_C{}^n$, the proportionality function for Sh number results:

$$Sh = f(x*, \mathrm{Re}_L) Sc^n \tag{3.12}$$

Equations 3.11 and 3.12 give, with equivalent functions $f(x*, \mathrm{Re}_L)$, the equation that relates the convection heat transfer coefficient h with the convection mass transfer coefficient h_m:

$$\frac{Nu}{\mathrm{Pr}^n} = \frac{Sh}{Sc^n} \Rightarrow \frac{hL/k}{\mathrm{Pr}^n} = \frac{h_m L / D_{AB}}{Sc^n} \tag{3.13}$$

By making use of the Lewis number relation, that represents the ratio of the thermal and mass diffusivities:

$$Le = \frac{\alpha}{D_{AB}} \tag{3.14}$$

the final relation between the two convection transfer coefficients, applicable both in laminar and turbulent flows, is:

$$\frac{h}{h_m} = \frac{k}{D_{AB} Le^n} = \rho \cdot c_p \cdot Le^{1-n} \tag{3.15}$$

Relation 3.15 offers the theoretical base for the convection heat transfer coefficient determination by employing the naphthalene sublimation technique in forced-convection flows.

The bulk gas flow past around the cylindrical naphthalene samples leads to their sublimation with naphthalene molecules being transferred to the gas stream, in the same way as heat would be transferred between the samples and the gas. Flow speed variations lead to different sublimation/heat transfer values.

Similar to the convective heat transfer equation derived from the energy equation for incompressible Newtonian fluids, the steady flow forced convective mass transfer equation is [33]:

$$v \cdot \nabla c = \alpha \cdot \nabla^2 c \tag{3.16}$$

where v is the flow velocity, and α is the diffusion coefficient.

In cylindrical coordinates, for a cylinder of radius r, having as axis parallel the coordinates system z axis (figure 3.1):

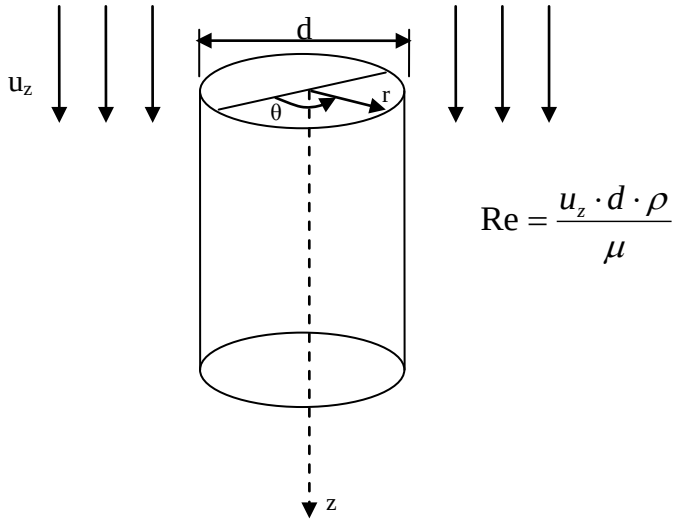

Figure 3.1 Naphthalene sample in cylindrical coordinates

equation (3.16) can be written:

$$u_r \frac{\partial c}{\partial r} + \frac{u_\theta}{r} \frac{\partial c}{\partial \theta} + u_z \frac{\partial c}{\partial z} = \alpha \cdot \left[\frac{1}{r} \frac{\partial}{\partial r} \left(r \frac{\partial c}{\partial r} \right) + \frac{1}{r^2} \frac{\partial^2 c}{\partial \theta^2} + \frac{\partial^2 c}{\partial z^2} \right] \tag{3.17}$$

For low Re numbers (where the convective mass transfer dominates over the diffusion mass transfer, with high Pe number), the concentration varies only in a thin layer adjacent to the naphthalene cylinder, and (giving that the traverse velocity occurring at the subliming surface is many orders of magnitude smaller than the nitrogen flow velocity on the z direction) only the concentration gradient normal to its lateral surface is important. This reduces equation (3.17) to:

$$u_z \frac{\partial c}{\partial z} = \alpha \frac{\partial^2 c}{\partial z^2} \tag{3.18}$$

Although not needed in this research, the mass convection coefficient h_m can be determined by using the experimentally determined specific cylinder sublimation rate:

$$\frac{\dot{m}}{A_S} = h_m (c - c_\infty) \tag{3.19}$$

where A_S is the cylinder external area, and c_∞ is the naphthalene concentration in the nitrogen flow stream. The mass convection coefficient is a non-linear function of the Re number $h_m = f(\mathrm{Re})$.

The heat and mass transfer analogy is valid for buoyancy-driven flows as well. However, the naphthalene samples must be exposed to isothermal conditions as sublimation is a strong function of temperature.

3.2 Naphthalene method for Pulsed-CVD

During each experiment a number of six naphthalene cylindrical samples of 10 mm diameter and 14 mm height have been used.

The samples have small dimensions and relatively large vertical distances between them. Numerical simulations showed that the fluid flow around the cylinders in steady flow doesn't influence the experimental results, as no flow shape variations from one cylinder to another have been detected (figure 3.2).

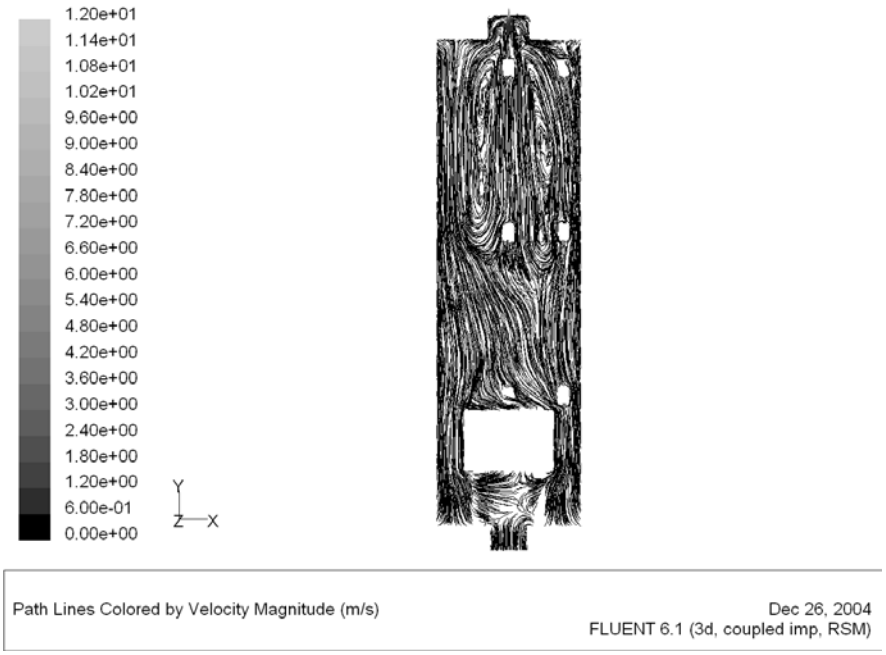

Figure 3.2 Reactor flow path lines around the six naphthalene cylinders

Flow field mass transport was investigated for both open reactor volume and stacked wafer configurations shown in figures 3.3 and 3.4. In all experiments the samples have been positioned in the reactor's symmetry plane. The figures also show the order (1-6) in which the cylinders have been measured and weighted.

The first arrangement in figure 3.3 was chosen so that the flow field uniformity inside the whole reactor volume, and implicitly at the heater top surface, would be determined.

In LPCVD reactors the deposition uniformities on wafers is a function only of the precursor diffusion from the bulk flow around the stack into the stagnant carrier gas between wafers in the stack. The velocities in between the wafers are considered to be equal and close to zero for steady flow condition. The diffusion controlled deposition process for stacked wafers is described [6, pp.296–309], by the dimensionless diffusion factor:

$$\phi = \sqrt{\frac{2r_0^{\,2}k}{\Delta D}} \tag{3.20}$$

For Ø > 0.2, the diffusion is rapid and the depositing species are uniformly distributed in the inter-wafers space. In equation 3.20, r_0 is the wafer radius, k is the chemical reaction rate-constant, Δ is the distance between the wafers, and D is the gas diffusivity.

In order to scale the experiment to represent a CVD process, the spacing for Ø > 0.2 was calculated for an orientative value of $k = 1.1 \cdot 10^{-3} m^3 / mole / s$ (which is the chemical reaction rate-constant for the nitrogen pent-oxide formation reaction $2NO_2 + \frac{1}{2}O_2 \rightarrow N_2O_5$). The gas diffusivity at temperatures of T = 273 K takes values between 0.1 cm^2/s to 10 cm^2/s, depending on the reactor pressure. The resulting dimension, calculated for reactor pressures from 0 to 100 Torr (0 to 13,332 Pa) for r_0 = 40 mm wafer radius, was Δ = 20 mm for the wafers interspaces.

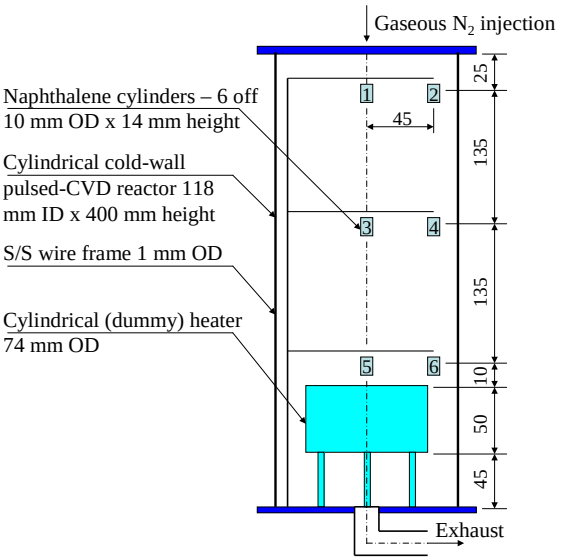

Figure 3.3 Naphthalene sample arrangement for open reactor volume flow field experiments (dimensions in mm)

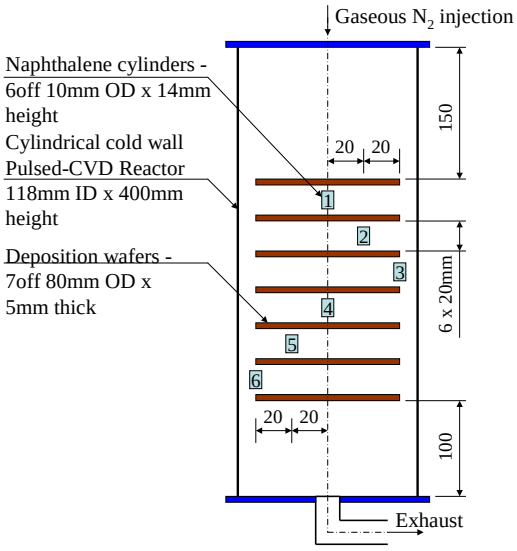

Figure 3.4 Naphthalene sample arrangement for stacked wafer experiments (dimensions in mm)

Pictures of the apparatus with the two different sample arrangements are presented in figures 3.5 and 3.6.

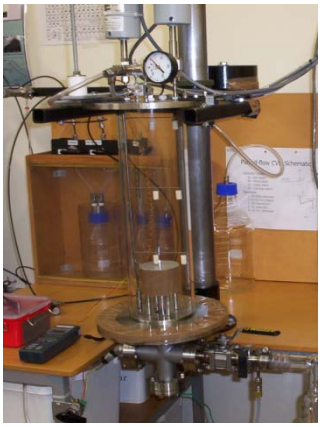

Figure 3.5 Naphthalene samples positioned on the wire frame

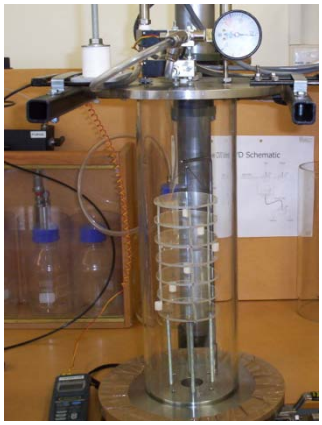

Figure 3.6 Naphthalene samples positioned between wafers

3.3 Naphthalene sublimation as a function of temperature and pressure

The naphthalene vapor partial pressure on the surface of the solid depends only on the temperature [23]:

$$\ln p_{nw} = c_1 + c_2 / T_w \tag{3.21}$$

where p_{nw} is the vapor partial pressure at the sublimating surface, c_1 and c_2 are two empirically determined constants, and T_w is the temperature at the sample surface. As an example, the naphthalene partial vapor pressure at a temperature of 20 ^{0}C, calculated for $c_1 = 31.23252$ and $c_2 = 8587.36$ is $p_{nw} \cong 6.85$ Pa.

The sublimation rates of naphthalene cylinder samples held at constant pressures in the reactor were determined by mass loss over 20 minutes. Experimental results showed that the sublimation rate asymptotically increases with the reactor pressure decrease. The highest values of the sublimation rates are reached at the reactor ultimate pressure, equal to the naphthalene vapor pressure when naphthalene samples are installed inside, as shown in figure 3.7.

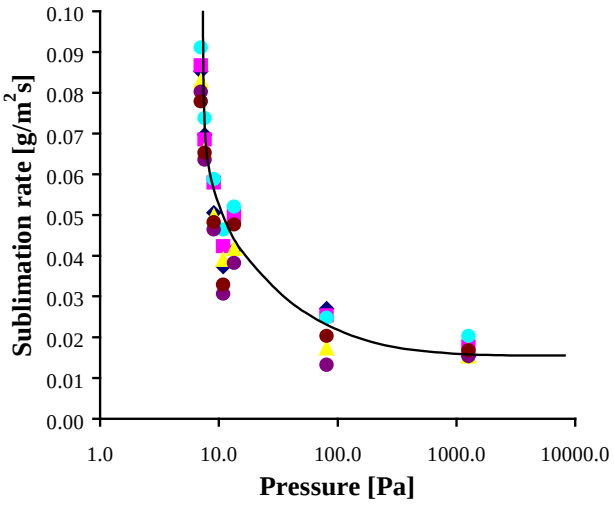

Figure 3.7 Naphthalene sublimation rate as a function of reactor pressure at nominal room temperature T = 20 ^{0}C (data by J-Y Lee)

The actual rate of naphthalene sublimation in separate experiments can not be compared, as the room/reactor temperatures and reactor pressures the experiments have been run were different. However, because during each one experiment all six samples are in the same pressure/temperature conditions, the comparable measure between different experiments is the naphthalene samples specific sublimation uniformity. The calculation method for uniformity is detailed in chapter 8. The reactor pressure uniformity is analytically demonstrated in chapter 10.

Chapter 4

Experimental apparatus

Experiments were run on two different experimental apparatus set-ups. The apparatus used during the first set of experiments (reactor volume flow field uniformity as a function of the pulse cycle length) was designed for Pulsed-CVD thin film depositions by using liquid precursors, and was manufactured previous to this research. As result, the reactor absolute peak pressures possible when injecting gaseous N_2 using the liquid delivery system were too low for comprehensive investigation, of less than 1 kPa. A picture of the liquid precursor apparatus, used during the open reactor volume flow field experiments, is presented in figure 4.1.

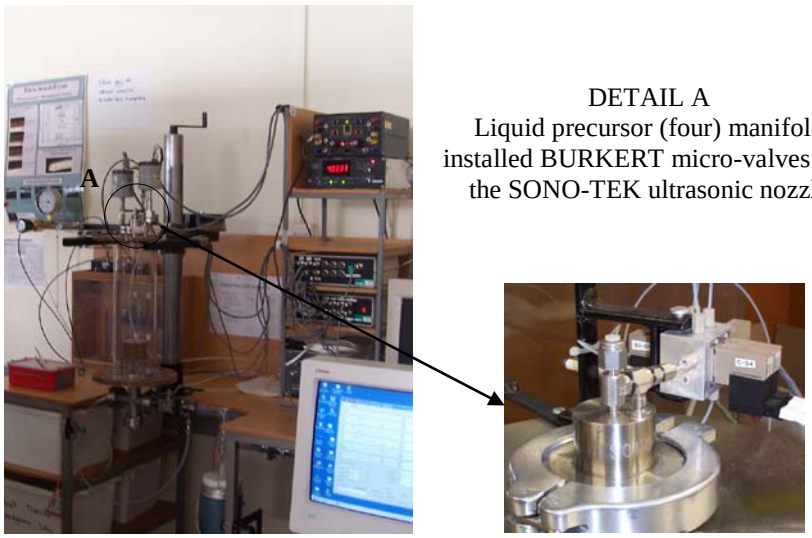

Figure 4.1 Picture of the liquid injection experimental apparatus (designed and built by J-Y Lee)

For the last two experimental sets (reactor volume flow field uniformity as a function of the pulse cycle maximum pressure, respectively the stacked wafer), in order to reach higher absolute reactor peak pressures, a new (gas injection) system was designed and built, providing for injection volume. The settings of the parameters for pulse control have been adapted in order to run experiments with gaseous N_2.

The four liquid precursor micro-valves have been replaced with two bigger gas injection valves connected with much larger ID tubes (6 mm instead of 0.8 mm).

The gas injection apparatus is shown in figure 4.2.

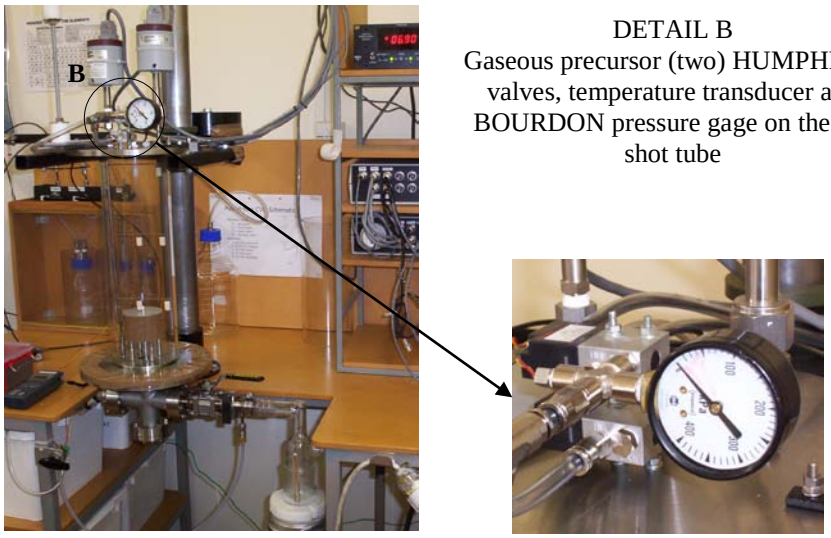

Figure 4.2 Picture of the gas injection experimental apparatus

4.1 Liquid injection apparatus system design

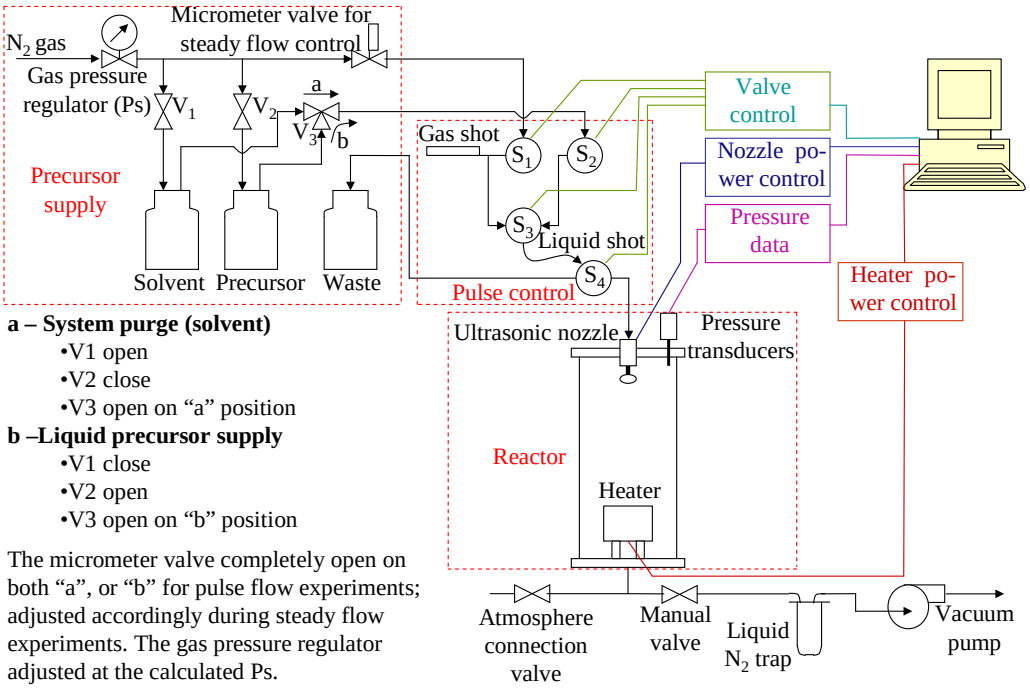

Figure 4.3 Liquid injection Pulsed-CVD apparatus set-up

Figure 4.3 is a schematic representation of the vertical Pulsed-CVD apparatus configured for liquid precursor injection. The system consists of five main parts:

a. Precursor supply
b. Pulse control
c. Reactor
d. Exhaust circuit
e. Data acquisition and control

Each of these subsystems components and their operation is described in the next sections.

4.2 Experimental apparatus components

4.2.a Precursor supply

The components of the precursor supply subsystem used during all gaseous N_2 injection experiments, either on the liquid or gas injection experimental apparatus set-ups, are:

1. Gas pressure regulator, TESCOM 442210 240

This is the manual regulator used to set the supply pressure to the pulse control valves during the pulse/steady flow experiments. It consists of a manual valve, which is attached to an atmospheric BOURDON mechanical gage that can measure pressures of up to 600 kPa.
The maximum gaseous N_2 supply gage pressure that can be set with the gas pressure regulator is of 400 kPa. This is also the maximum pressure to be run through the solvent and precursor bottles.

2. Micrometer valve

NUPRO stainless steel manual micrometer valve, used to adjust the supply pressure to the pulse control valves during the steady flow experiments. For the pulse flow experiments it remained continuously opened, with no local pressure drop between the gas pressure regulator and the solenoid valves.

3. Manual 2/3 way valves, V1-V3

SWAGELOCK stainless steel manual valves used to set the system operation in precursor supply mode, or system purge mode.

4. Liquid storage bottles

SCHOTT DURAN glass bottles each with a capacity of 500 ml, designed to store liquids under pressure. Provided with in-house designed stainless steel caps for adaptation to the connection fittings.

SWAGELOCK stainless steel fittings are used for the connections between the subsystem components.

The gas lines are made from Teflon tubes with an internal diameter of 2.5 mm.

4.2.b Pulse control

The pulse control subsystem consists of four BURKERT 6603/6604 micro-solenoid actuated - spring return, 3 way 2 positions valves. The micro-solenoids are supplied with a voltage of 24 VDC and have a power consumption of 1.5 W each, with a very good response time, of less than 20 ms.

Figure 4.4 BURKERT 6603/6604 micro-solenoid valve

The four micro-valves are installed on an in-house designed and manufactured aluminium manifold.

The manifold also includes the threaded connections for the fittings that connect the gas and liquid shot tubes, the precursor/solvent supply and the overflow to the waste.

The gas shot Teflon tube has dimensions of 4 mm ID, and a length of 4 m. The length is required in order to achieve (for this experimental apparatus set-up) high maximum pulse cycle pressures.

The liquid shot Teflon tube of 0.8 mm ID has a length of only 100 mm. This tube dimensions are set for liquid precursor injection.

The tube between the pulse control and reactor subsystems is also made from Teflon, and has an internal diameter of 0.8 mm, with a length of 20 mm.

4.2.c The CVD reactor

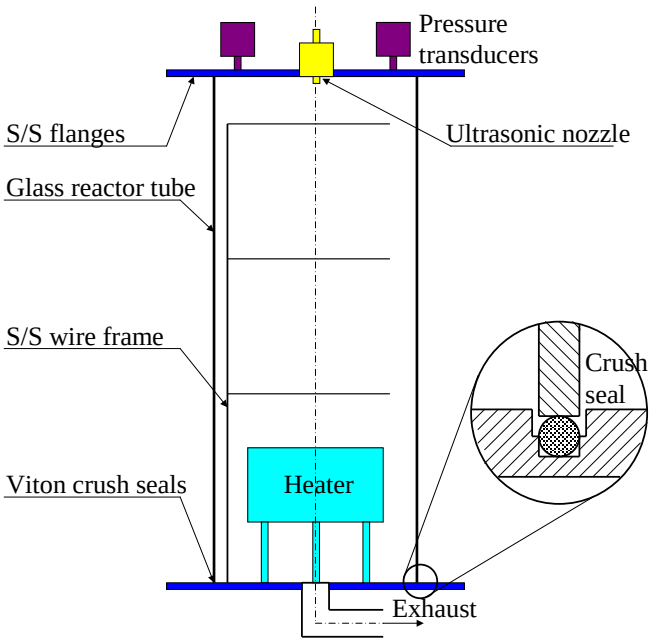

Figure 4.5 Pulsed-CVD reactor

Figure 4.5 is a schematic representation of the 118 mm ID, 400 mm height Pulsed-CVD reactor. It consists of six main components:

1. Ultrasonic nozzle

SONO-TEK 8700-120 nozzle with a micro sprays orifice shape. Because the nozzle is used for liquid precursor atomization, it didn't need to be powered, as we used gaseous N_2 as

precursor. Also, the needle that restricts the nozzle feed tube has not been used, as the tube needed to be clear in order to obtain high maximum reactor pressures during pulse flow regime experiments.

Figure 4.6 is a section through the nozzle. It shows the nozzle components and their geometrical aspect. The nozzle dimensions and specifications are given in figure 4.7.

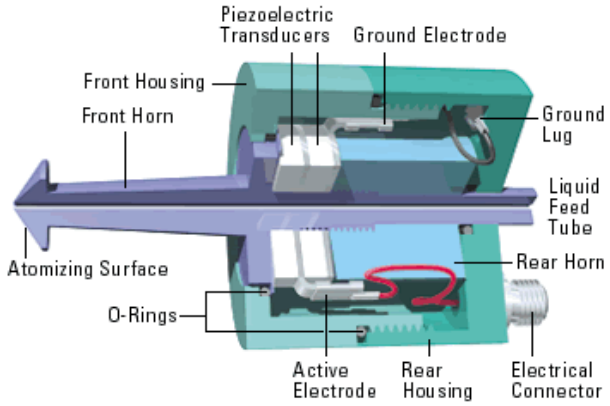

Figure 4.6 Ultrasonic nozzle components (source SONO-TEK Corporation)

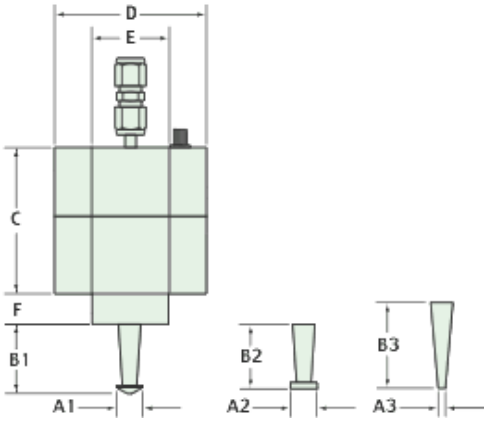

Dimensions (inch)									
A1	B1	A2	B2	A3	B3	C	D	E	F
0.23	0.44	0.23	0.40	0.09	0.56	1.0	1.44	0.50	0.34

Specifications			
Operating Frequency (kHz)	Maximum Flow Rate (gph)	Median Drop Diameter (microns)	Weight (g)
120	0.4	18	196

Figure 4.7 Ultrasonic nozzle dimensions and specifications (source SONO-TEK Corporation)

2. Pressure transducers

Two absolute pressure transducers (capacitance manometers) MKS BARATRON have been used during the open reactor volume flow field as a function of the cycle length experiments. The first transducer is a 626A model with a range of 5×10^{-4} to 1 Torr, and the second one is a 622A model with a range of 0.5 to 1000 Torr. Both have a very good dynamic response with a time constant of less than 20 ms, and an accuracy of 0.25 %.

The transducers have been connected to a MKS PDR-C-2C power supply/digital readout for power supply and direct pressure reading. Separately, they have been connected to the data acquisition and control system for file data recording.

As the two transducers readings didn't overlap and the measurement errors of the second pressure transducer were too big at pressure values of 133 Pa to 1300 Pa, filtering of the readings from the second transducer in this pressure range was required. An electronic filtering unit was used, that takes 1000 voltage values per second and filters them by averaging each consecutive 50 voltage signals. These last 20 per second averaged signals were sent to the computer to the data acquisition and control software.

The filtering and the two transducers direct readings resulted in three pressure channels on the computer software. The channels have been calibrated based on the difference in pressure readings between the digital reader and the software.

Figure 4.8 MKS BARATRON 626A capacitance manometer (source MKS BARATRON Corporation)

3. Reactor glass tube

The reactor wall is made of an 8 mm thick glass tube with internal diameter of 118 mm, and height of 400 mm. In order to obtain medium vacuum pressures inside, the tube seals on both ends, on the top and bottom edges, against two Viton circular O-rings installed inside grooves machined in the two top and bottom stainless steel flanges.

4. Reactor flanges

Two stainless steel flanges, one on each end of the reactor tube, are used to ensure a proper reactor enclosure for the vacuum processes that take place inside. On these two flanges have also been installed the pressure transducers, ultrasonic atomizer, and pulse control micro-valves (top flange); and the connection to the exhaust system (bottom flange).

5. Heater

The heater, with role of heating the substrate during real chemical vapour depositions, is a cylindrical assembly of two stainless steel shells that enclose in between a spiral heating element. Its outside dimensions are of 50 mm height and 74 mm diameter, and it is installed on four 10 mm OD stainless steel legs of 45 mm height. In these experiments it hasn't been powered.

Because of the influence the heater low temperature was having on the naphthalene samples in its vicinity, during the first two experimental sets it has been replaced with a dummy empty plastic heater with the same dimensions as the original one. During the last experimental set the heater has been removed from the reactor.

6. Wire frame

The wire frame on which the naphthalene samples were hanged was manufactured from stainless steel and consists of a vertical support wire of 3 mm diameter, and three horizontal, 1 mm diameter wires in which slots have been filed to stabilize the naphthalene samples positions during experiments.

4.2.d The exhaust circuit

The exhaust circuit consists of a 14 mm internal diameter valve, continuously kept open, a cold trap cooled down by using liquid N_2 stored in a vacuum flask, and the vacuum pump.

The cold trap retains the naphthalene vapours so they don't contaminate the vacuum pump oil. A large trap was manufactured because of the high quantity of naphthalene vapours it had to retain. It consists of an internal glass tube of 20 mm ID and an external tube of 60 mm ID. The exhaust circuit dimensions, including the cold vacuum trap, are given in chapter 7.

The vacuum pump is a VARIAN SD 200 model vane pump. It vacuums the reactor during the pump-down cycles through the exhaust circuit. The pump characteristics are given in table 4.1.

Table 4.1 Vane vacuum pump characteristics

Motor	Single phase, 220V, 50Hz
Vaned pump stages	2
Nominal rotation speed	1500 rev/min
Free air displacement	10 m^3/h
Base pressure (without gas ballast)	$<1x10^{-4}$mbar
Power rate	0.37 kW

All the exhaust subsystem components are connected to the reactor, vacuum pump and in between with 25 mm ID vacuum reinforced tubes.

4.2.e Data acquisition and control subsystem

The data acquisition and control subsystem has two roles in the experimental apparatus functioning. The first role is to control the functioning of the following electrical actuated components of the Pulsed-CVD system, by powering them at times required by the deposition process:

1. The four micro-solenoid valves from the pulse control subsystem
2. The ultrasonic nozzle
3. The two pressure transducers
4. The heater

During gaseous N_2 precursor experiments the ultrasonic nozzle and the heater have not been powered. The four micro-solenoid valves have been powered by an in-house manufactured power unit and the pressure transducers by using the MKS PDR-C-2C power supply unit. The timing control of the power supply to the micro-solenoid valves was achieved through the data acquisition and control software, while the pressure transducers have been continuously powered during experiments.

The second task of this subsystem was to gather experimental data for subsequent interpretation. This is the pressure data from the three different channels on the computer software. Previous to the experimental run, the three channels have been calibrated according to the readings on the MKS unit digital display. The calibration was done by reading the pressures from the MKS display at different levels and the corresponding values on the computer. If plotted, the readings would result in a line, as in figure 4.9.

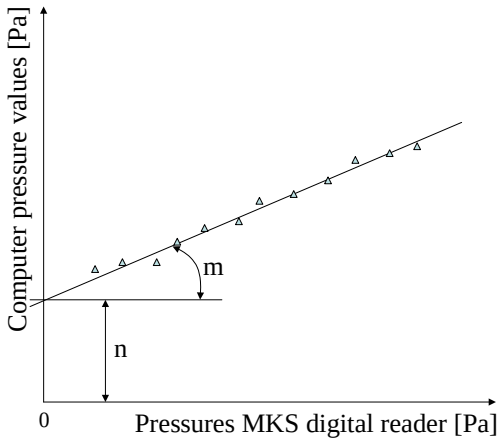

Figure 4.9 Pressure calibration

The slope m and intercept n of the data best fit line have been calculated and introduced in the software calibration section. At the end of the experiment the data was saved as a binary file, transformed into a text file, opened into Excel as a coma separated variable file, and saved.

4.3 Gas injection experimental apparatus set-up

As mentioned at the beginning of the chapter, the maximum reactor peak pressures obtained by injecting gaseous N_2 into the reactor by using the first experimental apparatus set-up were of less than 1 kPA. The reason is the injected gas flow velocity limitation through the 0.8 mm ID Teflon tube between the last micro-valve of the pulse control zone to the ultrasonic nozzle (and implicitly through the small internal diameter channels inside the micro-valves and the manifold they have been installed on).

In order to obtain higher reactor peak pressures, in the pulse control system area, the four BURKERT micro-valves have been replaced with two HUMPHREY 1/8 inch valves actuated by 24 VDC, 4.5 W solenoids. In this way the internal diameter of the tube between the last valve and the reactor has been increased from 0.8 mm to 6 mm. By doing this modification, maximum reactor absolute peak pressures in the range of 14 kPa have been obtained. This was required for experiments during which the reactor flow field uniformity as a function of increased peak pressures was studied.

Figure 4.10 is the schematic representation of the gas injection apparatus set-up.

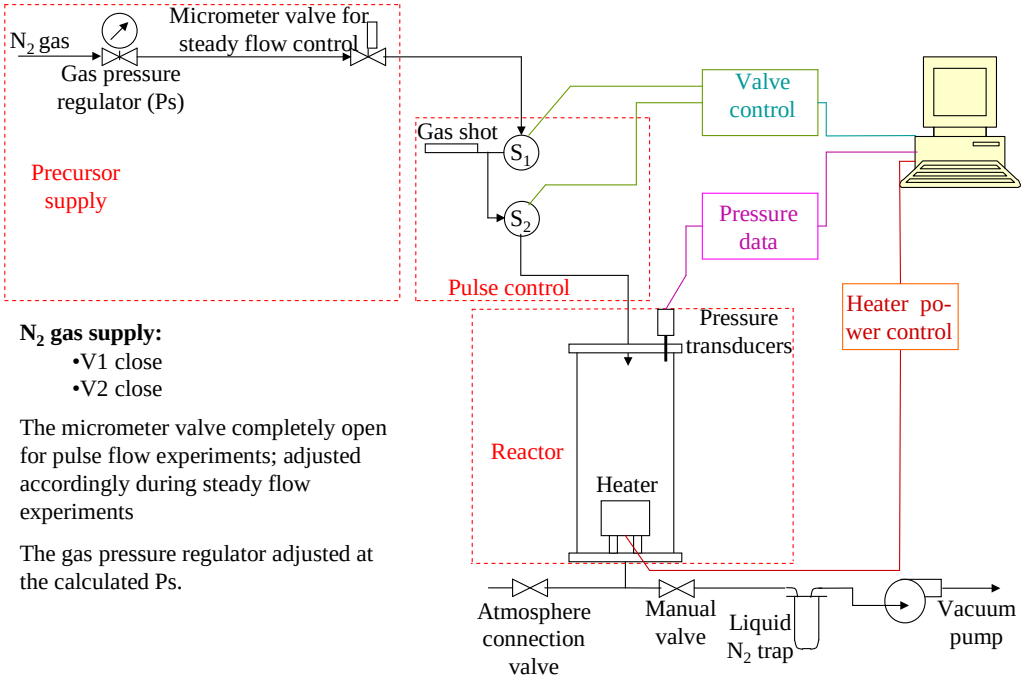

Figure 4.10 Gas injection Pulsed-CVD apparatus set-up

A number of just two valves is sufficient for the gas injection, as no need to separate the gas shot tube from the liquid shot tube exists; the metered quantity of gaseous precursor to be injected during each pulse is firstly stored into the gas shot tube between the two valves, and after that injected into the reactor at the beginning of each pulse by opening the second valve, S_2.

In order to achieve maximum pressures inside the gas shot tube, the micrometer valve was fully opened during pulse flow experiments. In steady flow experiments it was adjusted in order to obtain the required steady flow pressures.

The ultrasonic nozzle was not installed on this apparatus set-up, as it is required just during liquid precursor injections.

A temperature transducer and a BOURDON pressure gage have also been installed on the gas shot tube to measure the gaseous N_2 temperature and pressure at the reactor entrance.

The supply volume was increased by connecting a 2 l hermetically closed SCHOTT DURAN bottle at the end of the gas shot tube.

The last modification made to this apparatus set-up was the replacement of the 0.5 - 1000 Torr, 622A MKS BARATRON pressure transducer with a 0.05 - 100 Torr, 622A one. This was required as the intermediary filtered pressure readings accuracy was still poor. The replacement resulted in accurate readings in the range from 0 to 100 Torr by using this transducer and the small, 626A one. The two pressure channels have been calibrated as previously explained and the data saved in the same manner.

This second, gas injection apparatus set-up was used during the last two experimental sets. A dummy plastic heater was used during the second experimental set, and no heater was installed inside of the reactor in the last set of experiments.

Chapter 5

Experimental method

5.1 Method outcomes

This chapter describes the experimental steps, detailing them into procedural actions performed in order to obtain comparable experimental results in all the experimental sets, and an easy to find, follow and interpret experimental data.

The description refers to both experimental apparatus set-ups.

The section is divided into nine methods employed for the respective experimental stage requirements. The first three sections describe the methods involved in general experimental tasks. The next four detail what an experimental set (for certain reactor geometry) consisted of, or the experimental steps taken during the practical research. In the last two sections, the experiments' Excel workbooks naming and a summary data interpretation explanation are included.

The purpose to experimental work was the flow dynamics study in different internal configurations Pulsed-CVD reactors using the naphthalene sublimation technique. Naphthalene cylinders have been cast, machined, weighted and then assembled in the experimental apparatus in their respective run positions.

The experiments measure the exposure of the naphthalene surfaces to the experimental flow field. After an appropriate time of exposure, the run was stopped. Then the naphthalene samples were removed and weighed again. The weight measurements determined the mass losses of the naphthalene samples, which, together with the samples external areas and the time duration of the run, allow calculation of the total mass transfer rate from each of the six sample surfaces.

The time duration of an experiment was of 30 minutes, to allow the determined specific sublimation from active surfaces.

The mass losses extraneous to the experiments have been allowed as handling errors. They were evaluated by performing null time duration auxiliary runs after the first three real experiments. The results showed extraneous losses under 1% from the mass losses during experiments.

5.2 Naphthalene cylinders fabrication

The naphthalene cylinders have been fabricated by using a casting procedure, which employed the use of aluminium moulds made of two separate pieces that assembled together forms cavities with the shapes of the cylinders. Molten naphthalene was poured into the mould cavities and allowed to solidify. The melting point of naphthalene is 80.3 ^{0}C, but superheating of the molten naphthalene was needed to allow complete filling of the mould cavity prior to the occurrence of solidification. The naphthalene, supplied by BDH Laboratory - Poole, England, was of over 99% purity. As there are no narrow gaps or passages inside the mould cavities, the preheating of the mould wasn't necessary. The mould cavities were polished, as the naphthalene surfaces had to have a glasslike smoothness.

After casting, the cylinders were machined on a lathe to bring them to the desired height.

Because of the positions the cylinders occupied inside of the reactor, and the fact that they needed not to disturb the gas flow, small naphthalene samples have been cast. They have a diameter of 10 mm and a height of 14 mm.

Below, the stages of the experimental procedure regarding the cylinders fabrication, handling and data logging are presented:

a. Cast and machine naphthalene cylinders (6 off). Fill in the experimental sheet the mean dimensions of the cylinders.
b. Weigh each cylinder on the electronic scale and fill the weights in the experimental sheet, according to their position inside the reactor.

c. Keep the naphthalene cylinders in a gas tight container until the start of the experiment. This time had to be as short as possible, as the mass losses extraneous to the experiments had to be minimal. The naphthalene container used during these experiments had a volume of a 0.8 dm^3.

5.3 Precursor supply valves manual setting

As seen in the previous chapter in figure 4.3, where the liquid injection Pulsed-CVD system is schematically shown, in order to supply precursor to the pulse control valves (that control the exact quantity of fluid injected into the reactor), the first setting step of the experimental apparatus set-up was to manually adjust the valves V1, V2, and V3 for precursor supply.

This had to be done before the adjustment of the gas pressure regulator for the supply of gaseous N_2, with the micrometer valve fully open, as per the pulse flow experiments requirements (the steady flow experiments required subsequent adjustment of these two valves, as will be seen in the steady pressure experiment run).

During experiments employing the gas injection apparatus set-up, all valves to and from the bottles have been closed. The gaseous N_2 was supplied directly through the micrometer valve line.

5.4 Pulse control valves operating times setting

In the same figure 4.3, it can be seen that after passing the liquid precursor supply system zone, the fluids arrive at the pulse control micro-valves (figure 5.1) that are injecting controlled precursor quantities inside the reactor.

The adjustment of the amount injected precursor can be done by varying the length of the liquid loop. The precursor injection timing was achieved through controlled actuation of the four micro-valves. Their time sequence actuation was controlled by the computer software through the valve actuation power unit.

Solenoid valves
S1 – Gas supply
S2 – Liquid supply
S3 – Supply select
S4 – Discharge select

Sequence
1. –S4 (stop discharge)
2. S1+S2+S3 (charge)
3. -S2 (stop liquid)
4. -S1 (stop gas)
5. -S3+S4 (discharge)

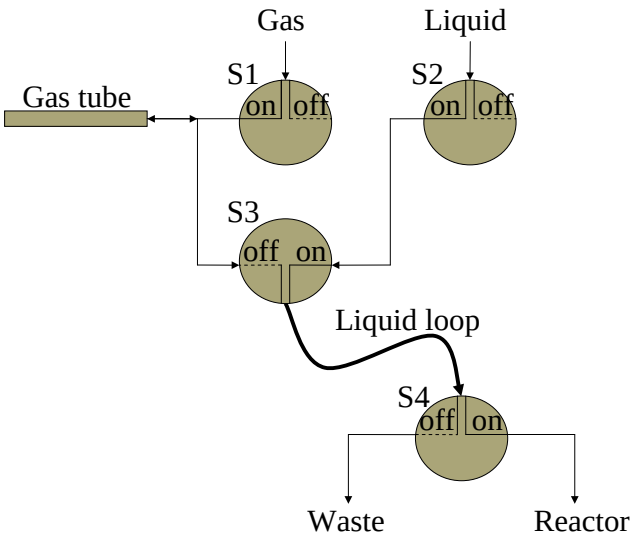

Figure 5.1 Liquid injection apparatus set-up pulse control subsystem

The liquid injection experimental apparatus set-up micro-valves time sequence actuation, consisting of five steps, is presented below. The sequence can easy be followed on figure 5.2, where each stage is presented in correspondence with the reactor's pulse pressure curve. Here $\Delta t = 1/100$ s is the computer control software time unit.

In the liquid injection apparatus set-up, the pulsed control valves time sequence is evolving in five steps:

1. **Stop discharge:** S4 off at the beginning (t = 0) of the valves cycle period (to insure that any liquid supplied in excess by S3 during the charge of the in-feed valves is sent to the waste).
2. **Charge:** S1, S2, S3 on at $t = 2\Delta t$, so that these valves only turn on after S4 turns off.
3. **Stop liquid:** S2 off at $t = m\Delta t$, between $t = 2\Delta t$ and $t = t_p - t_i$, big enough to fill the volume between S2 and S4 with liquid at supply pressure.
4. **Stop gas:** S1 off at $t = n\Delta t$, between $t = 2\Delta t$ and $t = t_p - t_i$, big enough to fill the volume between S1 and S3 with gas at supply pressure.
5. **Discharge:** S3 off and S4 on between $t = t_p - t_i$, and the end of the valves cycle period. The time between $t = t_p - t_i$, and the end of the valves cycle period is the injection time.

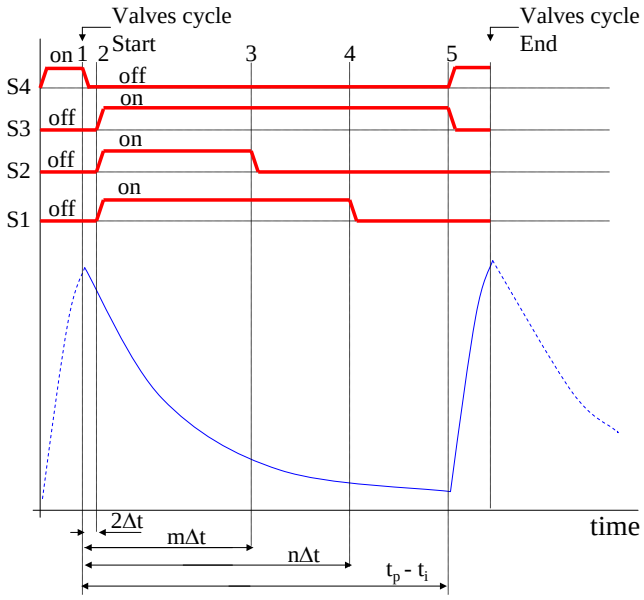

Figure 5.2 Liquid injection apparatus set-up micro-valves time sequence

In this study the liquid precursor was replaced with gaseous N_2.

Figure 5.3 is the pulse control subsystem representation of the gas injection experimental apparatus set-up.

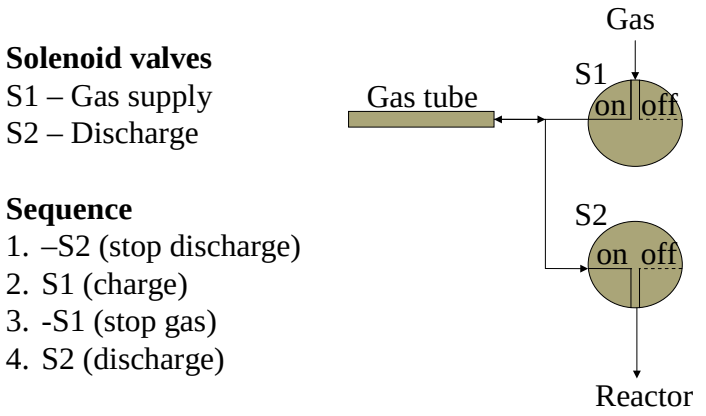

Figure 5.3 Gas injection apparatus set-up pulse control subsystem

Here, the pulse control valves time sequence is evolving by the following steps (figure 5.4):

1. **Stop discharge:** S2 off at the beginning (t = 0) of the valves cycle period (to insure that no gaseous precursor enters the reactor).
2. **Charge:** S1 on at t = 2Δt, so that this valves turns on only after S2 turns off.

3. **Stop gas:** S2 off at t = mΔt, big enough to fill the volume between S1 and S2 with gas at the supply pressure.
4. **Discharge:** S2 on at t = t_p - t_i. The time between t = t_p - t_i, and the end of the valves cycle period is the injection time.

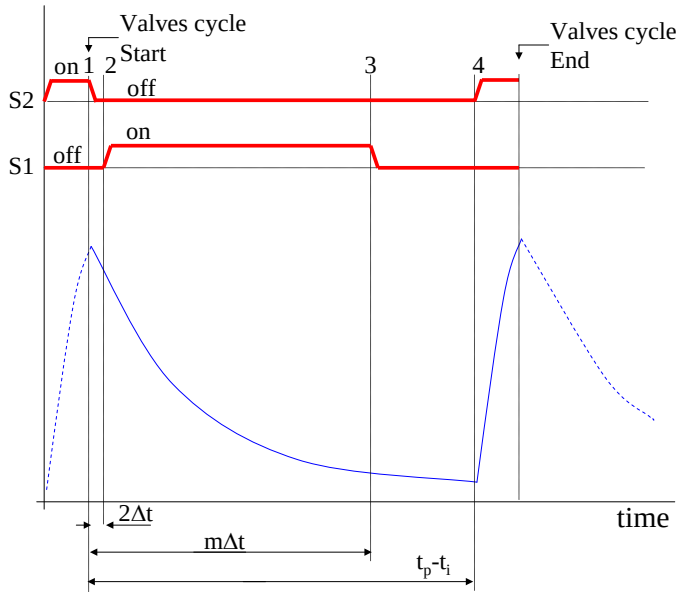

Figure 5.4 Gas injection apparatus set-up valves time sequence

5.5 Development of naphthalene measurement method

The reactor volume flow field uniformity as a function of the pulse cycle length experimental set consisted in a number of over 100 pulse and steady flow experiments. Not all the experiments needed to be interpreted, as some have been run in order to prepare the final ones. During these experiments, the cycle times t_p have been varied between 0.15 to 4 times 5 s (time value reduced compared to the reactor molecular time constant τ = 6.6 s as the reactor pulse cycle maximum pressures achieved were low – under 1 kPa).

The reactor volume flow field uniformity as a function of the pulse cycle maximum pressure, and the stacked wafer experimental sets have been performed at cycle time values of $t_p = 4\tau = 26.4$ s and sequentially increasing reactor pressure values (1 kPa to 14 kPa). The difference between these two sets was the method the naphthalene samples have been installed inside of the reactor (chapter 3). Each set consisted in a number of 16 experiments.

Next, the experimental procedural steps are detailed.

5.5. a Reactor set-up

At the beginning of each experimental set, the reactor was prepared by performing the next procedural steps:

1. Set the supply pressure.
2. Fill liquid N_2 into the vapour trap's flask.
3. Install the wire frame naphthalene support on the reactor's bottom flange.
4. Position the reactor cylinder on the bottom flange, check the proper positioning of the flanges relative to its glass wall, and close the reactor.
5. Turn on the pulse control valves MKS power supply unit. Allow a 15 minutes valves and manometers warm-up time.

5.5. b Steady vacuum (evacuated reactor) experiment

In order to evaluate the experiments' cycle times t_p and determine the reactor molecular time constant τ, as well as for compensation of the raw data for the sublimation rate by subtraction, a first experiment under a steady vacuum at the pump-down condition of the naphthalene vapour pressure, was run:

1. Weigh naphthalene cylinders on the electronic scale and write the values in the experiment data sheet.
2. Put the cylinders in the corresponding slots in the naphthalene container, close the container and bring it at the experimental apparatus location.
3. Open the reactor, remove the glass wall, open the naphthalene container and position the naphthalene cylinders on the wire frame support in positions corresponding to the ones inside the container.
4. Position the reactor cylinder on the bottom flange, check the proper positioning of the flanges relative to its glass wall, and close the reactor.
5. Close the atmosphere connection valve.
6. Turn on the vacuum pump.

7. Turn on the data acquisition and control program and make sure valve S4 (S2 for the gas injection experimental apparatus set-up) is turned off.
8. Start the data-log binary file.
9. Vacuum the reactor to the ultimate pressure.
10. Plot the resulted pump-down curve.

5.5.c System check

To check the proper functionality of all system components in pulse flow regime, prior to real pulse flow experiments, initial runs of about 7 minutes have been conducted, ensuring that desired pressures inside of the reactor were reached and that no problems were to appear when filling the naphthalene cylinders for the pulse flow experiments.

To achieve this, after closing the reactor, the following steps have been performed:

1. Close the atmosphere connection valve.
2. Turn on the vacuum pump.
3. Turn on the data acquisition and control program and make sure valve S4 (S2 for the gaseous precursor experimental set-up) is turned off.
4. Vacuum for 5 minutes to reach reactor ultimate pressure.
5. Load the saved pulse control valves configuration file and start the valves actuation.
6. Run the system for another 2 minutes (until the reading of the pressure on the meter show that the cycles are stable and the system reached the desired pressures).
7. Stop the data acquisition file, and the pulse control valves configuration file immediately after it.
8. Turn off the vacuum pump and on the atmosphere connection valve immediately after it.
9. Load the experimental data into Excel and draw a pressure variation graph to check the system functionality.

These Excel workbooks have not been kept.

5.5.d Pulse flow experimental method

After the system check, the pulse flow reactor experiments have been conducted.

Below are presented the experimental, recording and interpretation steps required for one experiment:

1. Weight the naphthalene cylinders on the electronic scale and write the values in the experiment data sheet.
2. Put the cylinders in the corresponding slots in the naphthalene container, close the container and bring it at the experimental apparatus location.
3. Open the reactor, remove the glass wall, open the naphthalene container and position the naphthalene cylinders on the wire frame support (between wafers during the third experimental set) in positions corresponding to the ones inside the container.
4. Position the reactor cylinder on the bottom flange, check the proper positioning of the flanges relative to its glass wall, and close the reactor.
5. Close the atmosphere connection valve.
6. Turn on the vacuum pump.
7. Turn on the data acquisition and control program and make sure valve S4 (S2 for the gaseous precursor experimental set-up) is turned off.
8. Start the data acquisition file.
9. Vacuum for 5 minutes to reach reactor ultimate pressure.
10. Set the pulse control valves configuration file and start the valves.
11. Run the system for another 25 minutes.
12. Turn off the data acquisition file and the pulse control valves configuration file immediately after it.
13. Turn off the pump and on the atmosphere connection valve immediately after it.
14. Save the data acquisition file.
15. Open the reactor, remove the naphthalene cylinders positioning them on the corresponding slots in the naphthalene container, and close the container.
16. Weight the cylinders on the electronic scale and write the values in the experiment data sheet.
17. Load the experimental data into Excel and save the workbook.

Complete and interpret data:

18. Complete all the additional data in the experiment's Excel workbook.
19. Draw the pulse pressure variation graphs.
20. Calculate the naphthalene specific sublimation uniformity and the non-dimensional molecular flux J_C^*.

5.5.e Steady flow experimental method

For each pulse flow experiment, the equivalent steady pressure was computed using the mean value definition formula:

$$\overline{P} = \frac{\int_0^t P(t) \cdot dt}{t} \tag{5.1}$$

where t is the experiment stable pulse cycles duration, of 1500 seconds (25 minutes).

Next, the following experimental steps have been performed:

1. Without naphthalene samples inside, position the reactor cylinder on the bottom flange, check the proper positioning of the flanges relative to its glass wall, and close the reactor.
2. Close the atmosphere connection valve.
3. Turn on the vacuum pump.
4. Set the pulse control valves S1 and S4 on, respectively S2 and S3 off (for the gas injection apparatus set-up, both valves S1 and S2 are turned on, in their opened position).
5. Adjust the gas pressure regulator and the micrometer valve to reach the computed steady pressure inside the reactor. Run the system for two minutes to make sure the (steady) pressure keeps constant.
6. Turn off the vacuum pump and on the atmosphere connection valve immediately after it.
7. Prior to the real experiment, weight the naphthalene cylinders on the electronic scale and write the values in the experiment data sheet.

8. Put the cylinders in the corresponding slots in the naphthalene container, close the container and bring it at the experimental apparatus location.
9. Open the reactor, remove the glass wall cylinder, and position the naphthalene samples on the wire frame support (between the wafers during the third experimental set) in the positions corresponding to the ones inside the container.
10. Position the reactor cylinder on the bottom flange, check the proper positioning of the flanges relative to its glass wall, and close the reactor.
11. Close the atmosphere connection valve.
12. Turn on the vacuum pump.
13. Turn on the data acquisition and control program and make sure the pulse control valve S4 (S2 for the gas injection apparatus set-up) is turned off.
14. Start the data acquisition file.
15. Pump-down for 5 minutes to reach reactor ultimate pressure.
16. Set the pulse control valves S1 and S4 on, respectively S2 and S3 off (for the gas injection apparatus set-up, both valves S1 and S2 are turned on in their open position).
17. Run the system for another 25 minutes.
18. Turn off the data acquisition file.
19. Turn off the vacuum pump and on the atmosphere connection valve immediately after it.
20. Save the data acquisition file.
21. Open the reactor, remove the naphthalene cylinders, positioning them on the corresponding slots in the naphthalene container, and close the container.
22. Weigh the cylinders on the electronic scale and write the values in the experiment data sheet.
23. Load the experiment data into Excel and save the workbook.

Complete and interpret data:

24. Complete all the additional data in the experiment's Excel workbook.
25. Draw the steady pressure data graphs.
26. Calculate the naphthalene specific sublimation uniformity.

5.6 Experiments name standard

The experimental data files have been named using the following general naming sequence:

Set number - Experiment number - Flow type: SV for Steady Vacuum; PF for Pulsed Flow (cycle time t_p [s] for experiments where this parameter is varied, maximum cycle pressure [Pa; kPa] for experiments where the maximum pressure is varied); SP for Steady Pressure (steady equivalent pressure $\overline{P}$ value [Pa]) - Reactor name – Heater name

The reactors and the heaters have been named as shown inn table 5.1, where r_1, h_1 / r_2, h_2 are the top/base heaters radiuses and heights, as shown in figure 5.5.

Table 5.1 Reactors/heaters naming standard

Annotations for files titles:								
Reactor	Small			Big	**Heater**	Small	Medium	Big
Radius [mm]	59			105	r_1 [mm]	73.0	96.0	185.0
Height [mm]	400	300	200	532	h_1 [mm]	22.5	22.5	22.5
Name	S1	S2	S3	B	r_2 [mm]	73.0	73.0	73.0
					h_2 [mm]	27.5	27.5	27.5
					Name	H1	H2	H3

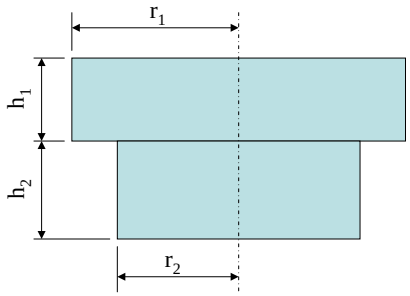

Figure 5.5 Heaters radiuses/heights

Table 5.1 comprises all the available reactors/heaters names. During this study the first reactor (S1) and the small heater (H1) have been used. In further experimental research the rest of the system components standard names can be used, and other components that are going to be purchased can also be named by using the same rule.

5.7 Experimental interpretations

After the completion of the reactor volume flow field uniformity as a function of the pulse cycle length experimental set, sublimation uniformity results and all other experimental

system parameters have been centralized in a table consisting of four divisions, each one for a different value of the injection time (appendix C). Injection times of 0.2 s, 0.4 s, 0.8 s, and 1 s have been considered. When using the liquid injection experimental apparatus set-up, increase of the maximum reactor pressures have been achieved by increasing the gaseous N_2 injection times t_i. The experiments have been run in the order of injection times increase.

Sublimation uniformity graphs, specific sublimation graphs, and pressure graphs have been drawn based on the data, compared and interpreted for different injection/cycle times, in pulse/steady flow regimes. Chapter 11 includes the experimental results interpretation, with explanations regarding system performance in the two different flow regimes.

For the reactor volume flow field uniformity as a function of the pulse cycle maximum pressure and stacked wafer flow uniformity experimental sets, the sample specific sublimation uniformity results have been centralized separately for pulse/steady flow experiments for increased reactor pressure values. The sample sublimation uniformities in equivalent experiments have been compared and graphically represented.

Chapter 6

Theoretical background of Pulsed-CVD

6.1 Pulse flow measurable parameters

In this chapter the measurable pulse flow parameters are presented, as they will be used during calculations and data interpretation. They are divided in time and pressure parameters.

The temperature variations of the gaseous N_2 in the gas shot tube have been measured. No significant differences relative to the room temperature have been observed. It is assumed that the gaseous precursor temperature inside the reactor is always constant, and equal to the room temperature.

6.1.a Times considered during one pulse flow cycle

Figure 6.1 is the graph of the reactor pressure during one pulse flow cycle.

Each cycle consists of two subsequent time stages:

a. Gas precursor injection: $0 \leq t \leq t_i$, where t_i is the total time for gas injection.
b. Gas evacuation: $t_i \leq t \leq t_p$, with t_p called the “cycle time”.

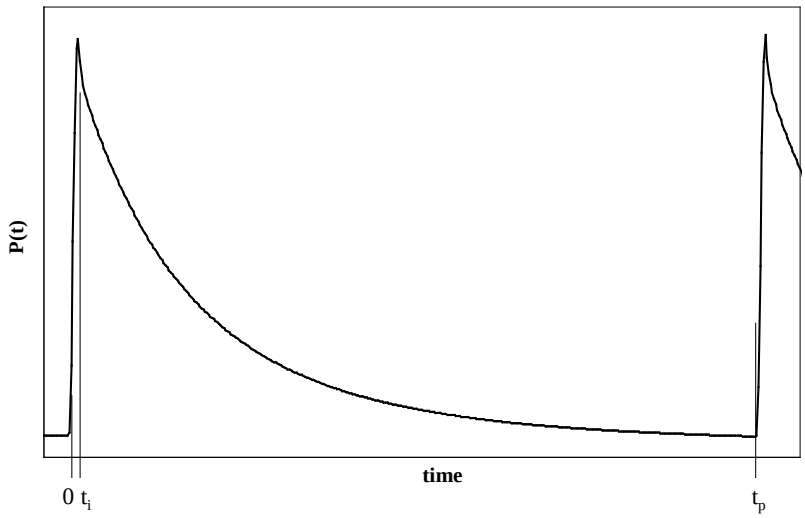

Figure 6.1 Experimental times during one pulse cycle

At the beginning of the cycle, high supply pressure gaseous N_2 is injected into the low pressure reactor.

Next, the reactor gas is evacuated by a vacuum pump, through the exhaust system.

The pressure evolution during the pump-down time ($t_p - t_i$) is determined by the pump speed S_P, exhaust system conductance C, and the gas maximum cycle pressure P_{max}.

6.1.b Pressures considered during one stable pulse flow cycle

During one cycle, the next pressures have been considered:

a. Maximum pressure P_{max}
b. Minimum pressure P_{min}
c. Ultimate pressure P_u (the lowest pressure the reactor can reach)
d. Average (equivalent steady flow) pressure, which by definition is:

$$\overline{P} = \frac{1}{t_p} \cdot \int_0^{t_p} P(t)dt \qquad (6.1)$$

From the above pressures, the next pressure differences, relative to the cycle ultimate pressure, can be determined:

$$\Delta P_{\max} = P_{\max} - P_u \tag{6.2}$$

$$\Delta P_{\min} = P_{\min} - P_u \tag{6.3}$$

$$\Delta \overline{P} = \overline{P} - P_u \tag{6.4}$$

This research uses all the above defined cycle pressures, as represented in figure 6.2.

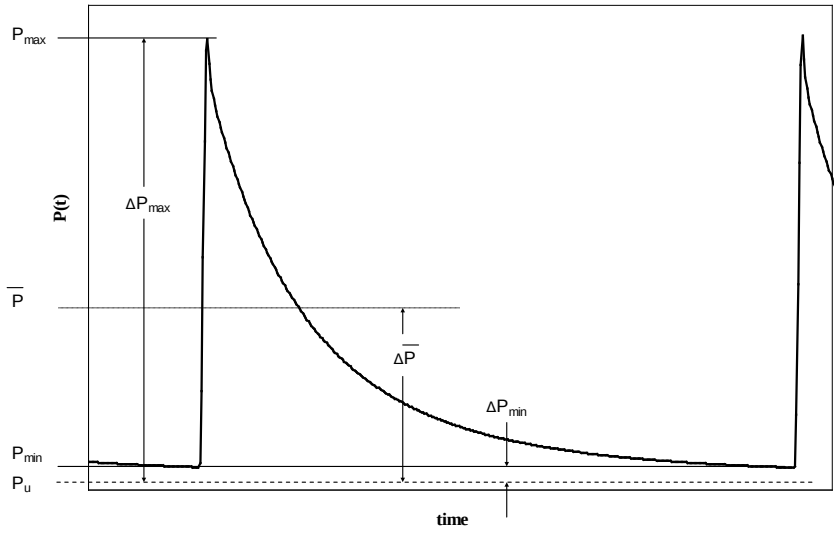

Figure 6.2 Pressures during one pulse cycle

6.2 **Theoretical considerations** [16]

Each cycle in the reactor begins with the injection of a set number of molecules n_i, from the injection tube which has a supply volume V_s, at a supply pressure P_s. Molecules are removed from the system at a rate Q_P by the vacuum pump with speed S_P through the exhaust system with conductance C. The supplied gas, reactor and surrounding temperatures are considered to be equal, $T_S = T_R = T$.

The molecular reactor balance during one cycle is:

$$\dot{n}_L dt - \frac{Q_P}{V_R}(n(t) - n_u)dt = d(n(t) - n_u) \tag{6.5}$$

The number of molecules remaining in the reactor volume any time during the pulse cycle is:

$$n(t) = (n_i + n_u) - \int_0^t \dot{n} \cdot dt \tag{6.6}$$

where n(t) is the number of molecules in the chamber at any time, n_u is the number of molecules at the reactor ultimate pressure P_u, $\int_0^t \dot{n} \cdot dt$ is the number of molecules evacuated in time t from the beginning of the cycle, and $\dot{n}_L$ is the molecular leak rate, small compared to the number of molecules injected and the evacuation pump rate.

From the ideal gas law, the number of molecules injected at the beginning of each cycle is:

$$n_i = (P_S - P_{\max}) \cdot \frac{V_S \cdot N_A}{R_0 \cdot T} = (P_{\max} - P_u) \cdot \frac{V_R \cdot N_A}{R_0 \cdot T} \tag{6.7}$$

where P_s is the absolute supply pressure in the supply tube, before the injection, and P_{max} is the initial reactor pressure at the beginning of the pulse cycle pump-down period (cycle peak pressure).

Rearranging and integrating from the start of a pulse t = 0, at any time during the pulse cycle t, and substituting equations 6.6 and 6.7 in 6.5, the pump down pressure variation is described by:

$$P(t) = (P_{\max} - P_u) e^{-\frac{(Q_p / V_R) \cdot t}{1 + Q_p / C}} + P_u \tag{6.8}$$

From the vacuum science theory [1], the volume displacement rate at the base of the reactor is:

$$S = \frac{Q_p \cdot C}{Q_p + C} \tag{6.9}$$

and the reactor molecular time constant τ is:

$$\tau = \frac{V_R}{S} \tag{6.10}$$

The dimensionless reactor pressure can be written as:

$$P^*(t) = \frac{P(t) - P_u}{P_{\max} - P_u} = e^{-\frac{t}{\tau}} \tag{6.11}$$

Equation 6.11 can be used to calculate the reactor pressure at any time t:

$$P(t) = P_u + (P_{\max} - P_u)e^{-\frac{t}{\tau}} \tag{6.12}$$

6.3 The dimensionless molecular flux [32]

6.3.a Dimensionless molecular flux calculation

The molecular incidence rate Φ(t) equation is:

$$\Phi(t) = \frac{N_A \cdot P(t)}{\sqrt{2\pi \cdot M \cdot R_0 \cdot T_R}} \tag{6.13}$$

where N_A is the Avogadro number, M is the precursor molecular weight, R_0 is the Universal Gas Constant, and T_R is the temperature inside the reactor.

The total flux per unit surface area, over a time interval equal to one pulse cycle t_p, is determined by substituting equation 6.12 into 6.13, and integrating over the pulse cycle:

$$J_C = \frac{N_A}{\sqrt{2\pi \cdot M \cdot R_0 \cdot T}} \left[\tau \left(P_{\max} - P_u \right) \cdot \left(1 - e^{-\frac{t_p}{\tau}} \right) + P_u t_p \right] \tag{6.14}$$

Using the definitions $J_{\min} = \Phi_{\min} \tau$ and $J_{\max} = \Phi_{\max} t_p$, the dimensionless molecular flux over a pulse cycle can be defined as:

$$J_C{}^* = \frac{J_P - J_{\min}}{J_{\max} - J_{\min}} = \frac{\tau}{t_p} \cdot \left(1 - e^{-\frac{t_p}{\tau}} \right) \tag{6.15}$$

This is the mathematical form of the dimensionless molecular flux as previously [16] calculated.

Next, the algorithm used in order to find the dimensionless molecular flux expression as a function of the reactor pressures is detailed.

By using relation 6.12, equation 6.1 can be written as:

$$\overline{P} = \frac{1}{t_p} \int_0^{t_p} \cdot \left[P_u + (P_{\max} - P_u) \cdot e^{-\frac{t}{\tau}} \right] \cdot dt \tag{6.16}$$

or:

$$\overline{P} = \frac{1}{t_p} \left[P_u t_p + (P_{\max} - P_u) \int_0^{t_p} e^{-\frac{t}{\tau}} dt \right] = \frac{1}{t_p} \left[P_u t_p + \left(P_{\max} - P_u \right) \cdot \left(-\tau \right) \cdot \left(e^{-\frac{t_p}{\tau}} - 1 \right) \right] \tag{6.17}$$

that gives:

$$\overline{P} = P_u + (P_{\max} - P_u) \frac{\tau}{t_p} \left(1 - e^{-\frac{t_p}{\tau}} \right) \tag{6.18}$$

Using equations 6.2 and 6.4, equation 6.18 can be expressed as:

$$\Delta\overline{P} = \Delta P_{\max}\frac{\tau}{t_p}\left(1-e^{-\frac{t_p}{\tau}}\right) \tag{6.19}$$

and the dimensionless equivalent pressure will be:

$$\Delta\overline{P}^{*} = \frac{\Delta\overline{P}}{\Delta P_{\max}} = \frac{\tau}{t_p}\left(1-e^{-\frac{t_p}{\tau}}\right) \tag{6.20}$$

which is exactly the value of the dimensionless molecular flux over a pulse cycle, expressed in 6.15. As the ultimate pressure has a very low value, in the range of 4 to 7 Pa in our experiments, we can write:

$$\Delta\overline{P}^{*} = \frac{\Delta\overline{P}}{\Delta P_{\max}} = \frac{\tau}{t_p}\left(1-e^{-\frac{t_p}{\tau}}\right) = J_C{}^{*} \cong \frac{\overline{P}}{P_{\max}} \tag{6.21}$$

Below, relation 6.21 is verified by expressing the dimensionless molecular flux over a pulse cycle as a function of the ratio between the cycle molecular flux and the maximum molecular flux over the cycle time t_p.

The cycle molecular flux can be calculated by integrating equation 6.13 over a cycle:

$$J_C = \frac{N_A}{\sqrt{2\pi\cdot M\cdot R_0\cdot T}}\int_0^{t_p} P(t)\cdot dt \tag{6.22}$$

and the maximum molecular flux can be written as:

$$J_{C\max} = \frac{N_A}{\sqrt{2\pi\cdot M\cdot R_0\cdot T}}P_{\max}t_p \tag{6.23}$$

The dimensionless molecular flux can, by using equations 6.1, 6.22 and 6.23, be expressed as:

$$J_C^{\ *} = \frac{J_C}{J_{C\max}} = \frac{\int_0^{t_p} P(t) \cdot dt}{P_{\max} t_p} = \frac{\overline{P}}{P_{\max}} \qquad (6.24)$$

This is the dimensionless parameter used during the reactor volume flow field uniformity as a function of the pulse cycle length experimental set for the comparison of sublimation uniformities between different injection times pulse flow experiments (U vs. $J_C^{\ *}$).

6.3.b Dimensionless molecular flux representation

In figure 6.3 the dimensionless molecular fluxes and the naphthalene samples sublimation uniformities are plotted against cycle time values of up to 20 s. This particular experiment was run in the second part of the reactor volume flow field uniformity as a function of the pulse cycle length experimental set, for an injection time of 0.4 s.

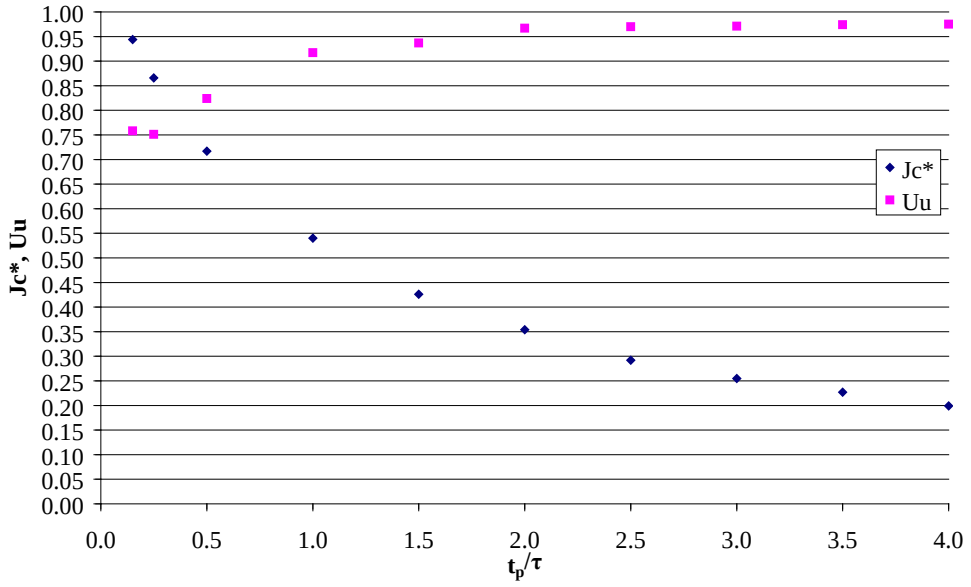

Figure 6.3 Uncompensated sublimation uniformities and dimensionless molecular fluxes as a function of the cycle times, for a constant injection time t_i = 0.4 s

As seen in figure 6.3, the value of the dimensionless molecular flux increases from low values at large cycle times, to values close to unity at very short cycle times. This is caused

by the decrease of the pressure integral over the cycle when decreasing the cycle time, combined with the increase of the cycle maximum pressure. The effect is represented in figure 6.4.

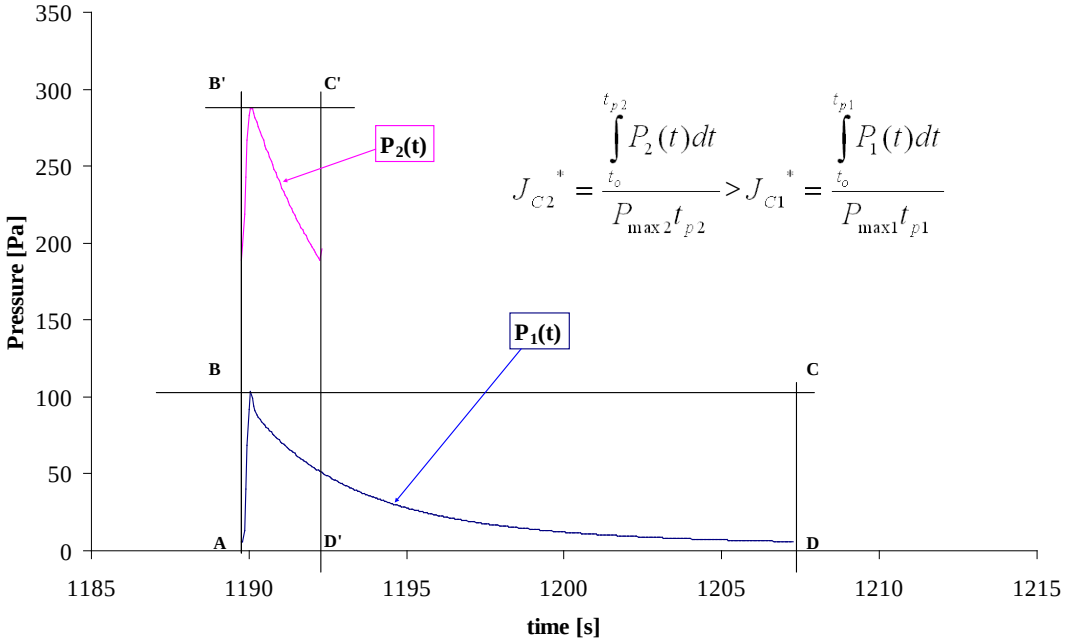

Figure 6.4 Graphical comparison between dimensionless molecular flux values for different conditions pulse flow cycles

The constant variation of the dimensionless molecular flux from values of zero to one during the pulse flow experiments, when decreasing the cycle time, is the reason it is considered the proper dimensionless parameter to be used in the comparison of the sublimation uniformities at different cycle conditions.

Chapter 7

Calculation of the reactor time constant [1]

One of this thesis aims is to find the values of the cycle time t_p as a function of the system molecular time constant τ, for optimum flow field uniformities.

The reactor time constant is calculated both in molecular flow ($P \cdot D < 3.15 \cdot 10^{-3} Torr \cdot cm$) and viscous flow ($P \cdot D > 5.55 \cdot 10^{-1} Torr \cdot cm$), where P is the reactor pressure and D is the exhaust system average diameter. The analytic results are compared to the values of τ determined experimentally on a pump-down pressure curve of the reactor. Figure 7.1 is a scaled drawing of the reactor and its exhaust circuit including their dimensions, based on which the calculations have been performed.

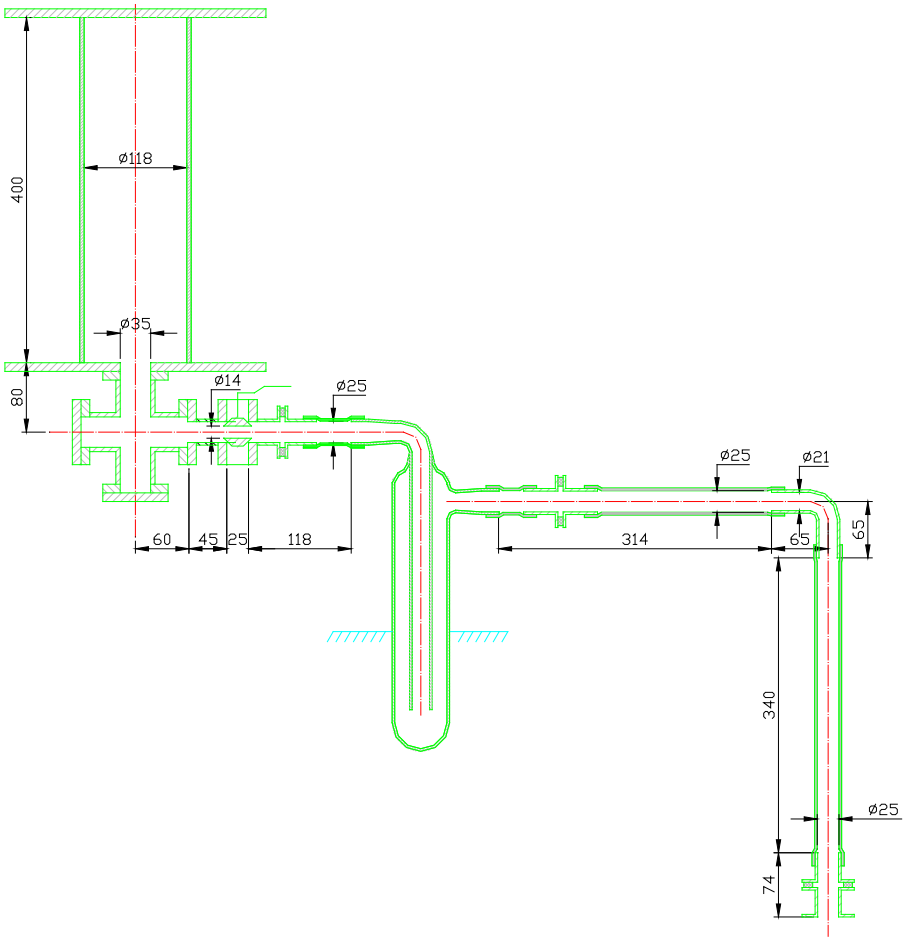

Figure 7.1 Pulsed-CVD reactor and exhaust circuit (dimensions in mm)

7.1 Conductance of the exhaust circuit line in molecular flow regime

The following values of the gaseous N_2 molecular mass and temperature have been considered in calculations:

M_{N2} = 28.016 g/mol
T = 293 K

7.1.a Conductance of the aperture between the reactor and the exhaust system

$$C = 2.86 \cdot \sqrt{\frac{T}{M}} \cdot D^2 = 113.33 \cdot l / s \tag{7.1}$$

7.1.b Elbow after aperture

Elbow diameter D = 3.5 cm; Elbow angle $\theta = 90^0$

Elbow equivalent length:

$$L_e = L_{ax} + 1.33 \cdot \frac{\theta}{180} \cdot D = 16.33 \cdot cm \tag{7.2}$$

Elbow conductance:

$$C = 3.81 \cdot \sqrt{\frac{T}{M}} \frac{D^3}{L_e} = 32.36 \cdot l / s \tag{7.3}$$

7.1.c Conductance of the long tubes of D = 2.5 cm

Total length of tubes: L = 4.5 + 11.8 + 31.4 + 34 + 7.4 = 89.1 cm

Tubes conductance:

$$C = 3.81 \cdot \sqrt{\frac{T}{M}} \frac{D^3}{L} = 2.16 \cdot l/s \tag{7.4}$$

7.1.d Conductance of the manual valve (considered a short pipe of constant cross-section)

Valve length and diameter: L = 2.5 cm; D = 1.4 cm

Valve conductance:

$$C = 3.81 \cdot \sqrt{\frac{T}{M}} \cdot \frac{D^3}{L + 1.33 \cdot D} = 7.75 \cdot l/s \tag{7.5}$$

7.1.e Conductance of the 2nd elbow

Elbow diameter D = 2.1 cm; Elbow angle $\theta = 90^0$

Elbow equivalent length:

$$L_e = L_{ax} + 1.33 \cdot \frac{\theta}{180} \cdot D = 14.4 \cdot cm \tag{7.6}$$

Elbow conductance:

$$C = 3.81 \cdot \sqrt{\frac{T}{M}} \frac{D^3}{L_e} = 7.93 \cdot l/s \tag{7.7}$$

7.2 Conductance of the cold trap in molecular flow regime

The cold trap conductance was calculated based on the dimensions in figure 7.2.

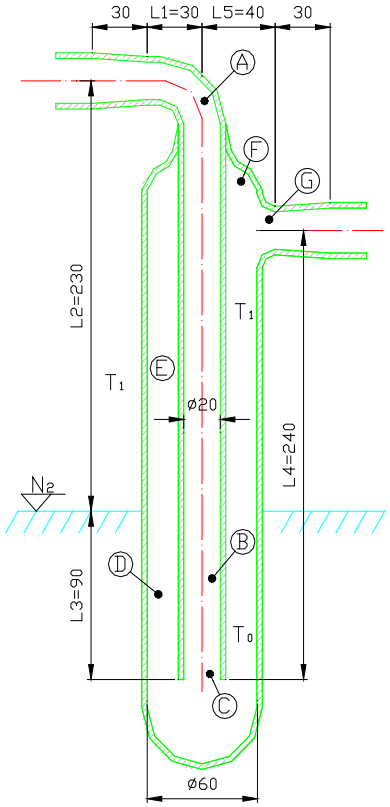

Figure 7.2 Cold vacuum trap (dimensions in mm)

The environment/liquid N_2 temperatures considered in calculations, and the vacuum trap internal/external tubes radiuses, are: T_1 = 293 K, T_0 = 77 K, r_1 = 1 cm, r_2 = 3 cm. The formulas assumes that the temperature of the inner tube decreases linearly from T_1 at the level of the liquid nitrogen to T_0 at the bottom of the inner tube, and that the outer wall of the trap may be considered at T_1 above the liquid nitrogen, and at T_0 below this level [1, p.93].

7.2.a Inlet elbow (A)

Elbow equivalent length (for elbow angle $\theta = 90^0$):

$$L_e = L_{ax} + \frac{\theta}{180} \cdot r_1 = 27.33 \cdot cm \tag{7.8}$$

Elbow conductance:

$$C = 3.81 \cdot \sqrt{\frac{T}{M}} \frac{8 \cdot r_1^{\,3}}{L_e} = 3.6 \cdot l/s \tag{7.9}$$

7.2.b Straight pipe (B) conductance

$$C = 3.81 \cdot \sqrt{\frac{T}{M}} \frac{8 \cdot r_1^{\,3}}{L_e} \cdot \frac{\sqrt{T_1} + \sqrt{T_0}}{\sqrt{T_1}} = 8.27 \cdot l/s \tag{7.10}$$

7.2.c Diaphragm (C) conductance

$$C = 3.64 \cdot \sqrt{\frac{T_0}{M}} \cdot \pi \cdot \left(r_2^{\,2} - r_1^{\,2}\right) \cdot \frac{r_2^{\,2}}{r_1^{\,2}} = 1365 \cdot l/s \tag{7.11}$$

7.2.d Annular pipe under the liquid nitrogen level (D)

Annular pipe constant:

$$\frac{D_i}{D_0} = \frac{r_1}{r_2} = 0.33 \Rightarrow k_0 = 1.096 \tag{7.12}$$

Annular pipe conductance:

$$C = 3.81 \cdot \sqrt{\frac{T_1}{M}} \cdot \frac{8k_0 \cdot \left(r_2 - r_1\right)^2 \cdot \left(r_1 + r_2\right)}{2 \cdot L_3 \cdot \sqrt{T_1}} \cdot \frac{T_1 - T_0}{\sqrt{r_1 T_1 + r_2 T_0} - \sqrt{T_0\left(r_1 + r_2\right)}} = 227.1 \cdot l/s \tag{7.13}$$

7.2.e Conductance of the annular space above the liquid nitrogen level (E)

$$C = 3.81 \cdot \sqrt{\frac{T_1}{M}} \cdot \frac{8k_0 \cdot \left(r_2 - r_1\right)^2 \cdot \left(r_1 + r_2\right)}{L_4 - L_3} = 115.96 \cdot l/s \tag{7.14}$$

7.2.f Exit aperture (F) conductance

$$C = 2.86 \cdot \sqrt{\frac{T_1}{M}} \cdot 4r_1^{\,2} = 37 \cdot l/s \tag{7.15}$$

7.2.g Exit tube (G) conductance

$$C = 3.81 \cdot \sqrt{\frac{T_1}{M}} \cdot \frac{8r_1^{\,3}}{L_5 - r_2} = 98.6 \cdot l/s \tag{7.16}$$

7.2.h Conductance of the tapered tubes (identical) before and after the trap

Tapered tube internal diameters and length:

D_1 = 2.5 cm; D_2 = 2 cm; L = 3 cm

Tapered tube conductance:

$$C = 7.62 \cdot \sqrt{\frac{T_1}{M}} \cdot \frac{D_1^{\,2} \cdot D_2^{\,2}}{(D_1 + D_2) \cdot L} = 45.64 \cdot l/s \tag{7.17}$$

7.2.i Total conductance of the cold trap

Considering the conductance values calculated with formulas 7.8 to 7.17, the total conductance of the trap have been calculated using the expression:

$$\frac{1}{C_{ct}} = \frac{1}{3.6} + \frac{1}{8.27} + \frac{1}{1365} + \frac{1}{227.1} + \frac{1}{115.96} + \frac{1}{37} + \frac{1}{98.6} + \frac{2}{45.64} = \frac{1}{2.02} \tag{7.18}$$

That gave a cold trap total conductance of:

$$C_{ct} \cong 2 \cdot l/s \tag{7.19}$$

7.2.j Total conductance of the exhaust circuit, including the big cold trap, in molecular flow, with gaseous N_2 at 20 ^{0}C as precursor

The exhaust circuit conductance in molecular flow, by considering the partial conductance from 7.1, 7.3, 7.4, 7.5, 7.7 and the cold trap conductance from 7.19:

$$\frac{1}{C_{tm}} = \frac{1}{113.33} + \frac{1}{32.36} + \frac{1}{2.16} + \frac{1}{7.75} + \frac{1}{7.93} + \frac{1}{2} = \frac{1}{0.795} \tag{7.20}$$

Total conductance of the exhaust circuit in molecular flow:

$$C_{tm} \cong 0.8 \cdot l/s \tag{7.21}$$

7.3 Calculation of the reactor time constant τ in molecular flow regime

7.3.a Vacuum pump (Varian 200) volume displacement rate

As per the characteristics given by the manufacturer:

S_P = 10 m^3/h = 2.77 l/s

7.3.b Calculation of the volume displacement rate at the base of the reactor

$$\frac{1}{S_m} = \frac{1}{C_{tm}} + \frac{1}{S_P} = \frac{1}{0.8} + \frac{1}{2.77} = \frac{1}{0.62} \tag{7.22}$$

This gives a volume displacement rate value of:

$$S_m = 0.62 \cdot l/s \tag{7.23}$$

7.3.c Reactor volume

The empty reactor volume:

$$V_R = \pi \cdot \left(\frac{1.18}{2}\right)^2 \cdot 3.98 = 4.35 \cdot l \tag{7.24}$$

7.3.d Heater volume

$$V_H \cong 0.25 \cdot l \tag{7.25}$$

7.3.e The reactor time constant τ in molecular flow

$$\tau_m = \frac{V_R - V_H}{S_m} \cong \frac{4.1}{0.62} = 6.6 \cdot s \tag{7.26}$$

7.4 Calculation of τ in viscous flow regime

The conductance of the exhaust circuit in other than molecular flow conditions inside of the reactor have been calculated using the general equation of flow:

$$C = C_m J \tag{7.27}$$

where the correction coefficient J is calculated using the equation:

$$J = \frac{1 + 271 \cdot \overline{DP} + 4790 \cdot (\overline{DP})^2}{1 + 316 \cdot \overline{DP}} \tag{7.28}$$

For example, for an experiment between P_{max} = 134 Pa (the top pressure value the small 626A capacitance manometer can read), and the reactor ultimate pressure, the average (equivalent steady flow) pressure as resulted from the experimental run calculations, will be:

$$\overline{P} \cong 22 \cdot Pa \cong 0.165 \cdot Torr \tag{7.29}$$

At this pressure, by using equation 7.28 and an average internal diameter D = 2.5 cm for the whole exhaust system, the correction coefficient will be:

$$J \cong 7 \tag{7.30}$$

The fact that the vacuum trap interior diameter is of 2 cm introduced an error in the analytical calculation, but this is just a check of the time constant values. They have been better approximated by using the real reactor pump-down curve (section 7.5).

As $\overline{P}D = 0.165 \cdot Torr \cdot 2.5 \cdot cm = 0.412 \cdot Torr \cdot cm$, in equivalent steady flow the system is close to the viscous flow regime with the report between the intermolecular and molecule-to-wall collisions:

$$\frac{X}{N} = \sqrt{2} \cdot \pi \cdot \frac{n}{V} \cdot \xi^2 \cdot D = 31.74 \cdot 10^3 \cdot D \cdot \frac{\overline{P}}{T} \cong 2.11 \tag{7.31}$$

Here $\frac{n}{V}$ is the number of molecules per unit volume, which at a temperature of 293 K, at the average pressure of 0.165 Torr, can be expressed as:

$$\frac{n}{V} = \frac{\overline{P}}{k \cdot T} \cong 4.08 \cdot 10^{19} \cdot molec / m^3 \tag{7.32}$$

where $k = \frac{R_0}{N_A} = 1.38 \cdot 10^{-23}\, J / K$ is the Boltzman constant.

In equation 7.31, ξ = 3.14 10^{-10} m is the gaseous N_2 molecular diameter, and D = 0.118 m is the reactor inside diameter.

The conductance of the exhaust system at this pressure is:

$$C_V = C_{tm} \cdot J \cong 0.8 \cdot 7 = 5.6 \cdot l / s \tag{7.33}$$

With this value, the transition regime at 0.165 Torr volume displacement rate at the base of the reactor can be calculated:

$$\frac{1}{S_{0.165Torr}} = \frac{1}{C_V} + \frac{1}{S_P} = \frac{1}{5.6} + \frac{1}{2.77} = \frac{1}{1.85} \Rightarrow S_{0.165Torr} = 1.85 \cdot l/s \qquad (7.34)$$

(as an observation, what limits S at this pressure is the vacuum pump volume displacement rate, S_P = 2.77 l/s).

τ is constant only in the molecular regime, in viscous or transition regimes it decreases with the increasing of the pressure. For the average pressure of 0.165 Torr, its value is:

$$\tau_{0.165Torr} = \frac{V_R - V_H}{S_{0.165Torr}} = \frac{4.1}{1.85} \cong 2.22 \cdot s \qquad (7.35)$$

Note: As mentioned, the use of the same diameter for the whole exhaust circuit in the calculation of the correction coefficient J for viscous flow introduced errors in the calculations in viscous regime. In practice, the exhaust circuit conductance in this flow regime is smaller.

7.5 Experimental determination of the reactor time constant τ

For the experimental determination of the reactor time constant, a pump-down curve from a maximum pressure of 134 Pa and an ultimate pressure of around 6 Pa (figure 7.3) was used. On this plot the continuous line is the curve resulted from data and the dotted lines are the plots for τ = 5 s, at different maximum pressures, as shown in the graph's legend.

The analytical pressure curves have been calculated based on the equation 6.12:

$$P(t) = P_u + (P_{\max} - P_u) \cdot e^{-\frac{t}{\tau}}$$

It can be seen that at P_{max} = 20 Pa the plot for τ = 5 s fits the data, when for higher maximum pressures, τ = 5 s is too big.

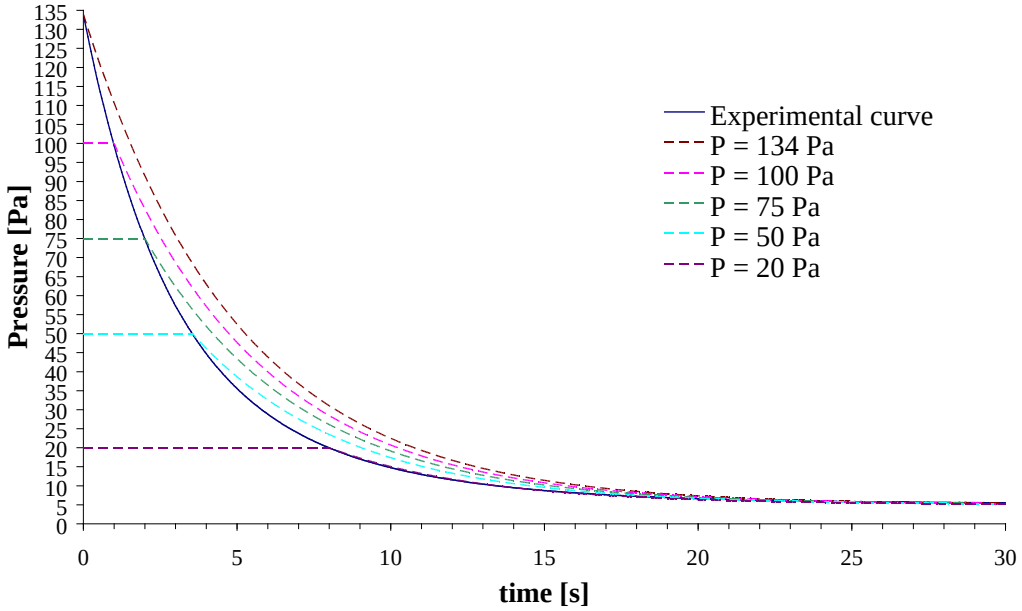

Figure 7.3 Comparison between analytical calculated pressure curves for τ = 5 s at different maximum pressures, and the experimental pressure curve

At P_{max} = 75 Pa the value of τ whose curve best approximate the data is τ = 4 s, as shown in figure 7.4.

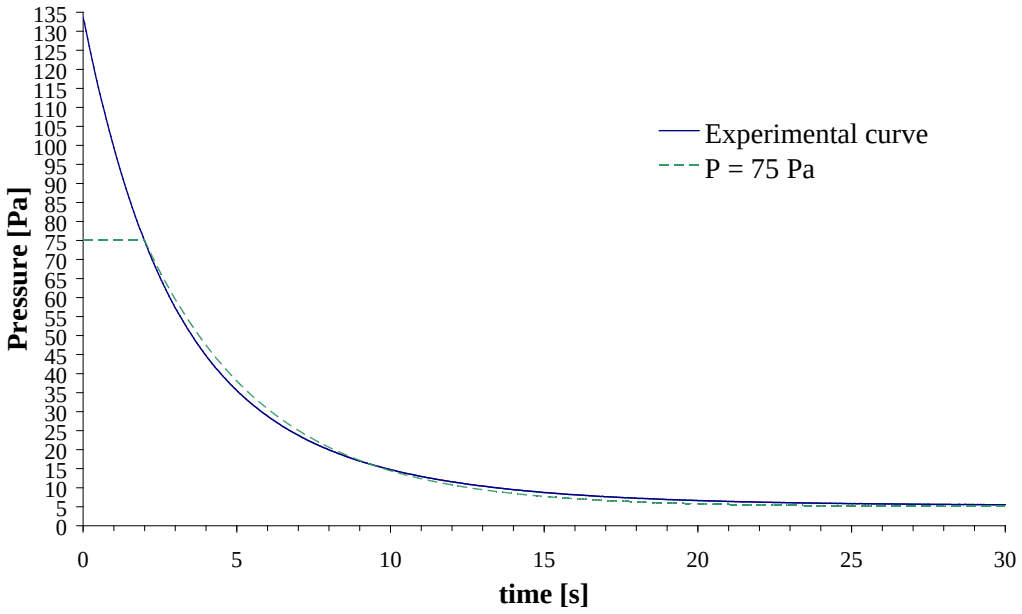

Figure 7.4 Comparison between analytical calculated pressure curve for τ = 4 s at a system maximum pressure of 75 Pa, and the experimental pressure curve

Where for P_{max} = 134 Pa, τ should be around a value of 3.6 s (figure 7.5).

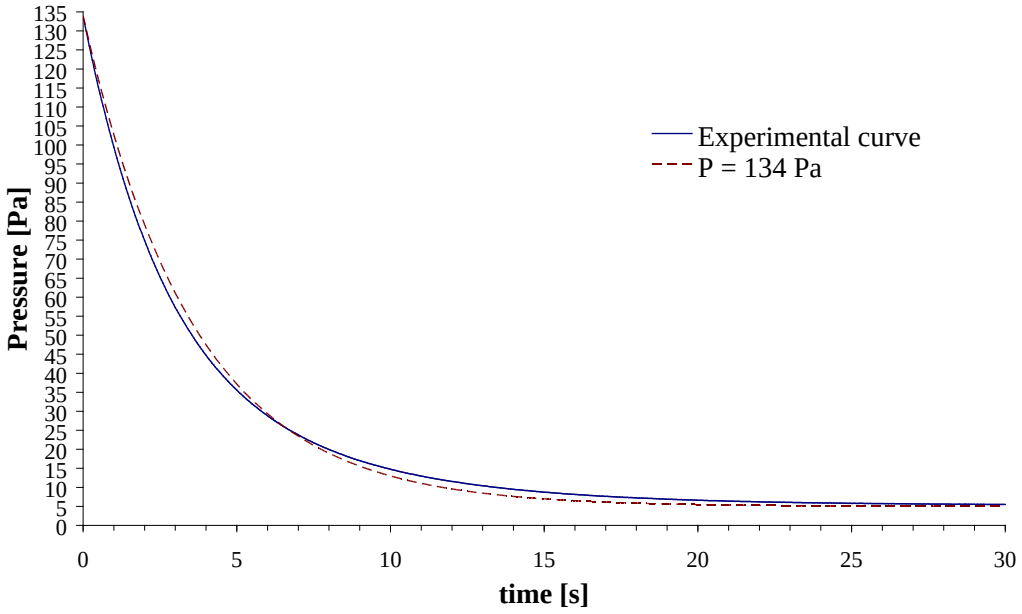

Figure 7.5 Comparison between analytical calculated pressure curve for τ = 3.6 s at a system maximum pressure of 134 Pa, and the experimental pressure curve

In this chapter the reactor time constant was analytically and experimentally determined. The results show that τ is constant only in molecular flow, and for our system its value is τ_m = 6.6 s.

When running the system at maximum pressures above the ones in molecular flow regime, there is no concept of a reactor time constant. As it was seen, its values decrease as the reactor pulse flow maximum pressure increases.

Chapter 8

Sublimation uniformity and error analysis [32]

8.1 Uniformity of naphthalene samples sublimation calculation

The uniformity of the flow in both pulse and equivalent steady flow inside of the Pulsed-CVD reactor is expressed based on the naphthalene samples sublimation uncompensated uniformity calculated as a function of the naphthalene cylinders weight loss during experiments:

$$\Delta m_i = \left(m_i - m_f\right)_i \tag{8.1}$$

with m_i / m_f being each sample masses before/after one experiment.

The specific sublimation of the naphthalene samples is:

$$S_{Si} = \frac{\Delta m_i}{A_{Si}} \tag{8.2}$$

where A_{si} is each separate cylinder exposed area to the flow (total external area of the cylinder).

The specific sublimation rate for each sample is given by the expression:

$$SR_{Si} = \frac{S_{Si}}{t} \tag{8.3}$$

where t is the sublimation time (experiment duration), same for all six samples during one experiment.

The uniformity is a non-dimensional measure, independent of the specific sublimation or the specific sublimation rate. It takes values between zero and one:

$$0 \le U \le 1 \tag{8.4}$$

For each experiment the uniformity was calculated by compensating and respectively normalizing the specific sublimation rates of the n = 6 naphthalene samples inside the reactor:

$$U = \frac{\sum_{i=1}^{n} SR_{S\,i} - \sum_{i=1}^{n} \left| SR_{S\,i} - \overline{SR_S} \right|}{\sum_{i=1}^{n} SR_{S\,i}} \tag{8.5}$$

or

$$U = 1 - \frac{\sum_{i=1}^{n} \left| SR_{S\,i} - \overline{SR_S} \right|}{\sum_{i=1}^{n} SR_{S\,i}} \tag{8.6}$$

where $\overline{SR_S}$ is the samples average specific sublimation rate:

$$\overline{SR_S} = \frac{\sum_{i=1}^{n} SR_{S\,i}}{n} \tag{8.7}$$

so that the uniformity can be expressed as:

$$U = 1 - \frac{1}{n} \cdot \sum_{i=1}^{n} \left| \frac{SR_{S\,i} - \overline{SR_S}}{\overline{SR_S}} \right| \tag{8.8}$$

A graphical representation of the sublimation uniformity is given in figure 8.1.

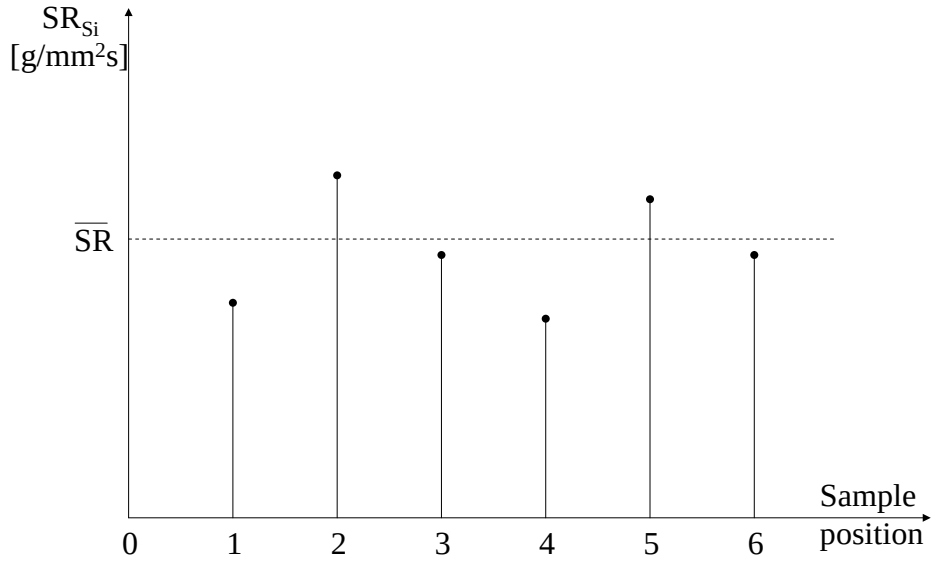

Figure 8.1 Naphthalene samples sublimation uniformity graphical representation

If expressing the difference between the individual and the average sublimation rates as:

$$\Delta SR_{S\,i} = SR_{S\,i} - \overline{SR_S} \tag{8.9}$$

from equation 8.8, the uniformity can be written as:

$$U = 1 - \frac{1}{n} \cdot \sum_{i=1}^{n} \left| \frac{\Delta SR_{S\,i}}{\overline{SR_S}} \right| \tag{8.10}$$

and knowing that the time t during each one of the experiments is the same for all the samples inside the reactor, by using equation 8.3 the uniformity can be expressed in terms of specific sublimations as:

$$U = 1 - \frac{1}{n} \cdot \sum_{i=1}^{n} \left| \frac{\Delta S_{S\,i}}{\overline{S_S}} \right| \tag{8.11}$$

with the difference between the individual cylinder specific sublimation and the average specific sublimation of all n cylinders:

$$\Delta S_{Si} = S_{Si} - \overline{S_S} \tag{8.12}$$

If expressing for each cylinder these differences as functions of the average specific sublimations:

$$\Delta S_{Si} = k_i \overline{S_S} \tag{8.13}$$

the uniformity can be written as:

$$U = 1 - \frac{1}{n}\sum_{i=1}^{n} k_i \tag{8.14}$$

Note: In order to calculate the sublimation compensated uniformity, expression 8.2 is replaced by $S_{Si} = \frac{\Delta m_i - \Delta m_{i,vacuum}}{A_{Si}}$, where $\Delta m_{i,vacuum}$ is the certain cylinder weight loss during the first part of the experiment (reactor pump-down time from atmospheric pressure to the system ultimate pressure).

8.2 Uniformity error analysis

In order to find the appropriate duration of each experiment, the amount of required sublimated naphthalene for each sample was estimated from the calculation of the absolute error in uniformity, by equalizing the contribution of sublimated mass absolute error with the external samples area absolute error.

From equation 8.11, by using the general formula for absolute error propagation [12, p. 72]:

$$\delta q \cong \left|\frac{\partial q}{\partial x}\right| \cdot \delta x + ... + \left|\frac{\partial q}{\partial z}\right| \cdot \delta z \tag{8.15}$$

where q is a function of several independent variables x, …, z:

$$q = f(x,...,z) \tag{8.16}$$

the absolute errors influencing the sublimation uniformity, as function of the sublimated mass absolute error δm, and of the external samples area absolute error δA can be expressed as:

$$\Delta U(\delta m) = \left| \frac{\partial U}{\partial \Delta S_{S_i}} \cdot \frac{\partial \Delta S_{S_i}}{\partial m} \right| \cdot \delta m + \left| \frac{\partial U}{\partial \overline{S_S}} \cdot \frac{\partial \overline{S_S}}{\partial m} \right| \cdot \delta m \tag{8.17}$$

$$\Delta U(\delta A) = \left| \frac{\partial U}{\partial \Delta S_{S_i}} \cdot \frac{\partial \Delta S_{S_i}}{\partial A_{S_i}} \right| \cdot \delta A + \left| \frac{\partial U}{\partial \overline{S_S}} \cdot \frac{\partial \overline{S_S}}{\partial \overline{A_S}} \right| \cdot \delta A \tag{8.18}$$

Next, the partial derivatives of equations 8.17 and 8.18 are estimated.

First, the partial derivatives relative to the specific sublimations are expressed.

Directly from equation 8.11, by considering the average specific sublimation $\overline{S_S}$ as being constant, can be calculated:

$$\frac{\partial U}{\partial \Delta S_{S_i}} = -\frac{1}{n} \cdot \frac{n}{\overline{S_S}} = -\frac{1}{\overline{S_S}} \tag{8.19}$$

Making use of relations 8.12 and 8.11:

$$\frac{\partial U}{\partial \overline{S_S}} = \frac{\partial}{\partial \overline{S_S}} \left[1 - \frac{1}{n} \cdot \sum_{i=1}^{n} \left| \frac{S_{S_i}}{\overline{S_S}} - 1 \right| \right] = -\frac{1}{n} \cdot \sum_{i=1}^{n} \frac{S_{S_i}}{\left(\overline{S_S}\right)^2} = -\frac{1}{\overline{S_S}} \tag{8.20}$$

Also:

$$\frac{\partial \Delta S_{S_i}}{\partial m} = \frac{\partial}{\partial m} \left(S_{S_i} - \overline{S_S} \right) = \left| \frac{\partial S_{S_i}}{\partial m} \right| + \left| \frac{\partial \overline{S_S}}{\partial m} \right| \tag{8.21}$$

where the specific sublimations partial derivatives relative to the sublimated mass are:

$$\frac{\partial S_{S_i}}{\partial m} = \frac{\partial}{\partial m} \left[\frac{\left(m_i - m_f\right)_i}{A_{S_i}} \right] = \left| \frac{\partial m_i}{\partial m} \right|_i \cdot \frac{1}{A_{S_i}} + \left| \frac{\partial m_f}{\partial m} \right|_i \cdot \frac{1}{A_{S_i}} = \frac{2}{A_{S_i}} \tag{8.22}$$

$$\frac{\partial \overline{S_S}}{\partial m} = \frac{\partial}{\partial m}\left[\frac{1}{n}\cdot\sum_{i=1}^{n}\frac{\left(m_i - m_f\right)_i}{A_{S_i}}\right] = \frac{1}{n}\cdot\sum_{i=1}^{n}\frac{\partial}{\partial m}\left[\frac{\left(m_i - m_f\right)_i}{A_{S_i}}\right] = \frac{2}{A_{S_i}} \qquad (8.23)$$

By replacing 8.22 and 8.23 into 8.21 and approximating that the external area of individual cylinders is equal to their average area $A_{S_i} \cong \overline{A_S}$ as $A_{S_i} = \overline{A_S} + \Delta A_{S_i}$ with $\Delta A_{S_i} \cong 0$, it results:

$$\frac{\partial \Delta S_{S_i}}{\partial m} \cong \frac{4}{\overline{A_S}} \qquad (8.24)$$

The partial derivatives relative to the samples external areas are:

$$\frac{\partial \Delta S_{S_i}}{\partial A_{S_i}} = \frac{\partial}{\partial A_{S_i}}\left(S_{S_i} - \overline{S_S}\right) = \left|\frac{\partial S_{S_i}}{\partial A_{S_i}}\right| + \left|\frac{\partial \overline{S_S}}{\partial A_{S_i}}\right| \cong 2\frac{S_{S_i}}{A_{S_i}} \qquad (8.25)$$

$$\frac{\partial \overline{S_S}}{\partial \overline{A_S}} \cong \frac{\partial}{\partial A_{S_i}}\left|\frac{1}{n}\sum_{i=1}^{n}\frac{\Delta m_i}{A_{S_i}}\right| = \frac{1}{n}\sum_{i=1}^{n}\frac{S_{S_i}}{A_{S_i}} = \frac{\overline{S}_S}{A_{S_i}} \cong \frac{\overline{S_S}}{\overline{A_S}} \qquad (8.26)$$

By substituting 8.19, 8.20, 8.23, and 8.24 into 8.17 the uniformity absolute error relative to the samples mass loss results:

$$\Delta U(\delta m) = \frac{1}{\overline{S_S}}\cdot\frac{4}{\overline{A_S}}\cdot\delta m + \frac{1}{\overline{S_S}}\cdot\frac{2}{\overline{A_S}}\cdot\delta m = \frac{6}{\overline{S_S}\cdot\overline{A_S}}\cdot\delta m = \frac{6}{\Delta m}\delta m \qquad (8.27)$$

And by replacing 8.19, 8.20, 8.25, and 8.26 into 8.18 the expression for the uniformity absolute error relative to the samples external areas is determined as:

$$\Delta U(\delta A) = \frac{1}{\overline{S_S}}\cdot\frac{2\cdot S_{S_i}}{A_{S_i}}\cdot\delta A + \frac{1}{\overline{S_S}}\cdot\frac{\overline{S_S}}{\overline{A_S}}\cdot\delta A \cong \left(\frac{2}{\overline{A_S}} + \frac{1}{\overline{A_S}}\right)\cdot\delta A = \frac{3}{\overline{A_S}}\delta A \qquad (8.28)$$

The total uniformity absolute error is expressed as the sum of the absolute errors calculated with 8.27 and 8.28:

$$\Delta U = \Delta U(\delta m) + \Delta U(\delta A) \cong \frac{6}{\overline{\Delta m}}\delta m + \frac{3}{\overline{A_S}}\delta A \tag{8.29}$$

The main contribution in the external area absolute error is the estimated absolute error in height measures, of about 0.2 mm. The unrolled cylinder lateral area is sketched in figure 8.2.

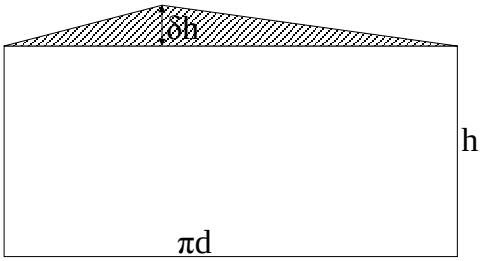

Figure 8.2 Naphthalene cylinder unrolled lateral area

In experiments, naphthalene cylinders of average heights of h = 14 mm, and diameters of d = 10 mm have been used. The average total cylinder external area is:

$$\overline{A_S} = \pi \cdot d \cdot h + \frac{\pi \cdot d^2}{2} \cong 597 \cdot mm^2 \tag{8.30}$$

The absolute error in external area measurement (the hatched triangle in figure 8.2) is, by considering the lateral area as being the one giving measurement absolute errors:

$$\delta A = \frac{\pi \cdot d \cdot \delta h}{2} = \frac{\pi \cdot 10 \cdot 0.2}{2} \cong 3.14 \cdot mm^2 \tag{8.31}$$

that results in:

$$\frac{\delta A}{\overline{A_S}} \cong \frac{3.14}{597} \cong 5.26 \cdot 10^{-3} \tag{8.32}$$

As the absolute error in mass measurements is $\delta m \cong 0.2$ mg, read on the electronic scale, by using equation 8.29 in which the absolute errors in area and mass measurements are equalized, and the result of equation 8.32, it results that the samples required experimental average mass loss is:

$$\overline{\Delta m} = \frac{2 \cdot 0.2}{5.26 \cdot 10^{-3}} \cdot mg \cong 80 \cdot mg \tag{8.33}$$

By running trial experiments, it was observed that in order to get these sublimation values, the duration of each experiment should be of about 30 minutes.

The total absolute error of the sublimation uniformity is calculated by using the quadratic sum independent random absolute errors equation [12, p. 73]:

$$\delta q = \sqrt{\left(\frac{\partial q}{\partial x} \cdot \delta x\right)^2 + \ldots + \left(\frac{\partial q}{\partial z} \cdot \delta z\right)^2} \tag{8.34}$$

as it is known that δq in equation 8.34 is always smaller or equal to δq in 8.15. Here q is expressed as in equation 8.16.

For uniformities U close to one, the samples sublimation uniformity absolute error is:

$$\Delta U = \sqrt{\left(\frac{6 \cdot 0.2}{80}\right)^2 + \left(\frac{3 \cdot 3.14}{600}\right)^2} \cong 0.022 \tag{8.35}$$

or a percentage error of 2.2%, quite a good value with the condition that attention to be given to the mass and area measurements during the experimental run, with very short times between the start/end of the experiments and the physical measurements, so that null extraneous errors introduced by time delays to be considered. For low uniformities, close to 0.5, the percentage error will be of 4.4%.

This error is considered low enough for the sublimation uniformity calculations. However, note that longer experiment durations would lead to lower errors, as the value of $\overline{\Delta m}$ will increase.

The time spent weighting and handling the naphthalene was of less than 3 min. per experiment, below 10% from the total experiment duration. The extraneous naphthalene mass losses were in a range of 1% from the total mass losses during experiments, which practically will not change the sublimation error.

Chapter 9

Pressure equations in pulse flow regime [32]

9.1 Experimental pressure data

The reactor volume flow field uniformity as a function of the pulse cycle length experimental set showed that by decreasing the cycle times under values of four times the reactor time constant τ, both the minimum and the maximum pressures are increasing from the system ultimate pressure, when starting to pulse, to a stable pulse regime. An intermediary phase develops between when the pulsing starts (from the reactor ultimate pressure) to when it stabilises to constant maximum and minimum pressure values.

Given the low pressures the experimental set was run, a reactor time constant value of $\tau = 5$ s was used for cycle time computations. A comparison between steady pulse regimes for cycle times $t_p = 4\tau = 20$ s, and $t_p = 0.25\tau = 1.25$ s is represented in figures 9.1 and 9.2. In order to obtain high maximum pressures with the liquid injection experimental apparatus set-up, these experiments have been run for a gas injection time $t_i = 0.8$ s.

In figure 9.1 the stable pulse regime starts immediately after the pressure into the reactor starts to pulse. Because at the end of the cycle the pulse regime minimum pressure is reaching very low values, of 1.1 times the system ultimate pressure, no intermediary phase is observed.

As we decrease the cycle time, the minimum/maximum pressure values in the stable pulse regime are taking continuously higher values, and an intermediary phase is starting to develop. The shorter the cycle times are, the higher the minimum/maximum pressures become, and the more pulses the intermediary phase includes. Figure 9.2 shows the pressure variation during the above mentioned phases (reactor pump-down at ultimate pressure; the intermediary, pressures increase, phase; and the stable pulse regime phase).

A second effect in the stable pulse regime, attributed to the decrease of the cycle time, was observed, namely the fact that the difference between the maximum and minimum pressures is constantly decreasing, leading to cycles with very close cycle pressure values.

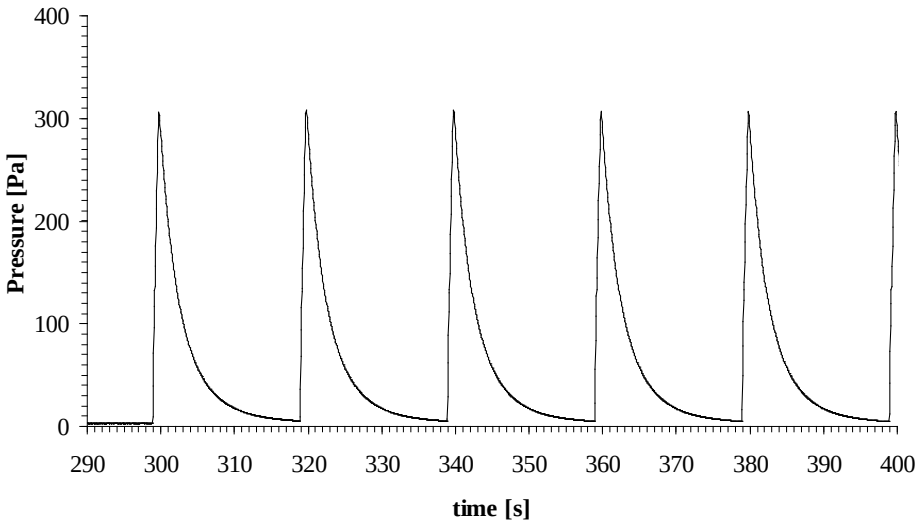

Figure 9.1 Pulse flow regime at t_p = 20 s and t_i = 0.8 s

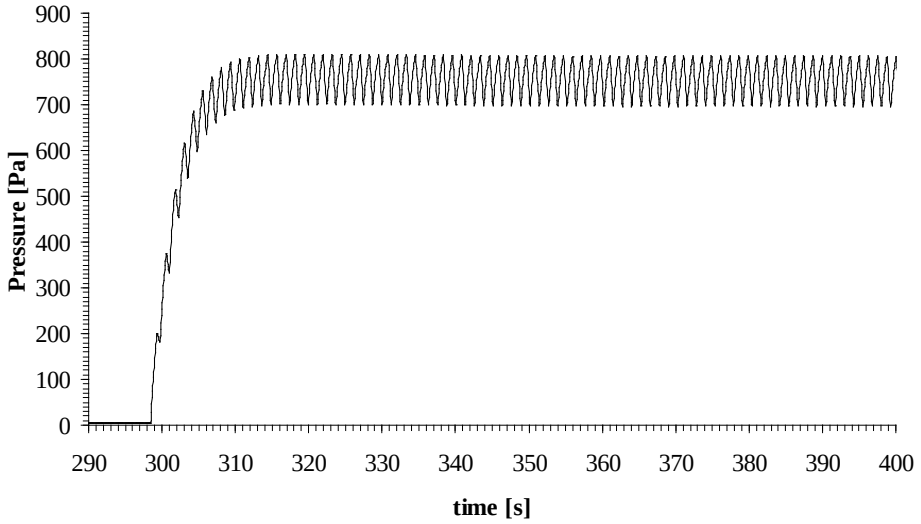

Figure 9.2 Pulse flow regime at t_p = 1.25 s and t_i = 0.8 s

9.2 Pulse cycle pressures analytical model

This section shows how the two previously described experimental effects can be analytically modelled. The mathematical expressions for the calculation of the maximum and minimum pressures, together with the method used in their determination are presented.

By considering the supply and reactor volumes connected to each other, and that the two volumes are completely isolated from surroundings (assuming the evacuated volume of gas during the very short injection times as negligible), the following equation expresses the gaseous N_2 mass conservation between the supply volume and the reactor volume:

$$V_S \cdot P_S + V_R \cdot P_{\min i} = (V_R + V_S) \cdot P_{\max i+1} \tag{9.1}$$

or:

$$P_{\max i+1} = \frac{V_S \cdot P_S}{V_R + V_S} + \frac{V_R \cdot P_{\min i}}{V_R + V_S} \tag{9.2}$$

where V_S is the supply volume before the ultrasonic nozzle (the volume of the gas contained inside the supply valves, the manifold channels and the liquid, respectively gas shot tubes), V_R is the reactor volume, P_S is the nitrogen gas supply pressure, and i is the cycle number.

Given that for the liquid injection experimental apparatus set-up V_R is much bigger than V_S ($\frac{V_S}{V_R} \cong 4 \cdot 10^{-6}$), equation 9.2 can be expressed as:

$$P_{\max i+1} \cong \frac{V_S \cdot P_S}{V_R} + \frac{V_R \cdot P_{\min i}}{V_R} = \frac{V_S \cdot P_S}{V_R} + P_{\min i} \tag{9.3}$$

The minimum pressure reached in one cycle, as a function of the ultimate pressure in the system, can also be approximated by using equation 6.12 at the end of one cycle time:

$$P_{\min i} = P_u + (P_{\max i} - P_u) \cdot e^{-\frac{t_p}{\tau}} \tag{9.4}$$

The cycle time t_p is identical for all cycles during the intermediary and stable pulse regimes in one experiment.

If expressing the maximum and respectively minimum pressures differences relative to the ultimate pressure (as in equations 6.2 and 6.3):

$$\Delta P_{\max} = P_{\max} - P_u \tag{9.5}$$

$$\Delta P_{\min} = P_{\min} - P_u \tag{9.6}$$

from relations 9.3 and 9.4, by using 9.5 and 9.6, it results:

$$\Delta P_{\max i+1} \cong \Delta P_{\min i} + \frac{V_S}{V_R} \cdot P_S \tag{9.7}$$

$$\Delta P_{\min i} = \Delta P_{\max i} \cdot e^{-\frac{t_p}{\tau}} \tag{9.8}$$

For cycles from 1 to n, with an initial condition $\Delta P_{min0} \cong 0$, ΔP_{max} and ΔP_{min} can be expressed as follows:

Cycle 1:

$$\Delta P_{\max 1} \cong \frac{V_S}{V_R} \cdot \left(P_S - P_{\min 0}\right) \cong \frac{V_S}{V_R} \cdot P_S \tag{9.9}$$

$$\Delta P_{\min 1} = \Delta P_{\max 1} \cdot e^{-\frac{t_p}{\tau}} \cong \frac{V_S}{V_R} \cdot P_S \cdot e^{-\frac{t_p}{\tau}} \tag{9.10}$$

Cycle 2:

$$\Delta P_{\max 2} \cong \Delta P_{\min 1} + \frac{V_S}{V_R} \cdot P_S \cong \frac{V_S}{V_R} \cdot P_S \cdot e^{-\frac{t_p}{\tau}} + \frac{V_S}{V_R} \cdot P_S \cong \frac{V_S}{V_R} \cdot P_S \cdot \left(1 + e^{-\frac{t_p}{\tau}}\right) \tag{9.11}$$

$$\Delta P_{\min 2} = \Delta P_{\max 2} \cdot e^{-\frac{t_p}{\tau}} \cong \frac{V_S}{V_R} \cdot P_S \cdot \left(1 + e^{-\frac{t_p}{\tau}}\right) \cdot e^{-\frac{t_p}{\tau}} \tag{9.12}$$

Cycle 3:

$$\Delta P_{\max 3} \cong \Delta P_{\min 2} + \frac{V_S}{V_R} \cdot P_S \cong \frac{V_S}{V_R} \cdot P_S \cdot \left(1 + e^{-\frac{t_p}{\tau}} + e^{-2\frac{t_p}{\tau}}\right) \tag{9.13}$$

$$\Delta P_{\min 3} = \Delta P_{\max 3} \cdot e^{-\frac{t_p}{\tau}} \cong \frac{V_S}{V_R} \cdot P_S \cdot \left(1 + e^{-\frac{t_p}{\tau}} + e^{-2\frac{t_p}{\tau}}\right) \cdot e^{-\frac{t_p}{\tau}} \tag{9.14}$$

.

.

.

Cycle n:

$$\Delta P_{\max n} \cong \Delta P_{\min n-1} + \frac{V_S}{V_R} \cdot P_S \cong \frac{V_S}{V_R} \cdot P_S \cdot \left(1 + e^{-\frac{t_p}{\tau}} + e^{-2\frac{t_p}{\tau}} + ... + e^{-(n-1)\frac{t_p}{\tau}}\right) \tag{9.15}$$

$$\Delta P_{\min n} = \Delta P_{\max n} \cdot e^{-\frac{t_p}{\tau}} \cong \frac{V_S}{V_R} \cdot P_S \cdot \left(1 + e^{-\frac{t_p}{\tau}} + e^{-2\frac{t_p}{\tau}} + ... + e^{-(n-1)\frac{t_p}{\tau}}\right) \cdot e^{-\frac{t_p}{\tau}} \tag{9.16}$$

9.3 Final pressures analytical expressions

From equations 9.15 and 9.16 it can be seen that ΔP_{max} and ΔP_{min} will reach constant values, as:

$$\lim_{n\to\infty}\left(\Delta P_{\max}\right) \cong \frac{V_S}{V_R} \cdot P_S \cdot \lim_{n\to\infty}\left(1 + e^{-\frac{t_p}{\tau}} + e^{-2\frac{t_p}{\tau}} + ... + e^{-(n-1)\frac{t_p}{\tau}}\right) = \frac{V_S}{V_R} \cdot P_S \cdot \frac{1}{1 - e^{-\frac{t_p}{\tau}}} \tag{9.17}$$

and:

$$\lim_{n\to\infty}\left(\Delta P_{\min}\right) \cong \frac{V_S}{V_R} \cdot P_S \cdot e^{-\frac{t_p}{\tau}} \cdot \lim_{n\to\infty}\left(1 + e^{-\frac{t_p}{\tau}} + e^{-2\frac{t_p}{\tau}} + ... + e^{-(n-1)\frac{t_p}{\tau}}\right) = \frac{V_S}{V_R} \cdot P_S \cdot \frac{e^{-\frac{t_p}{\tau}}}{1 - e^{-\frac{t_p}{\tau}}}$$

(9.18)

Equations 9.17 and 9.18 show that the stable pulse regime cycles evolve between constant minimum/maximum pressures.

9.4 Analytical determination of the number of intermediary cycles

By using the above minimum/maximum pressure equations, the number of intermediary cycles necessary to be run (from the moment we start to pulse from the reactor ultimate pressure) in order to reach stable pressure cycles, can be determined. This can be done by expressing the pulse cycle maximum pressures measurement error.

Considering maximum pressure differences lower 1 % in the stable pulse regime, the number of intermediary cycles can be calculated.

If k is the number of intermediary cycles, for any $k \geq 1$, by using equations 9.15 to write similar equations for cycles k and k + 1, and the limit from equation 9.17, it can be written:

$$\frac{\Delta P_{\max k+1} - \Delta P_{\max k}}{\Delta P_{\max k}} = e^{-k\frac{t_p}{\tau}} \cdot \left(1 - e^{-\frac{t_p}{\tau}}\right) \leq 0.01 \tag{9.20}$$

equation that after some algebraic modifications becomes:

$$k \geq \ln\left(\frac{1 - e^{-\frac{t_p}{\tau}}}{0.01}\right) \cdot \frac{\tau}{t_p} \tag{9.21}$$

The number of intermediary cycles (rounded by addition to integers) and their total durations, as a function of a reactor time constant $\tau = 5$ s and the cycles lengths t_p/τ, are given in table 9.1.

It can be observed that even if the intermediary phase includes a larger number of cycles when lowering the cycle time t_p (third data column), the shorter this phase is going to be (last column).

Table 9.1 Number and total duration of intermediary cycles for different cycle lengths

t_p/τ	t_p (s)	k calculated	k rounded	$t_{intermed.}$ (s)
4	20	1.15	2	40
3	15	1.25	2	30
2	10	2.23	3	30
1	5	4.15	5	25
0.5	2.5	7.34	8	20
0.25	1.25	12.38	13	16.25

During the sublimation uniformity error analysis (chapter 8), an experiment duration of 30 minutes was established. The intermediary phase durations are considerably smaller than this value.

The reactor is continuously evacuated, so that, during the injection, the two connected volumes aren't completely isolated from surroundings. This practical limitation would result in experimental intermediary times slightly shorter than the ones in table 9.1. Still, the difference between the analytical model and the practical experiments is small.

Experimental work demonstrated that in order to obtain stable pressure cycles without an intermediary phase, the cycle times will have to be at least four times the system's molecular reactor time constant $t_p \geq 4\tau$. This is going to be one of the main conditions for thin film depositions in Pulsed-CVD reactors (also see chapter 11).

The mathematical model can be used for calculations in gas injection Pulsed-CVD where the pressures between the supply and reactor volumes instantly equilibrate, that is, where no restrictions between these two volumes are encountered.

Chapter 10

CFD simulations

Steady flow CFD simulations have been performed on the experimental Pulsed-CVD reactor in order to see what the uniformity of the gaseous N_2 flow velocities in the reactor volume are, and respectively between parallel stacked wafers.

In order to determine if the system used during the first part of this research can be scaled-up for steady flow depositions, the first set of simulations have been performed for the comparison of the gaseous N_2 flow velocities inside reactors with different geometries, at two gas inlet velocities. As expected from the steady flow CVD reactors fluid dynamics literature, the resulted gaseous N_2 flow uniformities inside different geometry reactors are very poor.

The second part of the simulation study has been done on a reactor geometry identical to the real 400 mm height reactor used in the stacked wafer experimental research for the determination of the flow uniformity in between seven parallel, 80 mm OD wafers. The simulation has been done in steady flow regime, for a gaseous N_2 inlet velocity of 12 m/s at a reactor pressure of 350 Pa. Good flow uniformities between all the wafers have been determined.

The finite volumes discretization method was employed, by using the Fluent 6.1 software package. The simulations were run inside the full reactor 3D geometries, and the flow symmetry resulted from the iterations performed initially by using the k-ε turbulence model, improved by employing in the final computations the RSM model.

In this chapter the details involved in setting the simulations, as well as the simulations results are presented.

10.1 Reactor pressure uniformity

As mentioned in chapter 4, the reactor pressure is measured at its top. To set the reactor flow conditions during simulations, the pressure at different reactor levels need to be known.

The reactor gas throughput can be calculated, by using the Poiseuille law:

$$Q_R = \frac{\pi \cdot {R_R}^4}{16 \cdot \eta_R \cdot H_R} \cdot \left({P^2}_{top} - {P^2}_{bot} \right) \tag{10.1}$$

where η_R is the viscosity of the gaseous nitrogen inside of the reactor, R_R = 59 mm is the reactor radius, H_R = 400 mm is the reactor height, P_{top} is the pressure at the top of the reactor, and P_{bot} is the pressure at the bottom of the reactor.

The same way, the exhaust system throughput can be determined:

$$Q_E = \frac{\pi \cdot {R_E}^4}{16 \cdot \eta_E \cdot L_E} \cdot \left({P^2}_{bot} - {P^2}_{pump} \right) \tag{10.2}$$

where η_E is the viscosity of the nitrogen gas inside of the exhaust system, R_E = 12.5 mm is the average radius of the exhaust system cross-section, L_E = 1000 mm is the length of the exhaust system including the vacuum trap, and $P_{pump} \cong 0$ Pa is the pressure considered at the vacuum pump inlet.

Because fluids viscosity doesn't depend on pressure, but just on temperature, and considering one of the initial assumptions we made in our experiments, namely the fact that the temperatures anywhere inside of the Pulsed-CVD system are equal to the room temperature, we can assume that the gas viscosity inside of the reactor is equal to the viscosity of the gas inside the exhaust system: $\eta_R = \eta_E$, and as the exhaust system throughput is equal to the reactor throughput, by dividing equation 10.1 to 10.2 it can be written:

$$\left(\frac{R_R}{R_E}\right)^4 \cdot \left(\frac{L_E}{L_R}\right) \cdot \frac{P^2{}_{top} - P^2{}_{bot}}{P^2{}_{bot}} = 1 \tag{10.3}$$

and after replacing the above values in equation 10.3, results:

$$P_{bot} \cong 0.999 P_{top} \tag{10.4}$$

which means that during the simulations we can consider the pressure at the bottom of the reactor as being equal to the pressure at the top of it. During simulations these are the average equivalent steady flow pressures calculated from the pulse flow experiments pressure data, by using expression 5.1.

10.2 Gas inlet velocity calculation

In order to set the reactor gas inlet boundary condition, the velocity of the gas entering the reactor had to be determined. To do this the gas inlet molecular flow rate needed to be calculated.

The reactor molecular specific rate in molecules per second and cubic meter is:

$$\dot{N} = \left(\overline{P} - P_{\min}\right) = \left(n_{av} - n_{\min}\right) \cdot \frac{R_0}{N_A} \cdot T \tag{10.5}$$

where $\overline{P}$ is the steady flow equivalent pressure, P_{min} is the pulse cycle minimum pressure, with n_{av} and n_{min} the corresponding number of molecules per unit volume, R_0 the Universal Gas Constant, N_A the Avogadro number, and T the gas temperature.

Using equation 10.5, the reactor molecular rate can be approximated:

$$\left(n_{av} - n_{\min}\right) \cdot V_R = \frac{\overline{P} - P_{\min}}{R_0 \cdot T} \cdot N_A \cdot V_R \tag{10.6}$$

where $V_R = 4.37\ 10^{-3}\ m^3$ is the volume of the reactor.

The gaseous N_2 mass flow rate trough the reactor will then be:

$$\dot{m} = \left(n_{av} - n_{\min}\right) \cdot V_R \cdot m = \left(\overline{P} - P_{\min}\right) \cdot \frac{N_A}{R_0 \cdot T} \cdot m \cdot V_R \tag{10.7}$$

where the mass of a molecule of gas, m, can be expressed as:

$$m = \frac{M}{N_A} \tag{10.8}$$

which gives:

$$\dot{m} = \left(\overline{P} - P_{\min}\right) \cdot \frac{N_A}{R_0 \cdot T} \cdot \frac{M}{N_A} \cdot V_R = \left(\overline{P} - P_{\min}\right) \cdot \frac{M}{R_0 \cdot T} \cdot V_R \tag{10.9}$$

As the molecular mass of the nitrogen gas is M = 28.03 10^{-3} kg, for our reactor at a temperature T = 293 K, the mass flow rate is:

$$\dot{m} \cong 5 \cdot 10^{-8} \left(\overline{P} - P_{\min}\right) \cdot kg / s \tag{10.10}$$

The reactor mass flow rate is equal to the mass flow rate through the ultrasonic nozzle at the reactor entrance:

$$\dot{m} = \rho_S \cdot v_S \cdot A_S \tag{10.11}$$

where ρ_S is the density of the gaseous N_2 supplied through the nozzle at the supply pressure P_S, v_S is the gas velocity through the nozzle, and A_S is the nozzle internal cross-sectional area. Given that for our system $P_S = 10^5 \div 1.5\ 10^5$ Pa, and as the nozzle internal diameter is $D_S = 10^{-3}$ m, the extreme supply velocity values found for corresponding average steady flow equivalent pressures are:

$v_{S\min} \cong 1 \cdot m/s$ for $\overline{P} = 35 \cdot Pa$, respectively $v_{S\max} \cong 12 \cdot m/s$ for $\overline{P} = 350 \cdot Pa$

10.3 Fluent simulations

10.3.a Steady flow simulations for velocity field uniformity

The steady flow simulations for velocity field uniformity simulation set has been performed on 118 mm ID reactors of three different heights: 200 mm, 400 mm and 700 mm, with two different diameter heaters: 74 mm, respectively 116 mm (figure10.1). Gas inlet velocities of 1 m/s for a reactor internal pressure of 35 Pa and of 12 m/s at a 350 Pa reactor pressure were considered.

The aim of these simulations is the numerical study of the reactor velocity field uniformity. The uniformity was computed using a relation similar to the one employed in the naphthalene samples sublimation uniformity calculation, of the form:

$$U_V = 1 - \frac{1}{n} \cdot \sum_{i=1}^{n} \left| \frac{v_i - \bar{v}}{\bar{v}} \right| \qquad (10.1)$$

In relation 10.1, v_i are the axial velocity values considered at positions similar to the ones of the naphthalene samples during the reactor volume flow field uniformity as a function of the pulse cycle length/maximum pressure experiments. That is at three different levels in the reactor vertical symmetry plane: 105 mm above the reactor base, 25 mm bellow the reactor top, and in the median position between these two levels (figure 10.1). $\bar{v}$ is the average axial velocity. Same as in the experimental section, during each simulation a number of n = 6 values was considered.

Table 10.1 contains the data used during the interpretation of the velocity field uniformity simulations set, presented in the section at the end of the chapter.

The reactor geometries and meshes have been created in Gambit 2.1. The rounded numbers of tetrahedral cells resulted after meshing the six reactor geometries (three different reactor heights, each with two different heaters inside) are presented in table 10.2.

All simulations have been run on the whole reactor geometry. In Appendix B the flow velocity paths show its symmetry as resulted after convergence by using the RSM turbulence model (on an unrefined mesh).

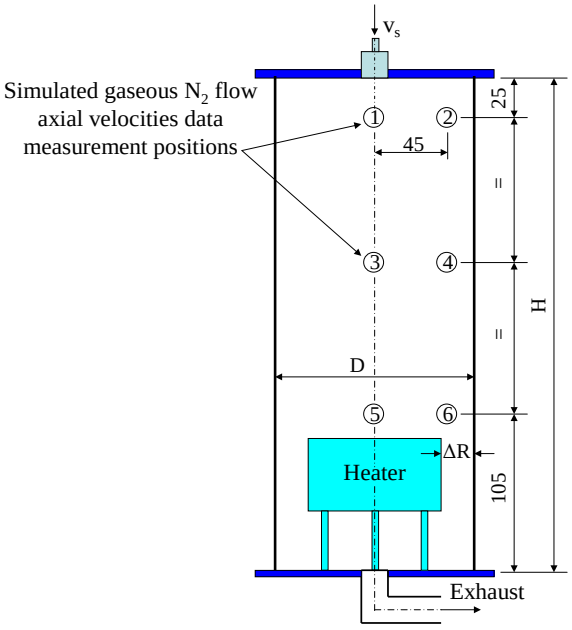

Figure 10.1 Pulsed-CVD reactor geometry for numerical simulations

Table 10.1 Numerical simulations velocity field uniformities

Simulation #	**1**	**2**	**3**	**4**	**5**	**6**	**7**	**8**	**9**	**10**	**11**	**12**
Inlet velocity v_s [m/s]	1						12					
Reactor pressure P [Pa]	35						350					
Heater diameter [mm]	74			116			74			116		
Reactor height H [mm]	200	400	700	200	400	700	200	400	700	200	400	700
Reactor-heater inter-space ΔR [mm]	22	22	22	1	1	1	22	22	22	1	1	1
H/ΔR	9.1	18.2	31.8	200	400	700	9.1	18.2	31.8	200	400	700
U_V	0.23	0.54	0.37	0.57	0.49	0.39	0.08	0.26	0.45	0.08	0.22	0.19

Table 10.2 Number of tetrahedral cells in reactor geometry meshes

Reactor height (mm)	Heater diameter (mm)	Number of cells per mesh
200	74	110 000
400	74	230 000
700	74	425 000
200	116	105 000
400	116	226 000
700	116	407 000

This set of simulations was done using the next Fluent settings:

1. Solver: Coupled Implicit, time – steady
2. Energy Equation: Off
3. Turbulence Model: Reynolds Stress Model, wall boundary conditions from k equation, standard wall functions
4. Materials: Gaseous N_2, with densities of $\rho_{35Pa} = 0.0004$ kg/m^3 / $\rho_{350Pa} = 0.004$ kg/m^3 at equivalent operating pressures of 35 Pa / 350 Pa
5. Operating Pressures: 35 Pa / 350 Pa, absolute pressures
6. Inlet Boundary Conditions: Velocity $v_S = 1$ m/s / $v_S = 12$ m/s with direction on negative Y axis, Turbulence Intensity $T_i = 4$ % (the value commonly used for flow in circular pipes), Hydraulic Diameter $H_D = 0.118$ m
7. Outflow Boundary Condition: Flow Rate Weighting = 1
8. Default: Under-Relaxation Factors, Discretization Schemes, and Courant number

Simulations flow velocity paths lines and velocity filed values are presented in the first section of appendix B.

10.3.b Steady flow simulation for flow uniformity between stacked wafers

CVD literature [8] show that the deposition uniformities between wafers positioned inside steady flow LPCVD reactors is a function only of the precursor diffusion at the substrate, with no precursor velocity influence, as the velocity gradients at the wafer substrate are very low. In these reactors, the velocities between the wafers are considered to be equal and close to zero.

A steady flow Fluent simulation was done on the 118 mm ID, 400 mm height reactor containing a stack of seven 5 mm thick, 80 mm OD horizontal wafers, positioned the same way as during the stacked wafer experiments. Chapter 3 details the way the wafers were dimensioned and arranged inside the reactor. The wafers order in the simulation is 1 to 7, from the top-down.

As the simulation was done at an equivalent steady pressure of 350 Pa, an inlet velocity of 12 m/s was considered.

The reactor geometry and mesh have been created in Gambit 2.1. The grid consists in a number of close to 250 000 tetrahedral cells. In Fluent the grid cells have been scaled, checked, smoothed and swapped.

This simulation was done using the next Fluent settings:

1. Solver: Coupled Implicit, time – steady
2. Energy Equation: Off
3. Turbulence Model: Reynolds Stress Model, wall boundary conditions from k equation, standard wall functions
4. Materials: Gaseous N_2, with a density of ρ_{350Pa} = 0.004 kg/m^3 at an equivalent operating pressure of 350 Pa
5. Operating Pressure: 350 Pa, absolute pressure
6. Inlet Boundary Conditions: Velocity v_S = 12 m/s with direction on negative Y axis, Turbulence Intensity T_i = 4 % (the value commonly used for flow in circular pipes), Hydraulic Diameter H_D = 0.118 m
7. Outflow Boundary Condition: Flow Rate Weighting = 1
8. Default: Under-Relaxation Factors, Discretization Schemes, and Courant number

Simulations flow velocity paths lines and values between wafers are presented in the second section of appendix B.

10.4 Simulation conclusions

The first simulation set show that the reactor pressure - velocity field uniformity dependence, is much more important than the uniformity dependence on the reactor geometrical characteristics. This can be seen in the graphs in figures 10.2 and 10.3, where in equivalent reactor geometry simulations at the two different pressures employed, the velocity field uniformities differences between the high/low pressure regimes reach 50 %. The simulations also show in all different considered conditions poor velocity field uniformity, with maximum values of 57 %.

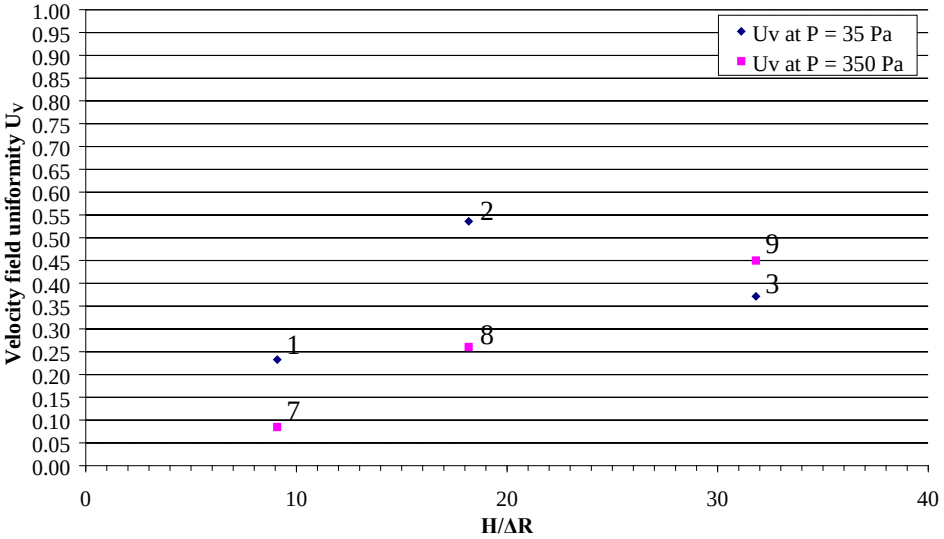

Figure 10.2 Reactor steady flow velocity field uniformities in the small heater configuration, at reactor pressures of 35 Pa and 350 Pa

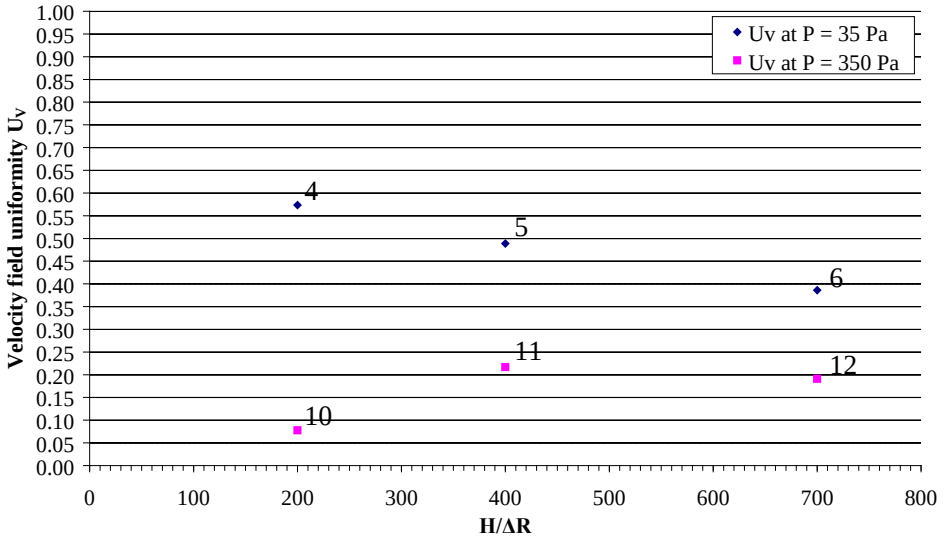

Figure 10.3 Reactor steady flow velocity field uniformities in the big heater configuration, at reactor pressures of 35 Pa and 350 Pa

For steady flow depositions this type of reactor is not industrially scalable. In order to properly manufacture a larger system, first a prototype would need to be built. On the prototype, simulations will need to be performed, followed by reactor vessel modifications in order to obtain uniform film depositions. This is the way current CVD reactors manufacturing technology works.

Not all simulations have been experimentally validated. However, during the reactor volume flow field uniformity as a function of the pulse cycle maximum pressure experimental set (chapter 11) it is shown that, for the 400 mm height reactor - small heater geometry, poor steady flow maximum flow field uniformities, of only 50 %, can be reached. Further experimental work, for other reactor geometries and higher pressures is proposed for better flow field characterization.

From the numerical simulations work we can make a general idea of the local Re number on each cylinder. However the sublimation rate also depends on the bulk concentration and much more localized effects than CFD can show (refer back to paragraph 3.1).

The steady flow simulation for flow uniformity between stacked wafers was run in order to find the gaseous N_2 axial velocity values between seven wafers of 80 mm OD, for reactant inlet velocity of 12 m/s, inside the 400 mm height reactor.

The simulation shows good flow axial velocity uniformities between the wafers, with velocity values close to zero at the positions where the substrates are to be installed (figure 10.5).

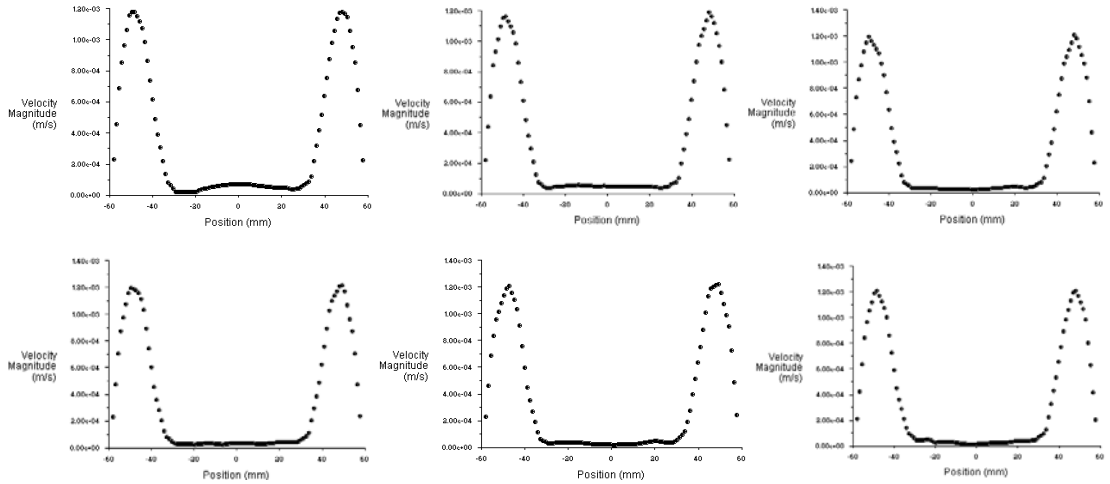

Figure 10.4 Gaseous N_2 flow axial velocities in the vertical symmetry plane between the seven stacked wafers, starting with the space between the first two top wafers (upper-left corner), to the space between the two bottom wafers (lower-right corner), inside the 400 mm height reactor, at reactant inlet velocity of 12 m/s

This was expected from the LPCVD reactors experience [6, 7, 8]. The flow uniformity between wafers is good even if the reactor pressure used in the simulation is still quite high. In LPCVD reactors these pressures are smaller (depending on the film deposition requirements), and better uniformities are expected, with the deposition uniformity having a higher dependence on the reactants diffusion through the boundary layers, than on the flow field uniformity.

The simulation was validated by the stacked wafer experimental set (chapter 11), where the flow uniformity between wafers is good not only in the pulse flow experiments at increased reactor pressures, but during equivalent steady flow experiments as well.

Chapter 11

Experimental data interpretation

11.1 Reactor volume flow field uniformity as a function of the pulse cycle length

In order to characterize the flow field inside Pulsed-CVD reactors, during this research three sets of experiments have been run.

The reactor volume flow field uniformity as a function of the pulse cycle length set consisted in a number of over 100 experiments (including the preparatory ones) in pulse flow conditions and in equivalent steady flow regimes. One reason these experiments were run was to determine the shortest cycle time for which the naphthalene samples sublimation uniformity still keeps in the high values range. The second purpose was to compare the pulse regime 3D flow field uniformities with the 3D flow field uniformities during equivalent steady flow experiments.

The uniformity of the flow field was ascertained by computing, as explained in chapter 8, the sublimation uniformity of six naphthalene samples, positioned on a stainless steel wire frame.

The maximum pulse cycle pressures reached during this experimental set have been quite low, of less than 1 kPa. The pulse flow cycle time durations have been calculated as multiples of a lower time constant ($\tau = 5$ s), as the minimum pressure achieved by the system after pulse cycles with a duration of $t_p = 4\tau$, was in the range of $P_{min} = 1.1\ P_u$ (where P_u is the reactor ultimate pressure).

For each subset, the cycle times have been varied from 0.15 to 4 times τ, with one experiment, in the fourth subset, at 5 times τ. The uncompensated/compensated samples sublimation uniformities, the equivalent steady pressures, and the non-dimensional fluxes J_C^* have been computed for each experiment.

The steady flow equivalent pressures ($\overline{P}$ in previous calculations, same to $P_{eq.steady}$ in the experimental data) have been calculated using equation 5.1 for the whole period of the stable limit pulse flow cycles (25 minutes in each pulse flow experiment).

The experimental parameters values are given in tables C.1 to C.4, appendix C. The graphs drawn by using this data analyze the cycle length effect on the reactor volume flow field uniformity, and are shown in the first section of the same appendix.

The last experimental subset doesn't include all the steady flow experiments. The reason of not considering them was that at the one second relatively high injection time the naphthalene sublimation would be influenced into a greater extent by this pressure rising part of the pulse cycle, so we relied in interpretations on the first three subsets. Still, the last subset offers a complete view when comparing the sublimation uniformities between pulse flow experiments at different injection times.

The uncompensated uniformities are the ones computed for the full experiment duration, of 30 minutes. The compensated sublimation uniformities have been calculated for the stable pulse cycle period, of 25 minutes. For each naphthalene sample the compensation was calculated by subtracting the specific sublimations during the reactor pump-down (the first part of the experiment with a duration of 5 minutes) from the total specific sublimation of the sample during the 30 minutes experiment. Differences of maximum 3 % resulted between correspondent uncompensated/compensated uniformities.

The first two major findings of the research are that in Pulsed-CVD maximum flow field uniformities are obtained for cycle time values of minimum four times the reactor molecular time constant $\boxed{t_p / \tau \geq 4}$ (figure 11.1), and of over 25 times the cycle injection time $\boxed{t_p / t_i > 25}$ (figure 11.2). In chapter 9 it was also showed that by running the Pulsed-CVD in these conditions, the pulse cycle regime is stable for the whole time of the process, without including any intermediary (pressure rising) stage.

These are the two general time rules to be followed during Pulsed-CVD depositions.

A comparison between uncompensated sublimation uniformities, inside the 400mm height reactor with the small (74 mm diameter heater), during pulse flow regimes at injection times of 0.2 s, 0.4 s, 0.8 s, and 1 s, between cycle times of 5τ down to 0.15τ, are plotted in figures 11.1 and 11.2.

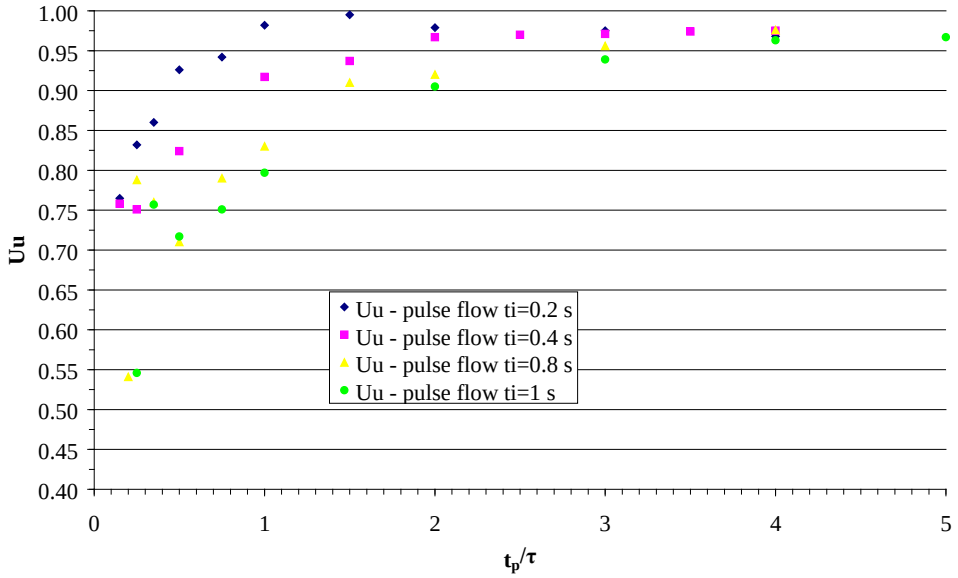

Figure 11.1 Uncompensated sublimation uniformity comparison between pulse flow experiments at injection times of 0.2 s, 0.4 s, 0.8 s, and 1 s, at cycle times of 5τ down to 0.15τ as a function of the cycle length

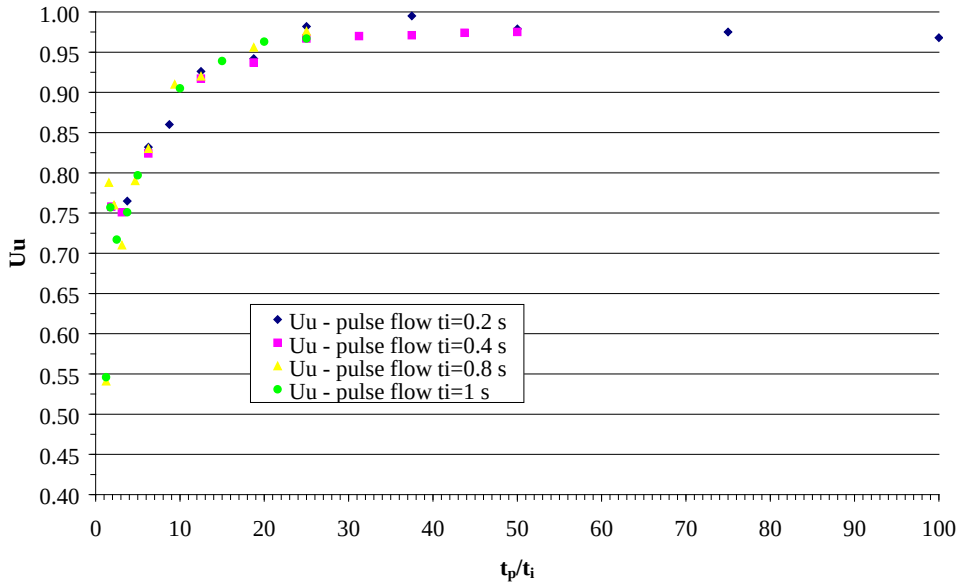

Figure 11.2 Uncompensated sublimation uniformity comparison between pulse flow experiments at injection times of 0.2 s, 0.4 s, 0.8 s, and 1 s, at cycle times of 5τ down to 0.15τ, as a function of the ratio between the cycle time and the injection time

The pulse cycle minimum/maximum pressures, and implicitly the equivalent steady flow pressures are taking increasingly higher values as the cycle times are reduced, at all the four injection time values used during the first set of experiments. For injection times of 0.2 s this can be seen in the graph from figure 11.3. The graph also show the pressure differences decrease between the minimum and maximum pressures as the cycle time decreases, which has as consequence the reactor molecular flux rate decrease. Also, for cycle lengths higher than four, the cycle's minimum/maximum pressures remain constant. These variations have been analytically modelled in chapter 9.

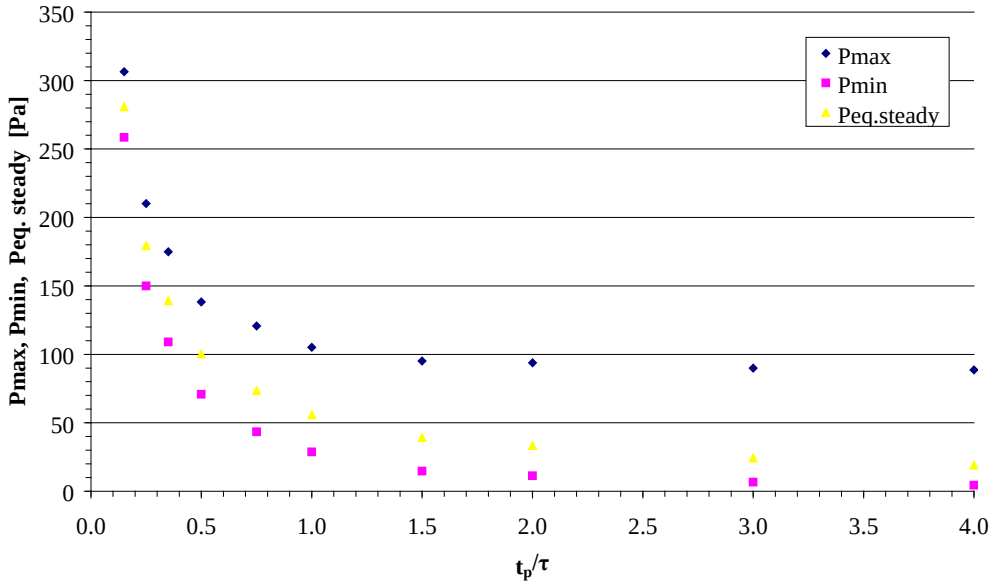

Figure 11.3 Reactor maximum, minimum, and equivalent pressures for value of t_p increasing from 0.15τ, to 4τ, at an injection time $t_i = 0.2$ s, pulse flow experiments

For extremely small cycle length experiments (the ones towards the end of the experimental data tables), the maximum/minimum pressures start to decrease. This is caused by the fact that the cycle times have been reduced to values where the cycle pump-down time (same to the time during which the gas shot tube is filled with gas at the supply pressure) becomes so short that the gas shot is filling at lower pressures (than the gage supply pressure of 400 kPa). The phenomenon can be observed in experiments 01-99 and 01-110. This is the limit where the delivery system runs outside its design capabilities.

11.2 Reactor volume flow field uniformity as a function of the pulse cycle maximum pressure

During the reactor volume flow field uniformity as a function of the pulse cycle maximum pressure set, a number of 16 pulse flow and equivalent steady flow regime experiments have been run.

Their scope was the comparison between steady/pulse flow reactor 3D flow field uniformity at consecutive increased reactor pressures, for equal pulse flow regime cycle times. In order to reach higher pulse flow maximum pressures, the gas injection experimental apparatus set-up was used.

The cycle time during the pulse flow experiments was set at a constant value, of four times the reactor molecular time constant τ = 6.6 s, analytically computed in chapter 7. This resulted in a cycle time $t_p = 4\tau = 26.4$ s. A short (relative to the total cycle time t_p) injection time t_i = 0.5 s, with a maximum gage supply pressure of 400 kPa, have been employed during the pulse flow experiments.

Same as in the reactor volume flow field uniformity as a function of the pulse cycle length set, the experiments duration was of 30 minutes each, with an initial 5 minutes reactor pump-down period, both in pulse or steady flow. The same parameters have been computed, and the naphthalene samples have been hanged on the stainless steel wire frame in the same positions.

This set experimental data is presented in table C.5. In the table it can be seen that the highest value the reactor pulse regime maximum pressure reached was of 13 709.2 Pa (close to 100 Torr). These are the data values used to draw the sublimation uniformities graphs in the second section of appendix C. The compensated sublimation uniformities have been computed from the uncompensated uniformities as shown in the first experimental set and in chapter 8.

In the graph from figure 11.4 it can be seen that the samples sublimation uniformities are almost 100% better in pulse flow regime than in the steady flow regime, with very good pulse flow sublimation uniformities, in the range of 86 % to 91 %.

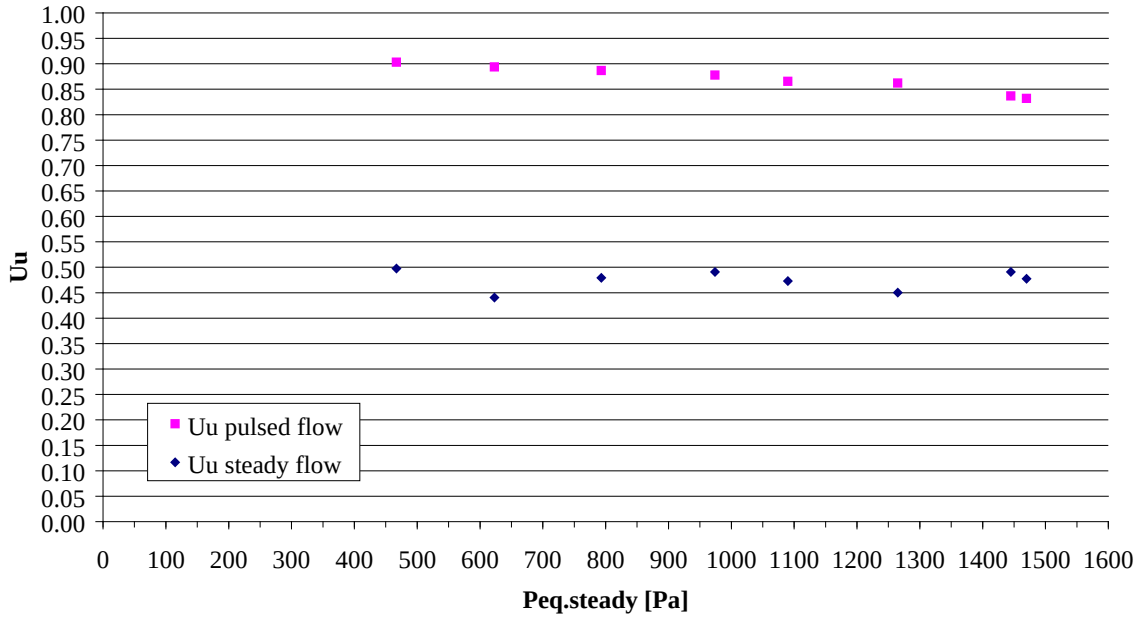

Figure 11.4 Uncompensated sublimation uniformities comparison between pulse flow experiments and equivalent steady flow experiments for continuously increased reactor pressures

In table C.5 it can be seen that, for maximum pulse flow reactor pressures of up to 100 Torr, the minimum pressures reached during pulse flow experiments, for cycle times of four times the reactor molecular time constant, are close to the reactor ultimate pressure. This proves that pulse flow depositions that require pressures up to 100 Torr can be done in optimum conditions, with very good 3D flow field uniformity, at this cycle time value.

For higher pressures flow field characterisation, further experiments would be required. However, a large number of CVD thin films are deposited at lower pressures than 100 Torr [30].

11.3 Stacked wafer flow uniformity

Same as in the reactor volume flow field uniformity as a function of the pulse cycle maximum pressure, during this third experimental set, 16 pulse flow and equivalent steady flow regime experiments have been run.

Their scope was the comparison of the flow field uniformity in pulse/steady flow experiments between seven deposition wafers stacked normal to the flow direction, at consecutive increased reactor pressures, for equal cycle times in the pulse flow regime. As in the second experimental set, the gas injection experimental apparatus set-up has been used.

The cycle time during the pulse flow experiments was set at the same constant value, of four times the reactor molecular time constant: $t_p = 4\tau = 26.4$ s. A short injection time $t_i = 0.5$ s, with a maximum gage supply pressure of 400 kPa, have been employed.

Same as in the two previous sets, the experiments duration was of 30 minutes each, with a 5 minutes reactor pump-down period at the beginning of each experiment, both in pulse or steady flow. The same parameters have been computed. Here the naphthalene samples have been hanged between the deposition wafers. Their exact position is shown in chapter 3.

The experimental data is shown in table C.6. These are the data values used to draw the sublimation uniformities graphs presented here and in the third section of appendix C. The compensated sublimation uniformities have been computed from the uncompensated ones as in the first two sets.

The highest value the reactor pulse regime maximum pressure reached was of 14 766.5 Pa (just above 100 Torr).

In figure 11.5 the samples sublimation compensated uniformities are plotted. They are the same in both pulse and steady flow experiments. Pulsed-CVD can be at least as good as the steady flow LPCVD reactors in regards of the flow field uniformities for depositions between stacked wafers.

In table C.6 can also be seen that, for maximum pulse flow reactor pressures of up to 100 Torr, the minimum pressures reached during pulse flow experiments, for cycle times of four times the reactor molecular time constant, are close to the reactor ultimate pressure.

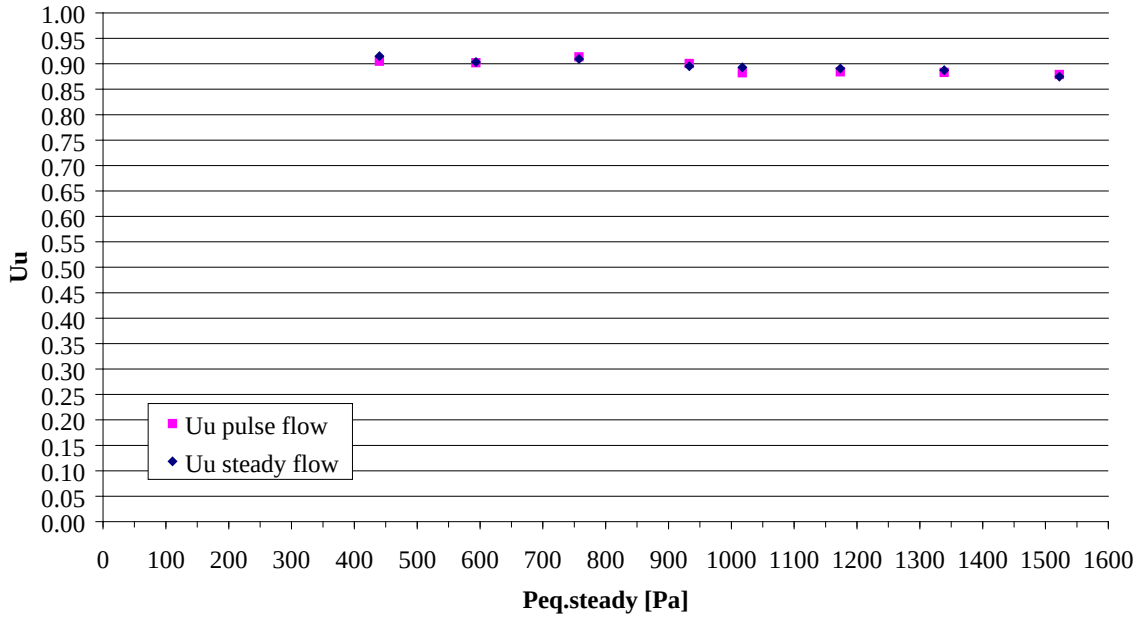

Figure 11.5 Uncompensated sublimation uniformities of samples positioned between horizontal stacked wafers; comparison between pulse flow experiments and equivalent steady flow experiments for increased reactor pressures

Chapter 12

Conclusions

This thesis presents an investigation of the flow field mass transport uniformity for Pulsed-Chemical Vapour Deposition (Pulsed-CVD) reactors as a function of geometric design parameters and processing variables. The reactor geometry variables are height and diameter of the vertical reactor, the diameter of the substrate heater relative to the reactor diameter, and the configuration of multiple wafer stacks. Process design variables are pump speed, reactor volume, and vacuum system conductance. The processing variables are the pulse timing, and the pulse cycle maximum/minimum pressures. A measure for the flow field uniformity was developed from the naphthalene sublimation technique which was used to evaluate both pulse pressure and steady flows. The steady flow condition was further investigated through numerical simulation using the commercial software package Fluent 6.1.

The purpose of the research was to provide empirical definition of the design space and operating regime for uniform deposition conditions in Pulsed-CVD reactors. The conditions for mass transport uniformity found through this research will be used in future Pulsed-CVD systems design, operation and industrial scale-up. In CVD processing, the uniformity of the precursor mass transport is a critical issue which leads to great expense and difficulty in development of new materials for new thin film devices. The results of this research may enable development of flexible, controllable, and economical manufacture of modern high-tech devices in New Zealand and other small countries.

At the beginning of the thesis, the Pulsed-CVD process is briefly described, and the CVD technology and applications are reviewed. The CVD technologies currently used in industry are presented, with emphasis on the thermal CVD reactor design and operation. The CVD mass-transport mechanisms are detailed for a better understanding of the physical processes involved in the CVD process.

In the experimental section, the naphthalene sublimation experimental technique is described, and the background theory of the heat and mass transfer analogy are presented. The experimental apparatus and technical characteristics of each of its components are detailed. The experimental method, procedure, and the settings for the experimental apparatus are also included.

The Pulsed-CVD background, including all the parameters involved in the analytical and experimental calculations, as well as the ones used for the CFD simulations are presented in the theoretical and modelling sections. The mathematical algorithms used to compute the process pressures, and molecular fluxes are developed. The sublimation uniformity computation statistical method employed for evaluation of different process regimes, and the analytical model describing the reactor pressure during the pulse cycle are explained. Numerical simulations for steady flow are presented including the finite volume software settings and boundary conditions, analytical computation algorithms, and geometry generation.

The findings of the experimental work are presented in the results sections. It was found that the pulse pressure mass transport flow field is more uniform than an equivalent steady flow field for all processing ranges. The Pulsed-CVD uniformity is very high when the cycle time is greater than or equal to four times the pump-down time constant for all pulse peak pressures, even up to 100 Torr, and the cycle time is at least 25 times the cycle injection time. The flow uniformities between deposition wafers were found to be very good in pulse flow, the Pulsed-CVD uniformities proving to be at least as good as the ones in LPCVD reactors. Thus, the operating regime for uniform thin film deposition by Pulsed-CVD has been determined, and the two operating restrictions are on the pulse timing and injection length, indicating that any Pulsed-CVD process is scalable:

$$\boxed{t_p / \tau \geq 4}$$

and

$$\boxed{t_p / t_i > 25}$$

The results of the stacked wafer investigation verify design criteria for pulsed uniformity as well as providing a validation of our implementation of the naphthalene sublimation technique as a measure of local convective mass transfer uniformity. The geometry of the stacked wafers was determined from standard design relations for steady Low Pressure CVD. Good uniformity was expected in steady flow because diffusion process was controlled by the wafer spacing. The measured uniformity, derived from the naphthalene sublimation was above 0.9 for both LPCVD and the Pulsed-CVD for $t_p \geq 4\tau$ and $t_i \leq 25t_p$.

Pulsed-CVD uniformities are better as the convective uniformities are achieved by domination of expansion effects over viscous forces.

12.1 Future work

It is the author's opinion that future Pulsed-CVD work should include:

1. Flow field characterization throughout the reactor for different reactor geometries and for maximum pulse flow cycle pressures above 100 Torr.

2. Flow field characterization for different substrate geometries, either plane, or three-dimensional.

3. Experimental apparatus improvements, with solutions for bringing the different geometry substrates at uniform deposition temperatures and measurement of all process parameters.

4. Experimental study of the reactor flow field by employing suitable visualisation techniques.

5. Experimental studies for films growth rates and morphology control in order to determine the optimum process parameters for depositing films with specific properties.

References

1. A. Roth, *Vacuum Technology*, North-Holland, Amsterdam (1982)
2. A. Chambers, R.K.Fitch, and B.S. Halliday, *Basic Vacuum Technology*, Adam Hilger, Bristol (1989)
3. J.M. Lafferty, *Foundations of Vacuum Science and Technology*, John Wiley & Sons, New York (1998)
4. C.E. Morosanu, *Thin Films by Chemical Vapor Deposition*, Elsevier, Amsterdam (1990)
5. H.O. Pierson, *Handbook of Chemical Vapor Deposition (CVD) Principles, Technology and Applications, 2nd edition*, Noyes Publications, New York (1999)
6. D.L. Smith, *Thin-Film Deposition Principles and Practice*, McGraw-Hill, Boston (1995)
7. A.Elshabini-Riad and F.D. Barlow, *Thin Film Technology Handbook*, McGraw-Hill, New York (1998)
8. M. Ohring, *Materials Science of Thin Films, 2nd edition*, Academic Press, San Diego (2002)
9. H.K. Versteeg and W. Malalasekera, *An introduction to computational fluid dynamics. The finite volume method*, Longman Scientific & Technical, New York (1995)
10. W. Shyy, S.S. Thakur, H. Ouyang, J. Liu, and E. Blosch, *Computational Techniques for Complex Transport Phenomena*, Cambridge University Press (1997)
11. F.P. Incropera and D.P. Dewitt, *Fundamentals of heat and mass transfer*, John Wiley and Sons, New York (2002)
12. J.R. Taylor, *An Introduction to Error Analysis*, University Science Books, California (1982)
13. F.M. White, *Fluid Mechanics*, McGraw-Hill, Boston (1999)
14. L. Perko, *Differential Equations and Dynamical Systems*, Springer-Verlag, New York (1991)

15. S.P. Krumdieck, O. Sbaizero, and R. Raj, Unique Precursor Delivery and Control Afforded by Low-Pressure Pulsed-CVD Process with Ultrasonic Atomization, *Journal de Phisique IV*, **11** (PR3) 1161-1168 (2001)

16. S.P. Krumdieck, J.Y. Lee, and H. Raatz, Uniform Molecular Flux in a Vertical Reactor with Pulsed Transition Regime Gas Flow, *Electrochemical Society Proceedings*, **8** (2003)

17. S.P. Krumdieck, Kinetic model of low pressure film deposition from single precursor vapour in a well-mixed, cold-wall reactor, *Acta Materialia*, **49** 583-588 (2001)

18. S.P. Krumdieck and R. Raj, Experimental Characterization and Modeling of Pulsed MOCVD with Ultrasonic Atomization of Liquid Precursor, *Chemical Vapor Deposition*, **7** (2) 85-90 (2001)

19. S.P. Krumedieck, O. Sbaizero, A. Bullert, and R. Raj, YSZ layers by pulsed-MOCVD on solid oxide fuel cell electrodes, *Surface and Coatings Technology*, **167** 226-223 (2003)

20. S.P. Krumdieck and R. Raj, Groth Rate and Morphology for Ceramic Films by Pulsed-MOCVD, *Surface and Coatings Technology*, **141** 7-14 (2001)

21. S.P. Krumdieck, O. Sbaizero, A. Bullert, and R. Raj, Solid Yttria-Stabilized Zirconia Films by Pulsed Chemical Vapor Deposition from Metal-organic Precursors, *Journal of the American Ceramic Society*, **85** (11) 2873-75 (2002)

22. S.P. Krumdieck and R. Raj, Conversion Efficiency of Alkoxide Precursor to Oxide Films Grown by an Ultrasonic-Assisted, Pulsed Liquid Injection, Metalorganic Chemical Vapor Deposition (Pulsed-CVD) Process, *Journal of the American Ceramic Society*, **82** (6) 1605-07 (1999)

23. P.R. Souza Mendes, The Naphthalene sublimation technique, *Experimental Thermal and Fluid Science*, **4** 510-523 (1991)

24. S.L. Thompson and W.R. Owens, A Survey of Flow at Low Pressures, *Vacuum*, **25**, (4) 151-156 (1975)

25. G. Asano, T. Oikawa, K. Tokita, K. Okada, and H. Funakubo, Low-Pressure Deposition of $Pb(Zr,Ti)O_3$ Films by MOCVD at Low-Temperature, *Transactions of the Materials Research Society of Japan*, **27** (1) 223-226 (2002)

26. K. Nagashima, M. Aratani, and H. Funakubo, Improvement of Property of Pb(ZrxTi1-x)O_3 Thin Film Prepared by Source Gas Pulse-Introduced Metalorganic Chemical Vapor Deposition, *The Japan Society of Applied Physics*, **39** (2) 996-998 (2000)

27. K. Kim and K. Young, Highly conformal Cu Thin-Film Growth by Low-Temperature Pulsed MOCVD, *Electrochemical and Solid-State Letters*, **6** (8) 106-108 (2003)

28. J-P. Senateur, C. Dubourdieu, F. Weiss, M. Rosina, and A. Abrutis, Pulsed Injection MOCVD of Functional Electronic Oxides, *Advanced Materials for Optics and Electronics*, **10** 155-161 (2000)

29. H.H. Hoang and I-M. Chen, Optimal Synthesis for Workspace and Manipulability of Parallel Flexure Mechanism, *Proceedings of the 11th World Congress in Mechanism and Machine Science*, China Machinery Press (2003)

30. S.P. Krumdieck, *Experimental Characterisation and Modelling for the Growth Rate of Oxide Coatings from Liquid Solutions of Metalorganic Precursors by Ultrasonic Pulsed Injection in a Cold Wall Low Pressure Reactor,* PhD Thesis, Univ. of Colorado - Boulder (1999)

31. H. Raatz, *Experimental Characterization of Flow Dynamics in a low pressure reactor with pulsed injection MOCVD*, Master Thesis, Technical University of Darmstadt (2002)

32. S.P. Krumdieck, S. Baluti and L. Markus, *A study of Flow Field Dynamics of Pulsed – Chemical Vapour Deposition*, draft article

33. W.M. Kays and M.E. Crawford, *Convective Heat and Mass Transfer*, *2nd edition*, McGraw-Hill (1980)

34. W. Merzkirch, *Flow Visualization*, Academic Press, Orlando (1987)

35. A.J. Smiths and T.T. Lim, *Flow Visualization*, Imperial College Press, London (2000)

Appendix A

CVD materials and their applications

A.1 The CVD of metals

Material	*Applications*
Aluminum	- metallization of semiconductor devices and replacement of evaporated or sputtered films to improve conformal uniformity - coating of carbon fibers for composite fabrication - corrosion and oxidation protection of steel - alloyed with Copper for semiconductor metallization
Beryllium	- First wall coatings for fusion reactors
Chromium	- Corrosion protection and oxidation protection of steels and other metals - Experimental contact metallization in integrated electronic circuits
Copper	- conductive coatings for semiconductor applications - alloying element with CVD Aluminum to reduce electro migration
Gold	- contact metallization and metallization of alumina in semiconductor applications
Molybdenum	- integrated circuits (IC's) contact and gate metallization - Schottky contact metallization - erosion resistant coatings for gun steel barrels deposited with carbonyl precursor - coatings for fotothermal solar converters with high infrared reflectance - freestanding shapes such as tubes and rods
Nickel	- molds, dies, and other forming tools for metal and plastic processing, especially those involving irregular surfaces and internal areas - high strength structural parts when alloyed with small amounts of Boron - contacts for electronic applications (alloyed with Palladium)
Niobium (Columbium)	- coatings for nuclear fuel particles - cladding for steel and copper tubing for chemical processes
Platinum and Platinum group metals (Iridium, Rhodium and Ruthenium)	- coatings for high temperature crucibles - catalyst in fuel cells and automobile emission control - ohmic and Scottky diode contacts - diffusion barrier metallization

Rhenium	- heaters for high temperature furnaces - boats, crucibles, tubes and other freestanding shapes - contacts and diffusion-barrier metallization and selective deposition on Silicon in semiconductor applications (experimental) - thermocouple sheaths
Tantalum	- thin film capacitors - corrosion resistant coatings - ordnance devices
Titanium	- production of metal foil and shapes - corrosion resistant coatings on steel and other substrates - preparation of Titanium aluminides - diffusion barrier in semiconductors
Tungsten	- replacement of Aluminum and general metallization of integrated circuits - selective deposition via plugs and gate electrodes for very large scale integrated circuits - diffusion barriers between Silicon and Aluminum in integrated circuits - thermionic cathodes (co-deposited with Thorium) - coating for targets for X-ray cathodes (co-deposition with Rhenium) - selective absorber coatings for solar energy collectors

A.2 The CVD of intermetallics

Material	*Applications*
Titanium Aluminides	- Ti3Al and TiAl have excellent high temperature oxidation resistance owing to the formation of a thin alumina layer on the surface - potential applications in aerospace structures
Ferro-Nickel	
Nickel-Chromium	
Tungsten-Thorium	- long life thermionic cathode emitters for high-power applications in high-frequency tubes
Niobium-Germanium	- niobium germanide NbGe is a superconductor with a high transition temperature (T_c = 20 K)

A.3 The CVD of the allotropes of carbon

Material	*Applications*
Graphite	- boats and crucibles for liquid phase epitaxy - crucibles for molecular beam epitaxy - electrodes for plasma etching - reaction vessels for gas-phase epitaxy of III-V compounds - trays for Silicon wafer handling - heating elements for high temperature furnaces - coating for fusion reactors - coating for nuclear-fuel particles - chemical vapor infiltration of carbon-carbon structures (reentry heat shields, rocket nozzles, and other aerospace components) - aircraft disk brakes - biomedical devices, heart valves, implants
Diamond	- grinding, cutting (inserts, twist drills, whetstones, industrial knives, circuit-board drills, oil-drilling tools, slitter blades, surgical scalpels, saws) - wear parts (bearings, jet-nozzle coatings, slurry valves, extrusion dies, abrasive pump seals, computer disk coatings, engine parts, medical implants, ball bearings, drawing dies, textile machinery) - acoustical (speaker diaphragms) - diffusion, corrosion (crucibles, ion barriers – Sodium, fiber coatings, reaction vessels) - optical coatings (laser protection, fiber optics, scanners, lenses, antireflection, UV to IR windows, X-ray windows, radomes) - photonic devices (radiation detectors, switches) - thermal management (heat-sink diodes, heat-sink PC boards, thermal printers, target heat-sinks) - semiconductor (high-power transistors, high-power microwave, photovoltaic elements, field-effect transistors, UV sensors)
Diamond-like-Carbon	- erosion / corrosion protection for machinery and bearing surfaces - anti-reflection coating with an adjustable index of refraction for Germanium, Magnesium Fluoride, Cadmium Telluride, Zinc Sulfide, and Zinc Selenide IR windows - laser-damage coatings for high-power laser windows - etching mask for X-ay lithography - coatings for hip-joints, heart valves, and other prostheses (DLC is biocompatible and blood compatible) - coating for tissue culture flask, micro-carriers, cell culture containers, etc.

A.4 The CVD of non-metallic elements

Material	*Applications*
Boron	- production of Boron fibers on W or C core - coatings for the first wall of fusion reactor - dopant in Silicon semiconductor films
Silicon	- epitaxial Silicon (digital bipolar integrated circuits, linear digital metal-on-Silicon (MOS), discrete linear digital MOS, complimentary MOS (CMOS)) - polysilicon (gate electrodes, interconnection conductors, resistor and emitter contacts, thermal and mechanical sensors, photovoltaic cells - amorphous Silicon (photovoltaic devices, photocopier drums)

A.5 The CVD of ceramic materials: Carbides

Material	*Applications*
Boron Carbide	- coating for shielding against neutron radiation - coating for neutron flux control in nuclear reactors - wear parts, sandblast nozzles, seals - mortar and pestle - high-grade abrasive and lapping powder - high-temperature thermocouple - lightweight body and airborne armor - matrix materials for ceramic composites - coating for nozzles, dressing sticks for grinding wheels
Chromium Carbide	- special coating for maximum chemical resistance - intermediate layer for tool steel coatings
Hafnium Carbide	- oxidation resistant coatings for carbon-carbon composites (co-deposited with SiC) - production of whiskers (with Nickel catalyst) - coating for super alloys - coating on cemented carbides - HfC-NbC solution as coating for tools
Niobium Carbide	NbC has only limited industrial uses. It is found mostly in combination with TaC in 10, 20, or 50 wt% NbC. The following is a summary of its applications in production or development. - in special grades of cemented carbides in combination with alumina - with TaC to improve the proprieties of cemented carbides - hard coating for protection of niobium metal - as a carbonitride for superconductor applications

Silicon Carbide	- low-weight, high-strength mirrors - high-power, high-frequency, and high-temperature semiconductor devices - radiation-resistant semiconductors - radiation sensors (amorphous SiC) - fibers and whiskers - matrix in ceramic composites - catalytic support for automobile exhaust - thermocouple sheath - lightweight armor - coatings for susceptors and heating elements for epitaxial Silicon deposition - coatings for fusion reactor applications - coatings for ceramic heat exchanger ceramic tubes - oxidation resistant coatings for carbon-carbon composites - heteroepitaxial deposit on Silicon - blue light-emitting diodes (LED)
Tantalum Carbide	- coating on Tantalum metal to improve chemical resistance, high temperature hardness, and wear and oxidation resistance.
Titanium Carbide	- secondary carbide in cemented carbides - coatings for cutting and milling tools in inserts - coatings for stamping, chamfering and coining tools - ball-bearing coatings - coatings for extrusion and spray gun nozzles - coatings for pump shafts, packing sleeves, and feed screws for chemical industry - coatings for molding tools and kneading elements for plastic processing - molded bipolar plates for high-voltage battery and fuel power sources - coatings for fusion reactor applications
Tungsten Carbide	- major industrial material used extensively in cemented carbides for cutting tools - production of submicron powder for hot pressing or hot isostatic pressing of high-precision tooling - coating of fine-porosity carbon for catalytic applications
Zirconium Carbide	- coating for atomic-fuel particles (Thoria and Urania) for nuclear-fission power plants

A.6 The CVD of ceramic materials: Nitrides

Material	*Applications*
Aluminium Nitride	- heat-sink substrates and packing materials for electronic devices (major application) - passivation and dielectric layers - high-frequency acoustic wave devices (piezoelectric) - traveling-wave tubes - microwave-absorbing components - experimental high-power and high-temperature material for electronic and optoelectronic devices, especially in the UV region of the spectrum
Hexagonal Boron Nitride	- powder for lubricants and additives - radar windows and antennas - crucibles for Aluminum evaporation and for molecular beam epitaxy - vessels for Czochralski crystal growth of III-V and II-VI compounds (i.e. Gallium Arsenide) - insulating substrate in ribbon heaters in combination with a pyrolytic graphite resistance heating element
Cubic Boron Nitride	- cutting and grinding applications
Hafnium Nitride	- tribological and corrosion resistant coatings - diffusion barriers for microelectronic devices (experimental) - whiskers - coatings on Tungsten wires - coating for cutting tools
Niobium Nitride	- as a potential superconductor coating - diffusion barrier in semiconductors (experimental)
Silicon Nitride	- structural and chemical resistance applications - film in semiconductor devices - crucibles for Silicon single-crystal processing - crucibles and vessels for handling corrosive chemicals and molten metals - high-temperature gas turbine components - diesel-engine components - rotors for turbocharger - cutting tools (Si_3N_4 and Sialons) - components for welding, tube drawing and extruders - ball and roller bearings - bearing seals and check valves - blast nozzles - thermocouple tubes - heat exchangers, pumps and seal faces - passivation layers, multilayer resist stacks, diffusion barriers, interlevel dielectrics, side-wall spacers, trench masks, oxidation masks, etc., in semiconductor devices - whiskers for height strength reinforcement

Titanium Nitride	- the most important interstitial Nitride coating from an application standpoint - used extensively to provide wear resistance and as a diffusion barrier and anti-reflection coating in semiconductor devices - wear resistant coatings on cemented carbides, either single or in combination with TiC, TiCN, and Al_2O_3 - coatings on tool steel for twist drills - diffusion barriers and anti-reflection coatings in integrated circuits

A.7 The CVD of ceramic materials: Oxides

Material	*Applications*
Aluminum Oxide	- coating for carbide tools (usually with TiC and TiN underlayers) - sealant coatings for plasma-sprayed oxides - thin films in the fabrication of transistors (FET) and other semiconductor applications
Chromium Oxide	- intermediate layer in corrosion- and erosion-resistant applications
Hafnium Oxide	- diffusion barrier in semiconductor devices (experimental) - oxidation-resistant coatings - wire coating for emitters
Silicon Dioxide	- passivation layers, surface dielectric, and doping barrier in semiconductor devices - intermetallic dielectrics - diffusion sources - etch barriers - oxidation protection of stainless steel in nuclear reactors - preparation of optical fibers - passivation layers in energy-saving architectural glass (E-glass) - barrier layers for SnO_2 films for glass coating
Tantalum Oxide	- high dielectric-constant capacitors - gate insulators in MOS devices - optical coatings, anti-reflection coatings, and coatings for hot mirrors
Tin Oxide	- energy saving coatings for plate glass (E-glass) and light bulbs - transparent electrodes in photovoltaic cells - transparent heating elements - antistatic coatings - coatings for solar cells - oxygen sensors for air/fuel control in combustion engines (Niobium oxide NbO_5 is also used for this application)
Titanium Oxide	- high index films in multilayer interference filters - antireflection coatings, optical waveguides and photoelectrochemical cells - dielectric layers in thin-film capacitors

Zirconium Oxide	- electrolytes, oxygen sensors, fuel cells, electronic conduction coatings, and furnace elements - piezoelectricity devices, PLZT ceramics - high-temperature passivation of microelectronic devices - structural composites
Iron Oxide	- beam splitter and interference layer in optical devices - detector for ethyl alcohol
Zinc Oxide	Applications in - piezoelectric devices - transducers - coatings for photoconductive devices, non-linear resistors (varistors), and overvoltage protectors
Titanates	- optoelectronic and piezoelectric devices (PZT-Lead Zirconate Titanate, and PLZT-Lead Lanthanum Zirconate Titanate) - potential in opto-electronic applications ($SrTiO_3$-Strontium Titanate)
Magnesia Aluminate (Spinel)	- potential application as an insulator coating or Silicon in semiconductor devices
Glasses	- passivation and planarization coating for Silicon wafers in semiconductor devices (PSG-PhosphoSilicate glass) - interlayer dielectric on polysilicon (BPSG-borophosphosilicate)

A.8 The CVD of ceramic materials: Borides, Silicides, III-V Compounds and II-VI Compounds (Chalcogenides)

Material	*Applications*
Borides	- limited industrial applications - boron filaments - experimental TiBr coatings for cemented carbide cutting tools and other wear- and erosion-resistant applications (pumps, valves, etc.) - ZrB_2 coatings for solar absorption - TiB_2 coatings for electrodes for Aluminum production (Hall-cell cathodes). TiB_2 has high resistance to molten Aluminum, yet it is readily wetted by the molten metal and good electrical contact is assured - production of TiB_2 powder for hot pressing
Molybdenum Disilicide	- conductive coatings in semiconductor devices - oxidation-resistant coatings - heating elements for high-temperature furnaces in oxidizing atmosphere
Tantalum Disilicide	- gate material in VLSI technology
Titanium Disilicide	- Schottky barriers and ohmic contacts in integrated circuits (IC's) - replacement of dopped Silicon in MOS devices where Silicon resistivity (300μohm-cm) is too high - general metallization

Tungsten Disilicide	- replacement for polysilicon gates in interconnects in MOS devices - polycide structures ($WSiO_2$ + polysilicon) - adhesion layer with non-selective Tungsten
III-V Compounds	- microwave devices - photo-chemical cells - light emitting diodes (LED) - solid state neutron detector of Boron phosphide, which is a refractory semiconductor with a wide band gap - field effect transistors (FET) of epitaxial InP (Indium phosphide) - heterostructure bipolar transistors (HBT) of InGaAs and InAlAs - BP whiskers
II-VI Compounds (Chalcogenides)	- infrared transparent windows (ZnS, ZnSe, and ZnTe) - photoconductors (CdSe and CdS) - photovoltaic devices (CdTe) - windows for CO_2 lasers - thin film photovoltaic devices (CdTe is a direct bandgap semiconductor with a bandgap energy of 1.5eV at room temperature)

Appendix B

Fluent simulations

B.1 Steady flow simulations for velocity field uniformity

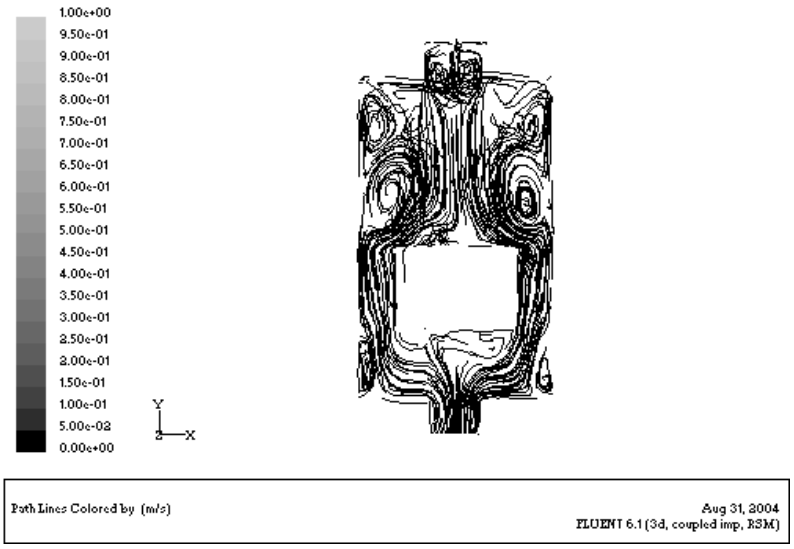

Figure B.1 Velocity path lines in a 200 mm height reactor, 74 mm diameter heater, for an inlet velocity v_S =1 m/s, and a steady flow pressure of 35 Pa

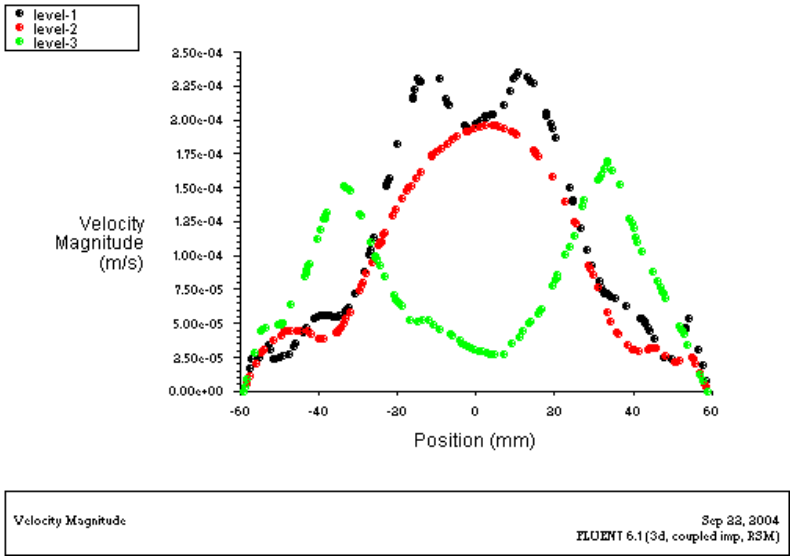

Figure B.2 Axial velocity values in a 200 mm height reactor, 74 mm diameter heater, for an inlet velocity v_S =1 m/s, and steady flow pressure of 35 Pa, at 105 mm, 140 mm, and 175 mm from the reactor base

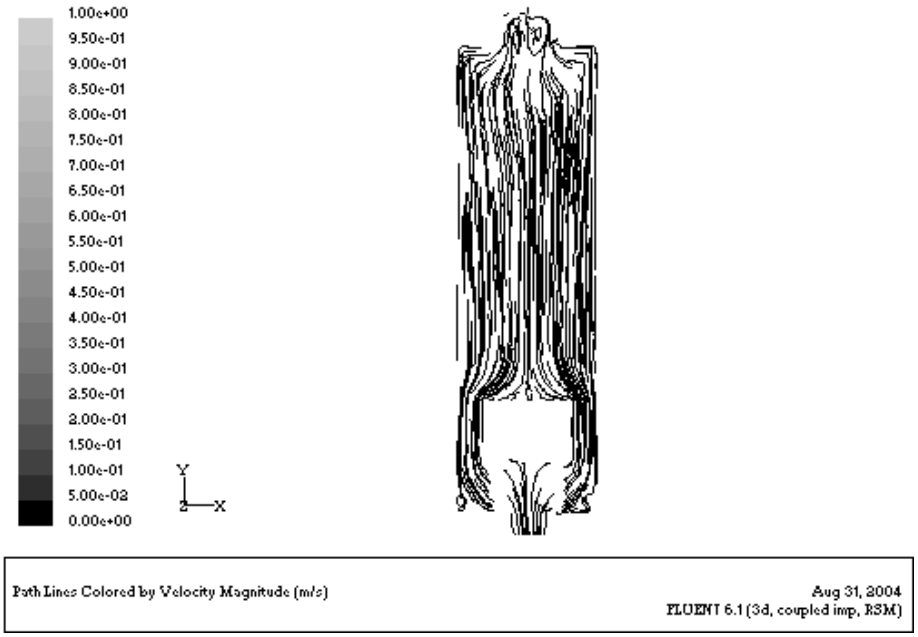

Figure B.3 Velocity path lines in a 400 mm height reactor, 74 mm diameter heater, for an inlet velocity v_S =1 m/s, and a steady flow pressure of 35 Pa

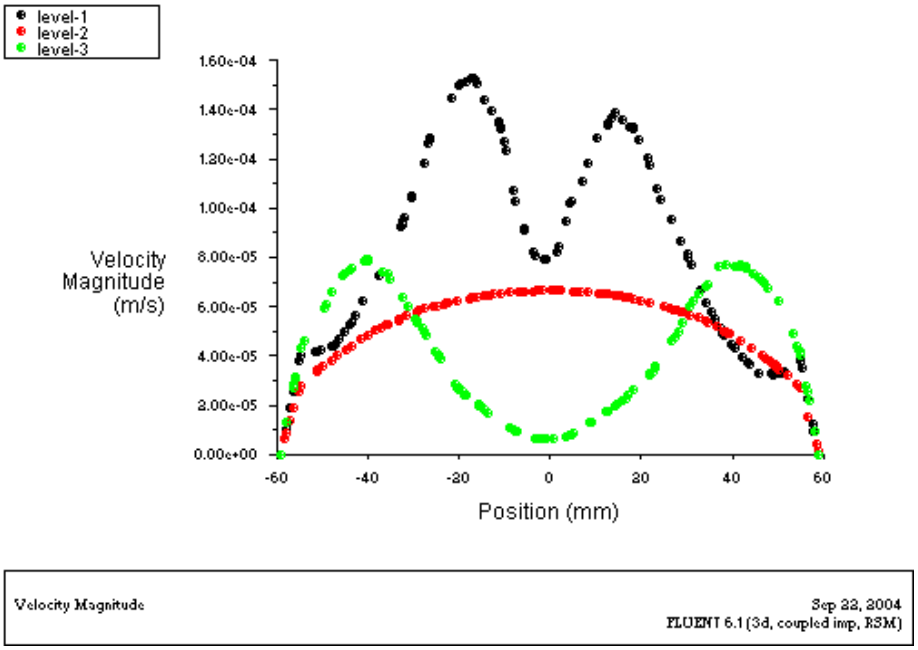

Figure B.4 Axial velocity values in a 400 mm height reactor, 74 mm diameter heater, for an inlet velocity v_S =1 m/s, and steady flow pressure of 35 Pa, at 105 mm, 240 mm, and 375 mm from the reactor base

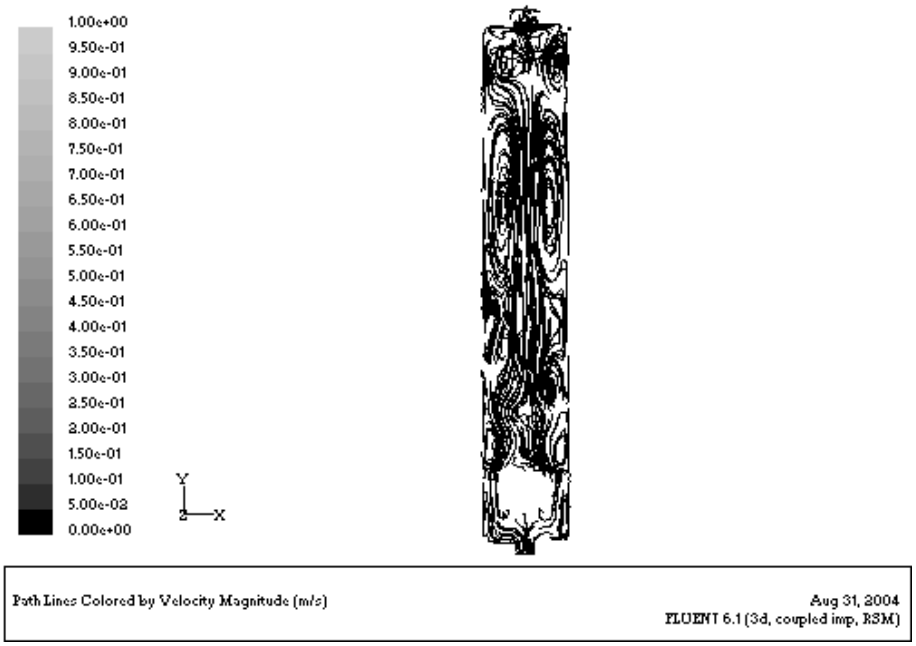

Figure B.5 Velocity path lines in a 700 mm height reactor, 74 mm diameter heater, for an inlet velocity v_S =1 m/s, and a steady flow pressure of 35 Pa

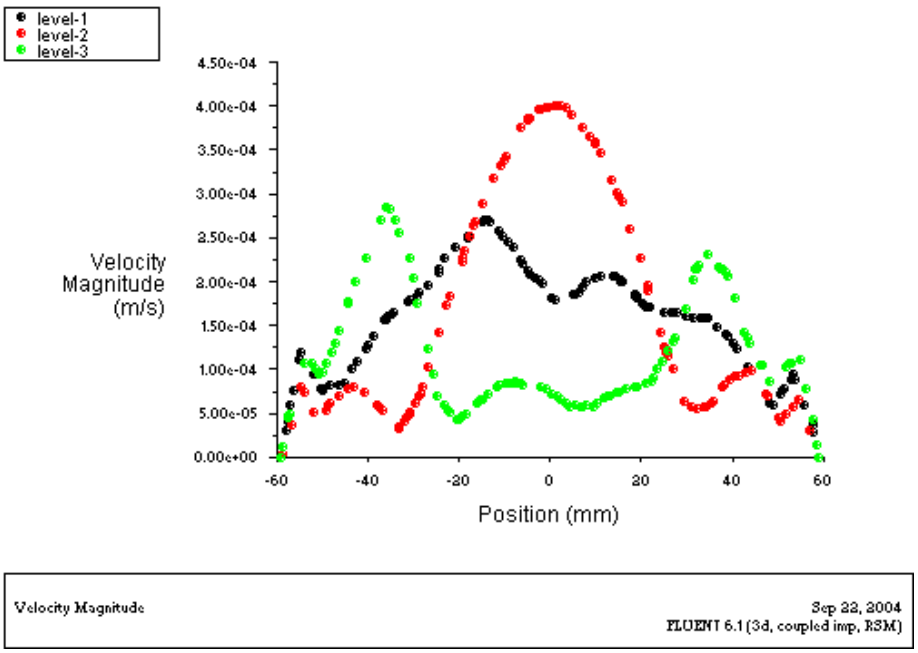

Figure B.6 Axial velocity values in a 700 mm height reactor, 74 mm diameter heater, for an inlet velocity v_S =1 m/s, and steady flow pressure of 35 Pa, at 105 mm, 390 mm, and 675 mm from the reactor base

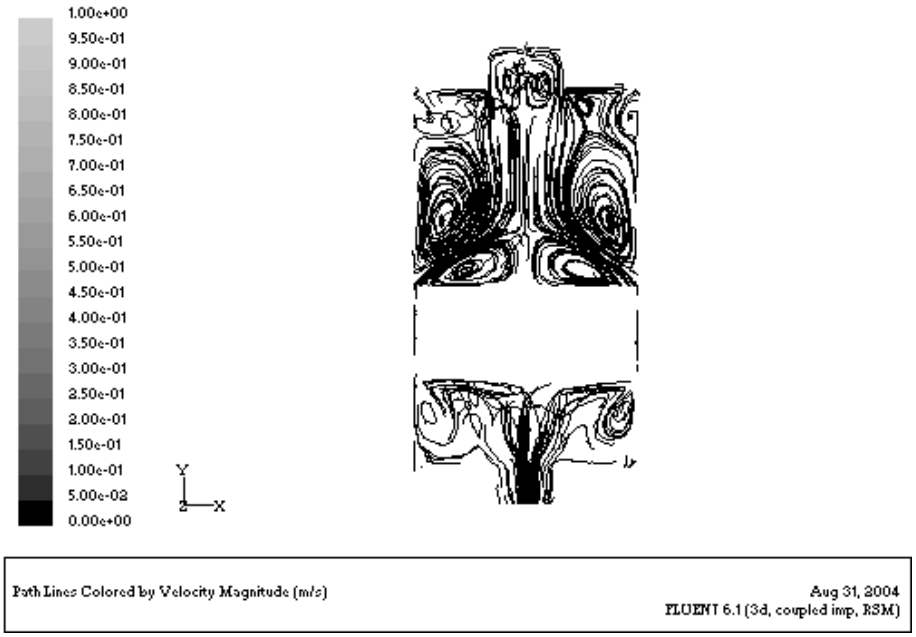

Figure B.7 Velocity path lines in a 200 mm height reactor, 116 mm diameter heater, for an inlet velocity v_S =1 m/s, and a steady flow pressure of 35 Pa

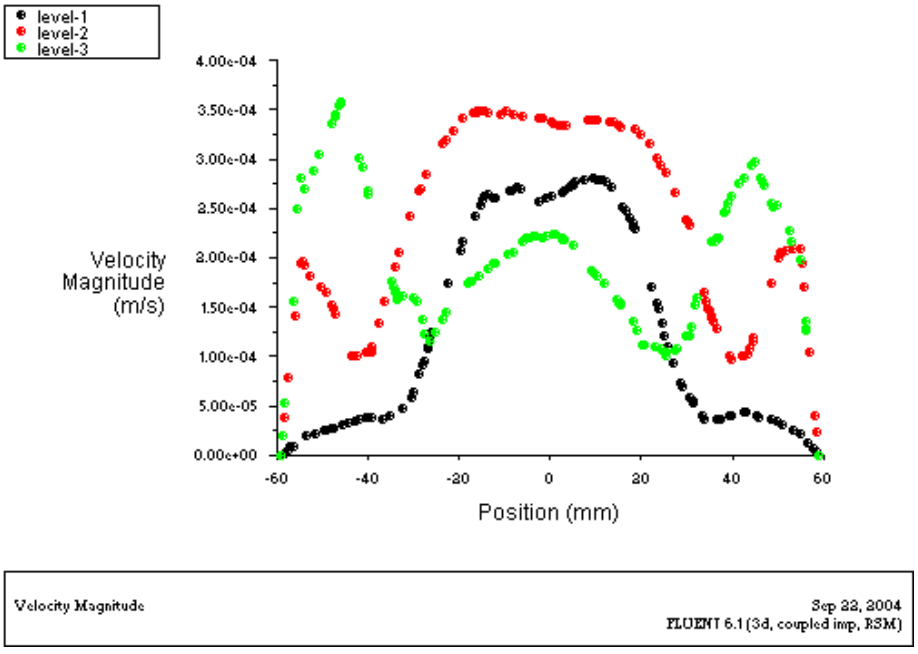

Figure B.8 Axial velocity values in a 200 mm height reactor, 116 mm diameter heater, for an inlet velocity v_S =1 m/s, and steady flow pressure of 35 Pa, at 105 mm, 140 mm, and 175 mm from the reactor base

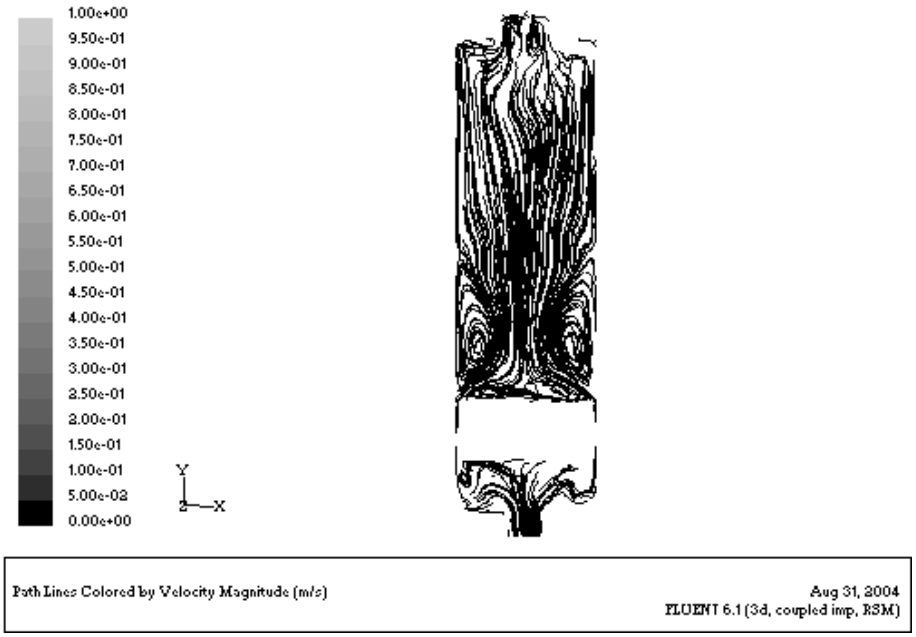

Figure B.9 Velocity path lines in a 400 mm height reactor, 116 mm diameter heater, for an inlet velocity v_S =1 m/s, and a steady flow pressure of 35 Pa

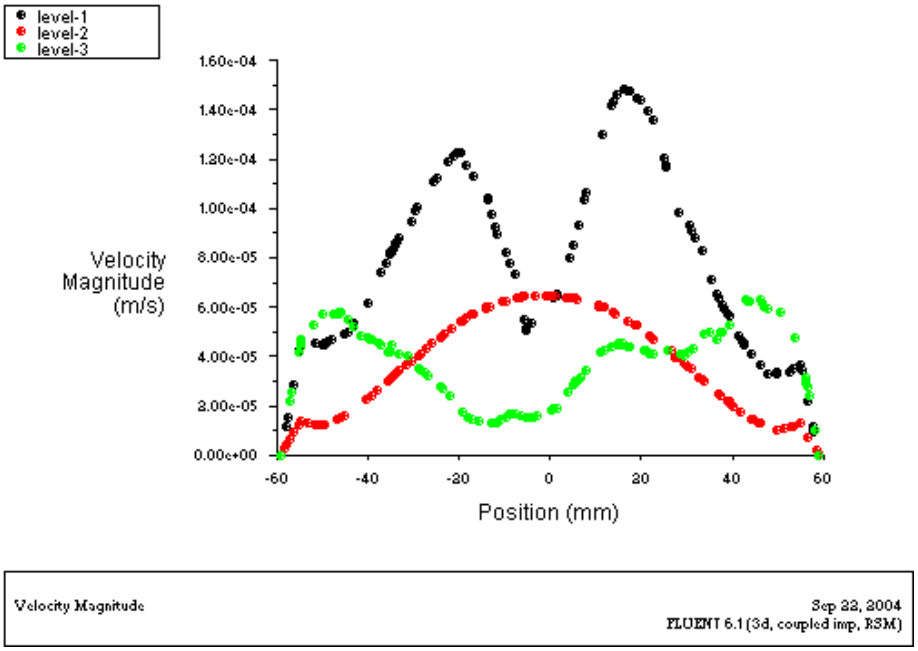

Figure B.10 Axial velocity values in a 400 mm height reactor, 116 mm diameter heater, for an inlet velocity v_S =1 m/s, and steady flow pressure of 35 Pa, at 105 mm, 240 mm, and 375 mm from the reactor base

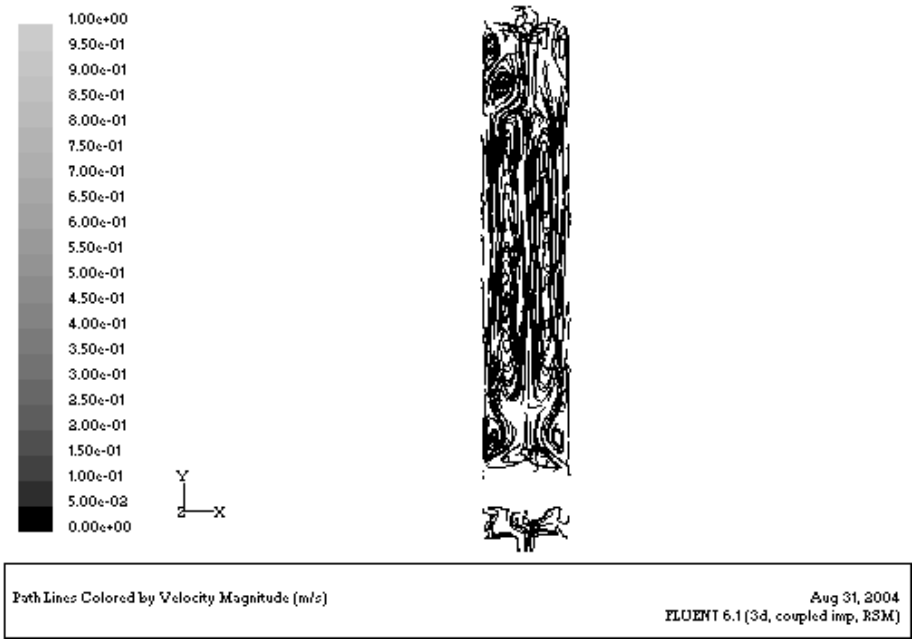

Figure B.11 Velocity path lines in a 700 mm height reactor, 116 mm diameter heater, for an inlet velocity v_S =1 m/s, and a steady flow pressure of 35 Pa

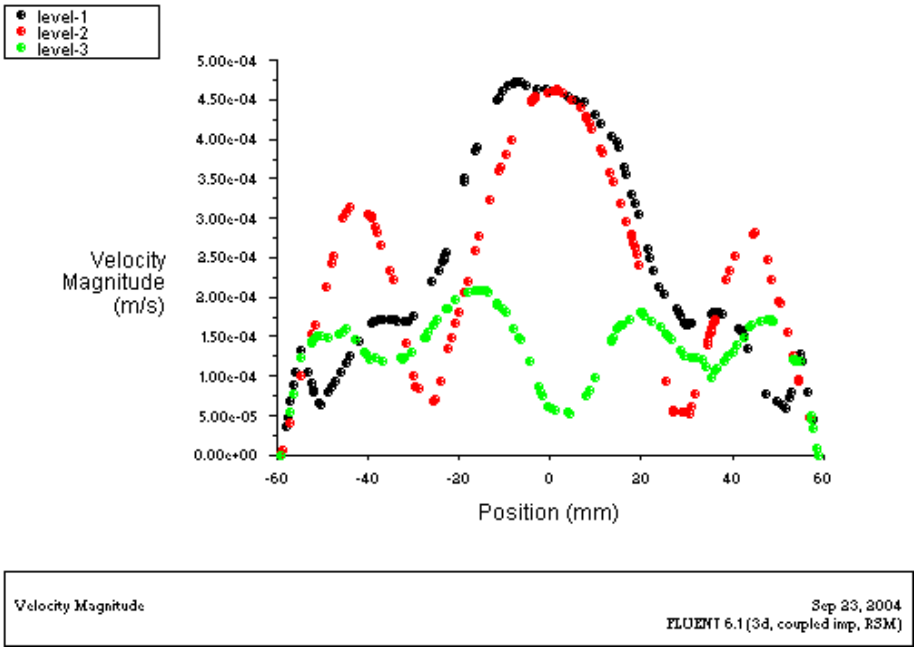

Figure B.12 Axial velocity values in a 700 mm height reactor, 116 mm diameter heater, for an inlet velocity v_S =1 m/s, and steady flow pressure of 35 Pa, at 105 mm, 390 mm, and 675 mm from the reactor base

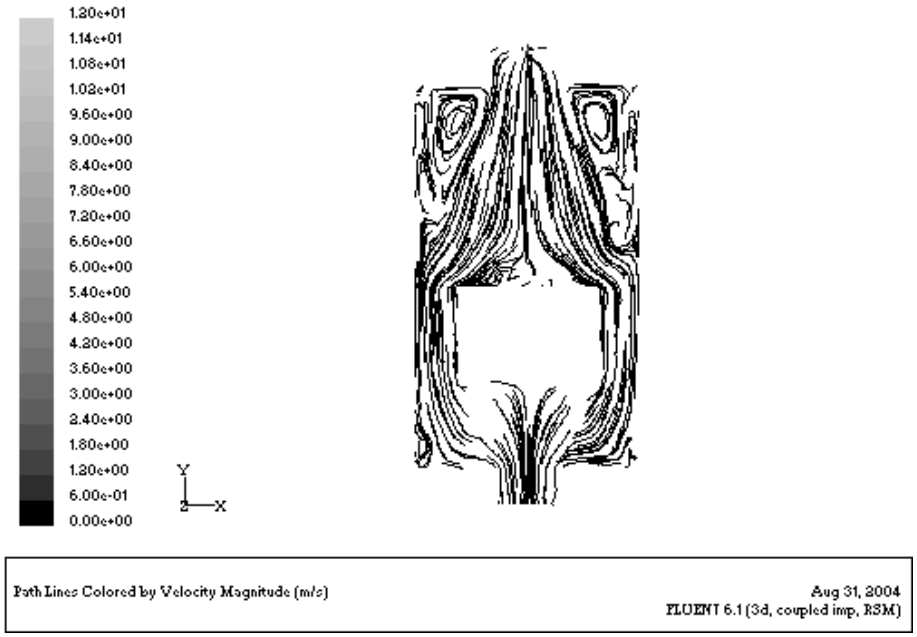

Figure B.13 Velocity path lines in a 200 mm height reactor, 74 mm diameter heater, for an inlet velocity v_S =12 m/s, and a steady flow pressure of 350 Pa

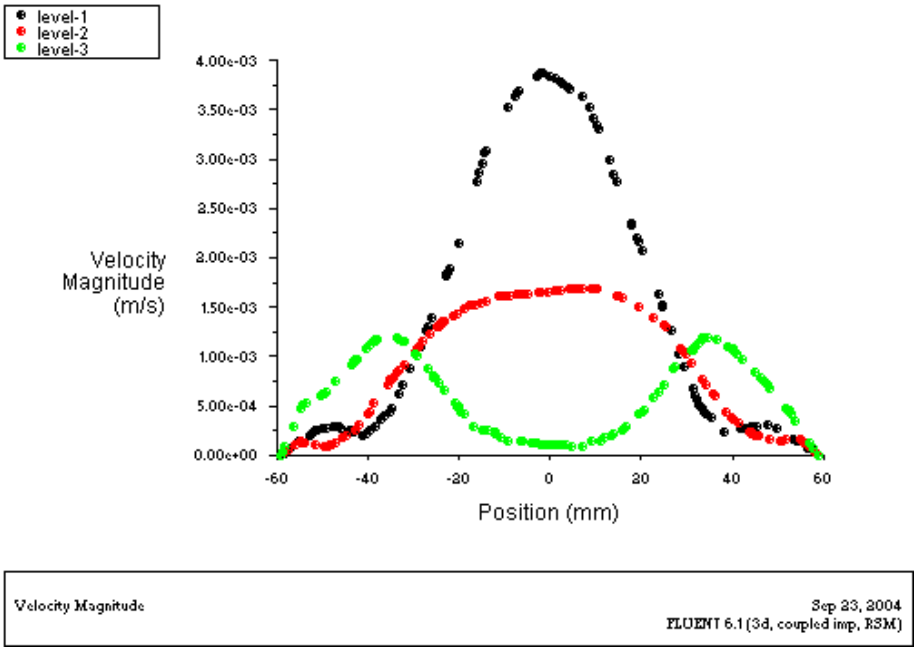

Figure B.14 Axial velocity values in a 200 mm height reactor, 74 mm diameter heater, for an inlet velocity v_S =12 m/s, and steady flow pressure of 350 Pa, at 105 mm, 140 mm, and 175 mm from the reactor base

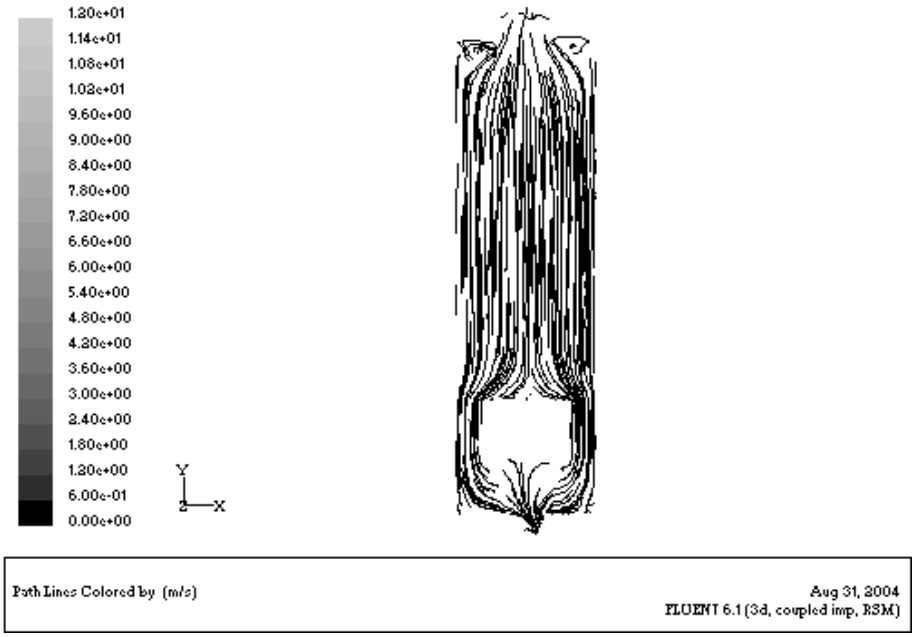

Figure B.15 Velocity path lines in a 400 mm height reactor, 74 mm diameter heater, for an inlet velocity v_S =12 m/s, and a steady flow pressure of 350 Pa

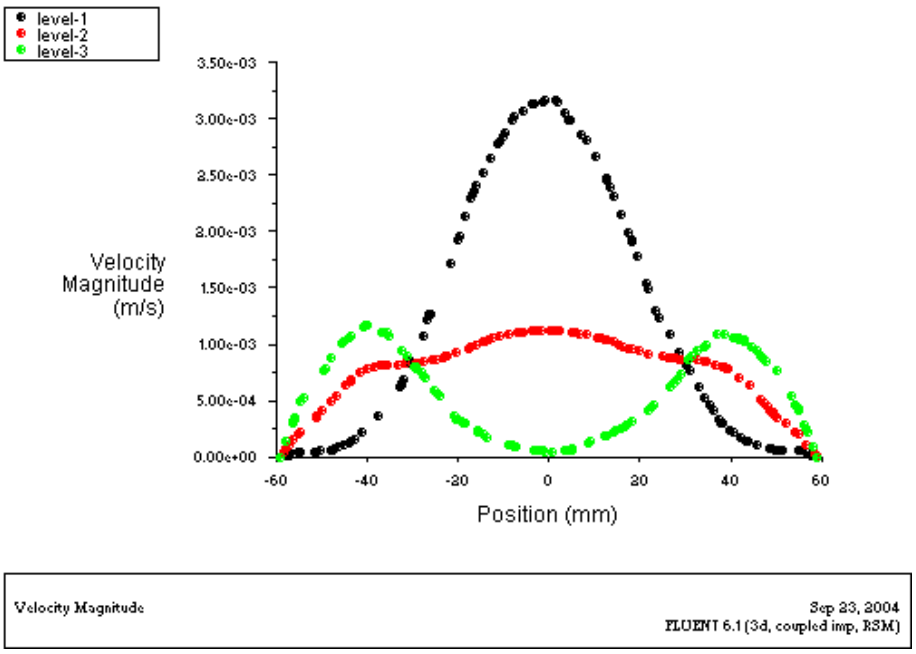

Figure B.16 Axial velocity values in a 400 mm height reactor, 74 mm diameter heater, for an inlet velocity v_S =12 m/s, and steady flow pressure of 350 Pa, at 105 mm, 240 mm, and 375 mm from the reactor base

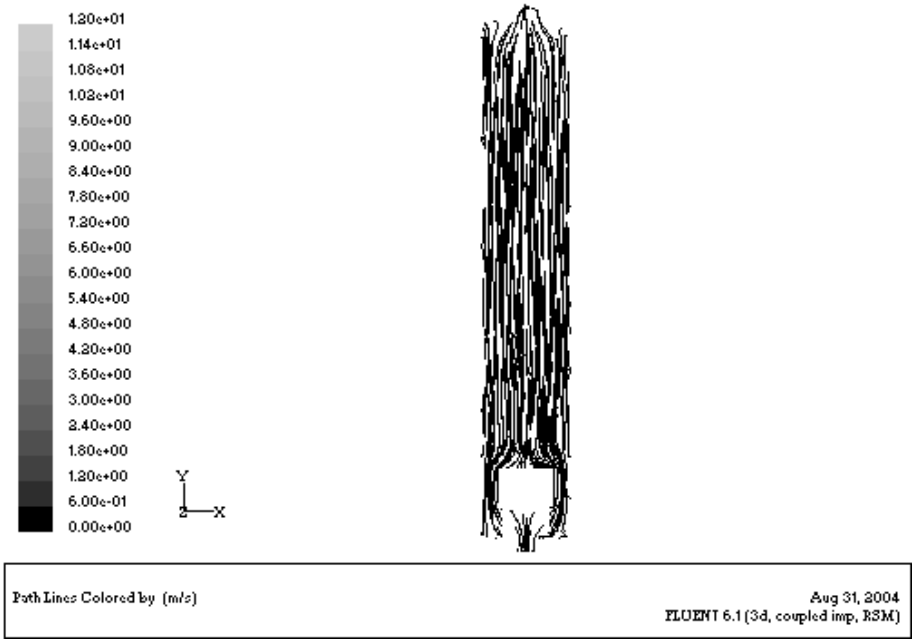

Figure B.17 Velocity path lines in a 700 mm height reactor, 74 mm diameter heater, for an inlet velocity v_S =12 m/s, and a steady flow pressure of 350 Pa

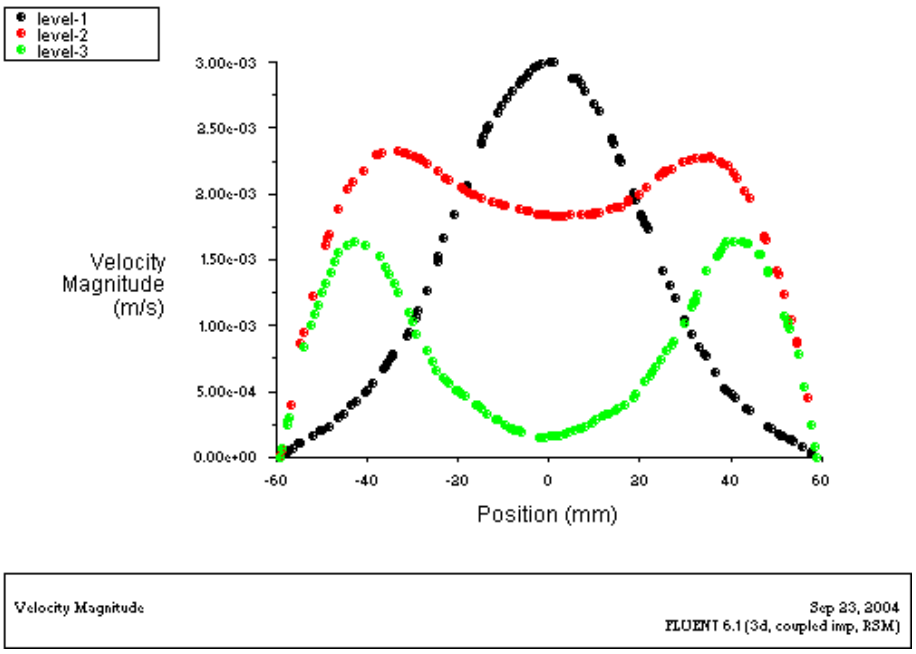

Figure B.18 Axial velocity values in a 700 mm height reactor, 74 mm diameter heater, for an inlet velocity v_S =12 m/s, and steady flow pressure of 350 Pa, at 105 mm, 390 mm, and 675 mm from the reactor base

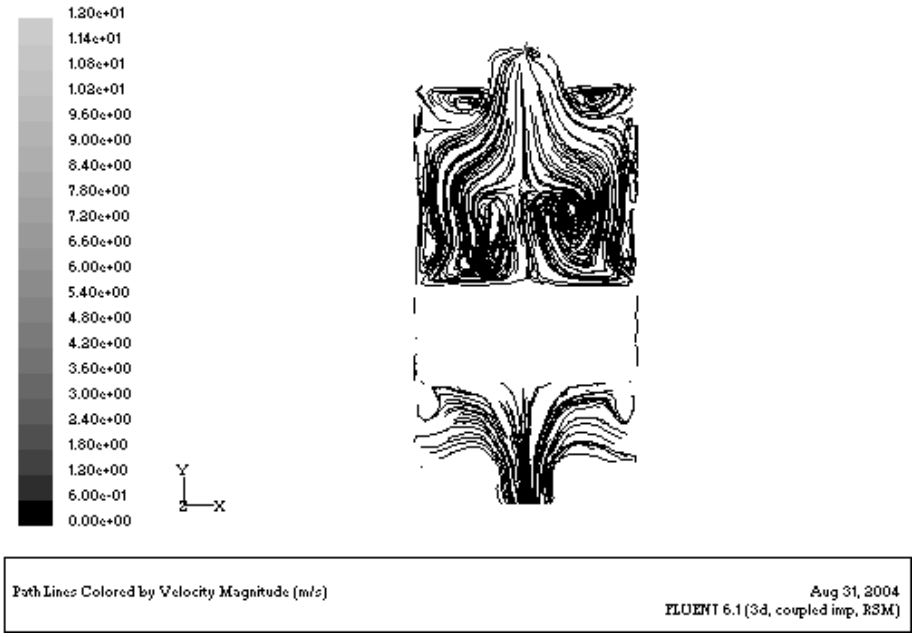

Figure B.19 Velocity path lines in a 200 mm height reactor, 116 mm diameter heater, for an inlet velocity v_S =12 m/s, and a steady flow pressure of 350 Pa

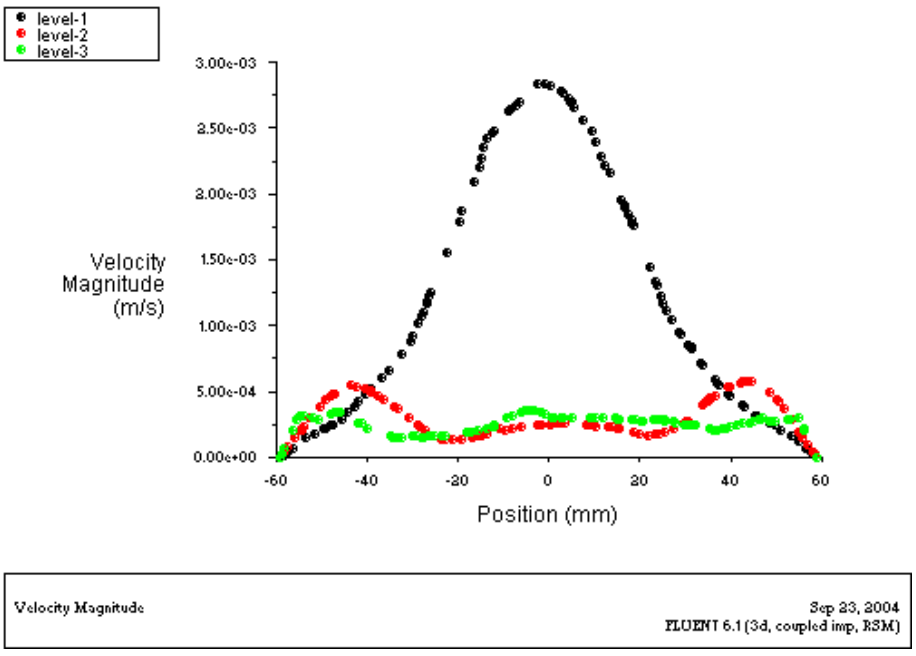

Figure B.20 Axial velocity values in a 200 mm height reactor, 116 mm diameter heater, for an inlet velocity v_S =12 m/s, and steady flow pressure of 350 Pa, at 105 mm, 140 mm, and 175 mm from the reactor base

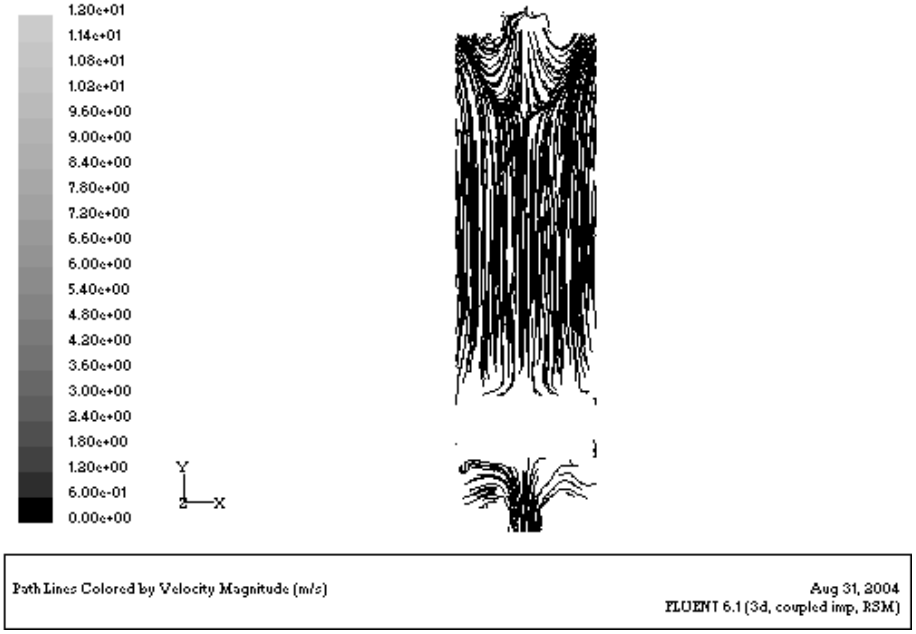

Figure B.21 Velocity path lines in a 400 mm height reactor, 116 mm diameter heater, for an inlet velocity v_S =12 m/s, and a steady flow pressure of 350 Pa

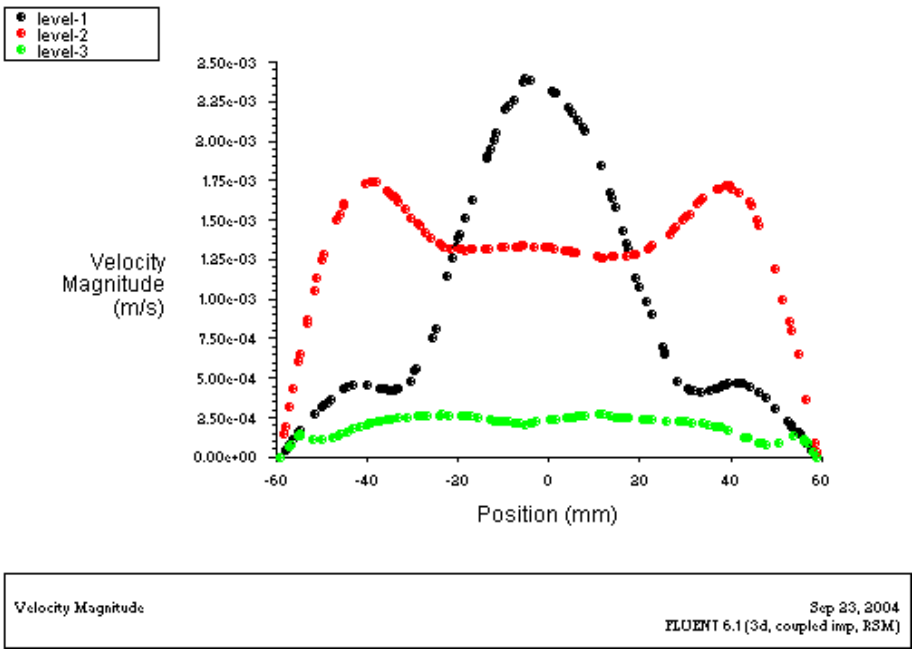

Figure B.22 Axial velocity values in a 400 mm height reactor, 116 mm diameter heater, for an inlet velocity v_S =12 m/s, and steady flow pressure of 350 Pa, at 105 mm, 240 mm, and 375 mm from the reactor base

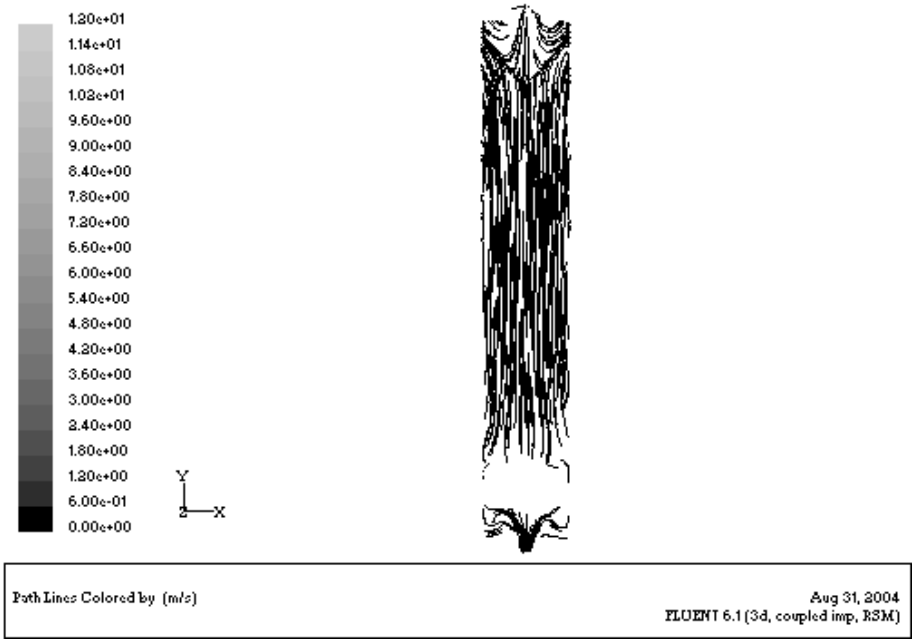

Figure B.23 Velocity path lines in a 700 mm height reactor, 116 mm diameter heater, for an inlet velocity v_S =12 m/s, and a steady flow pressure of 350 Pa

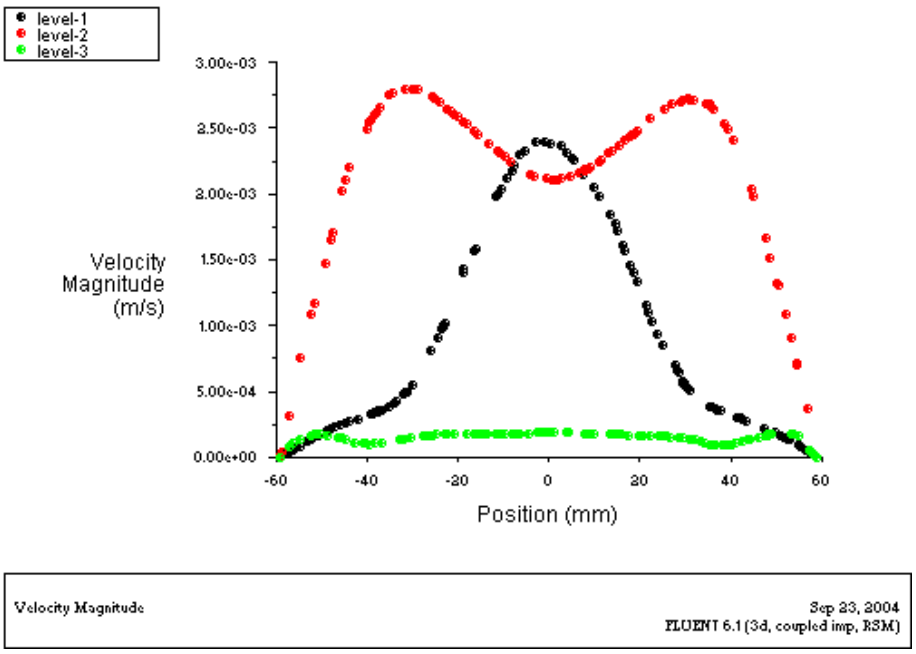

Figure B.24 Axial velocity values in a 700 mm height reactor, 116 mm diameter heater, for an inlet velocity v_S =12 m/s, and steady flow pressure of 350 Pa, at 105 mm, 390 mm, and 675 mm from the reactor base

B.2 Steady flow simulation for flow uniformity between stacked wafers

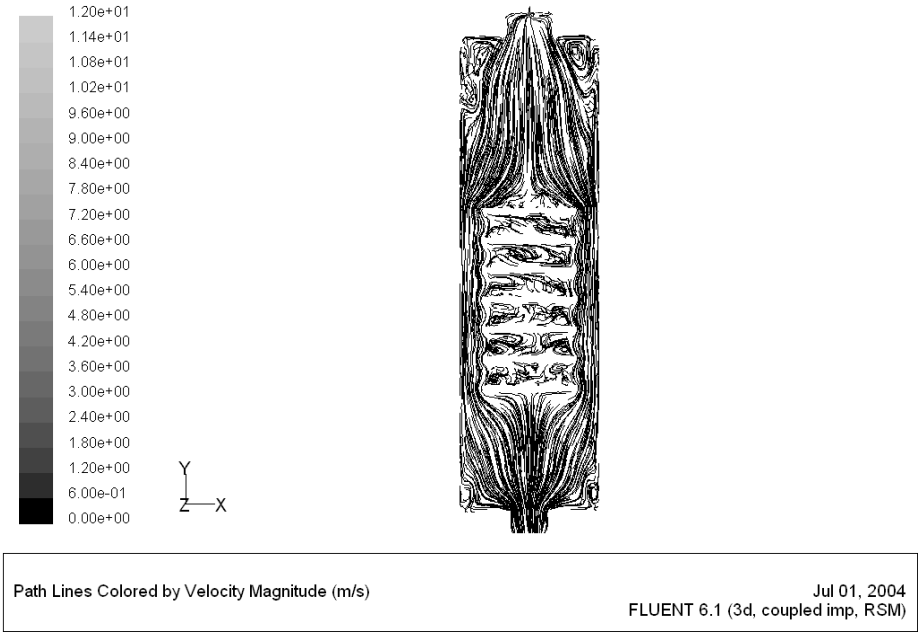

Figure B.25 Velocity path lines around the wafers for v_S = 12 m/s, and a steady flow pressure of 350 Pa

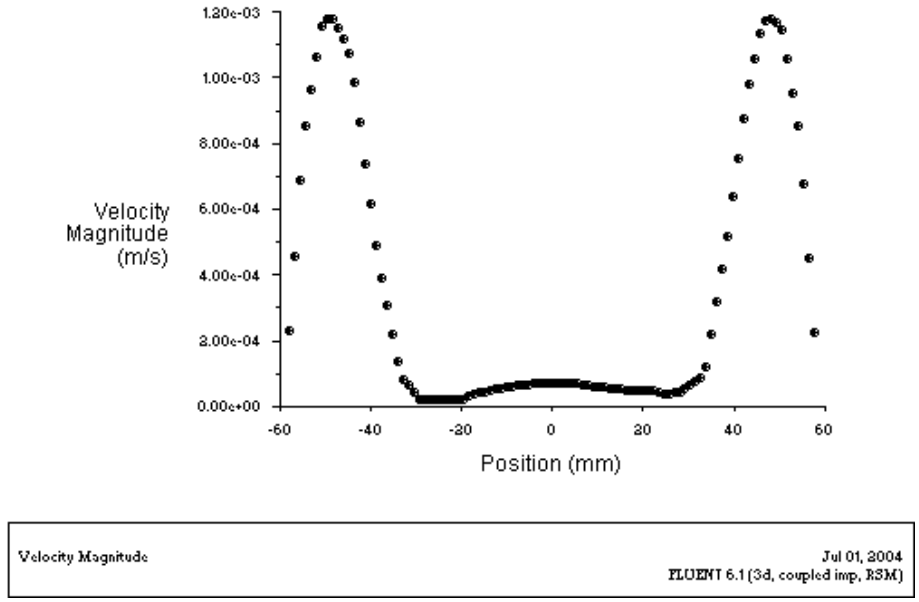

Figure B.26 Axial velocity values between the two top wafers (1 and 2), at the wafer number 2 substrate surface, for v_S = 12 m/s, and a steady flow pressure of 350 Pa

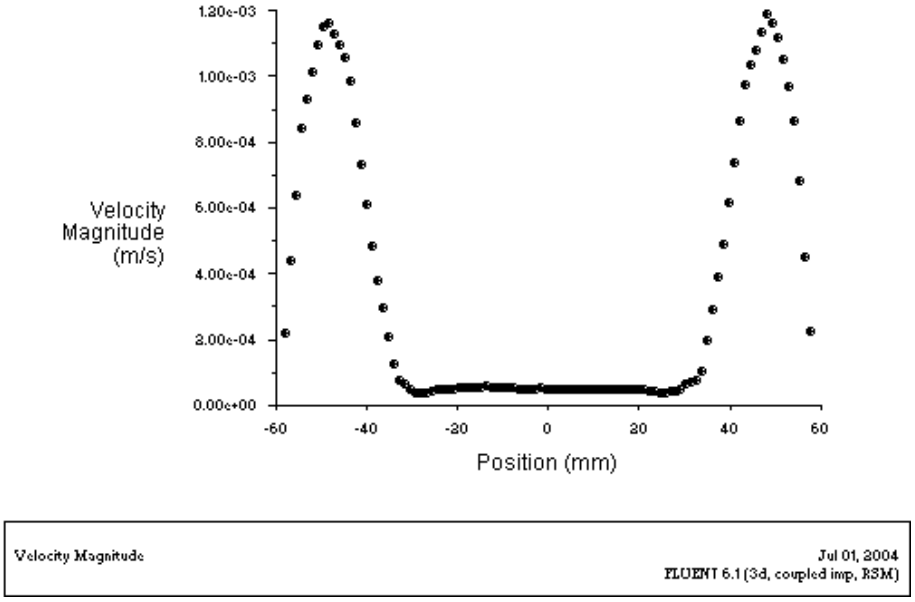

Figure B.27 Axial velocity values between wafers 2 and 3, at the wafer number 3 substrate surface, for v_S = 12 m/s, and a steady flow pressure of 350 Pa

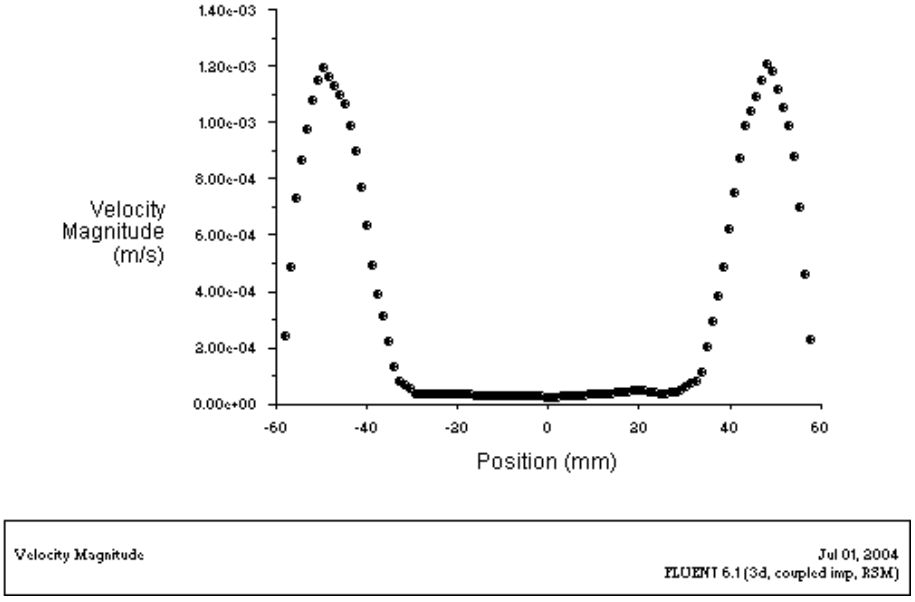

Figure B.28 Axial velocity values between wafers 3 and 4, at the wafer number 4 substrate surface, for v_S = 12 m/s, and a steady flow pressure of 350 Pa

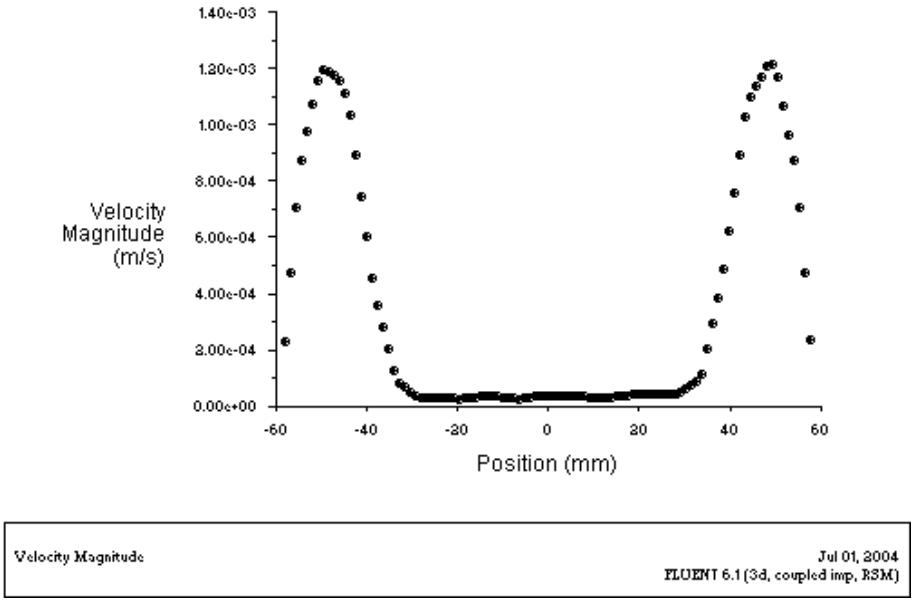

Figure B.29 Axial velocity values between wafers 4 and 5, at the wafer number 5 substrate surface, for v_S = 12 m/s, and a steady flow pressure of 350 Pa

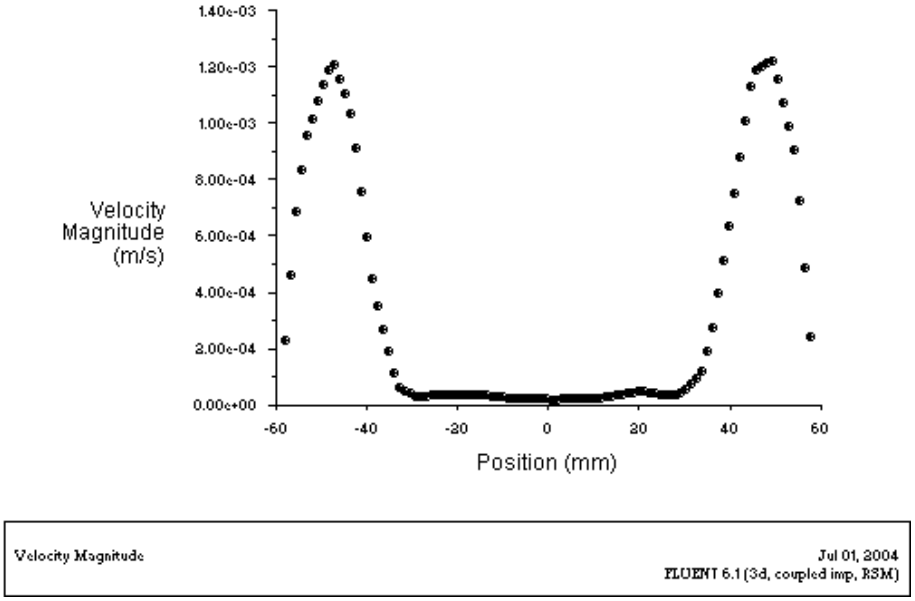

Figure B.30 Axial velocity values between wafers 5 and 6, at the wafer number 6 substrate surface, for v_S = 12 m/s, and a steady flow pressure of 350 Pa

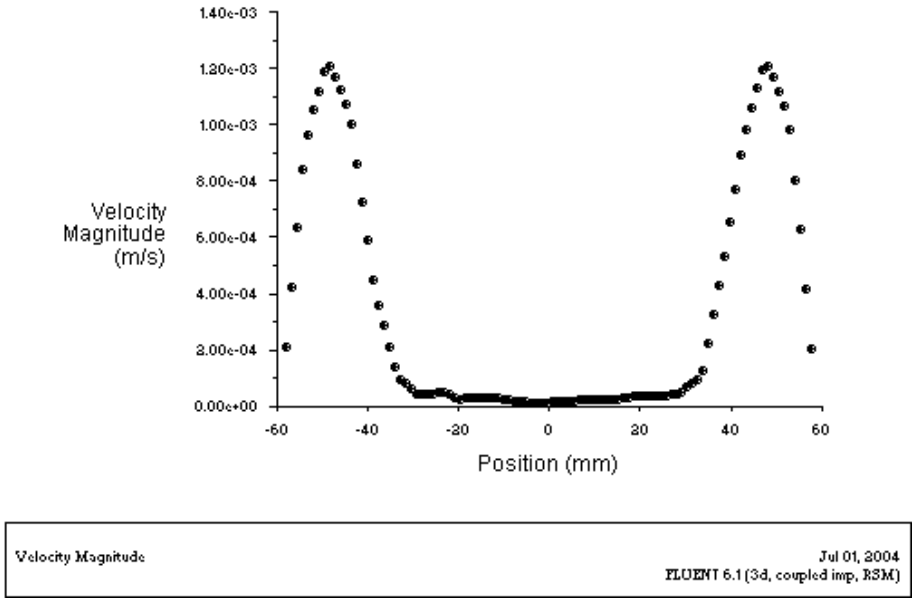

Figure B.31 Axial velocity values between wafers 6 and 7, at the wafer number 7 substrate surface, for v_S = 12 m/s, and a steady flow pressure of 350 Pa

Appendix C

Experimental graphs

Experimental data

Table C.1 Reactor volume flow field uniformity as a function of the pulse cycle length – subset 1 experimental data

t_i= 0.2 s		$P_{supply\ gage}$ = 300 kPa								
Pulse flow										
Experiment #	**01-02'**	**01-04'**	**01-06'**	**01-47**	**01-48**	**01-48'**	**01-49**	**01-49'**	**01-50**	**01-51**
tp [s]	20.00	15.00	10.00	7.50	5.00	3.75	2.50	1.75	1.25	0.75
tp/τ	4	3	2	1.5	1	0.75	0.5	0.35	0.25	0.15
tp/t_i	100	75	50	37.5	25	18.75	12.5	8.75	6.25	3.75
J_C^*	0.215	0.271	0.357	0.413	0.531	0.609	0.725	0.795	0.853	0.916
Uu	0.968	0.975	0.979	0.995	0.982	0.942	0.926	0.860	0.832	0.765
Uc	0.974	0.978	0.977	0.991	0.974	0.928	0.914	0.836	0.809	0.732
P_{max} *[Pa]*	88.6	89.9	93.8	95.1	105.2	120.7	138.3	175.0	210.1	306.4
P_{min} *[Pa]*	4.4	6.6	11.3	14.7	28.7	43.4	70.8	109.0	150.0	258.5
Steady flow										
Experiment #	**01-55**	**01-56**	**01-58**	**01-60**	**01-61**	**01-61'**	**01-62**	**01-62'**	**01-63**	**01-64**
$P_{eq.steady}$ *[Pa]*	19.1	24.3	33.4	39.3	55.9	73.5	100.3	139.2	179.3	280.8
Uu	0.839	0.808	0.848	0.842	0.866	0.867	0.845	0.810	0.805	0.673
Uc	0.819	0.777	0.831	0.817	0.843	0.849	0.818	0.770	0.762	0.611

Table C.2 Reactor volume flow field uniformity as a function of the pulse cycle length – subset 2 experimental data

t_i= 0.4 s			$P_{supply\ gage}$= 400 kPa							
Pulse flow										
Experiment #	**01-65**	**01-66**	**01-67**	**01-68**	**01-69**	**01-70**	**01-71**	**01- 72**	**01-73**	**01-74**
tp [s]	20.00	17.50	15.00	12.50	10.00	7.50	5.00	2.50	1.25	0.75
tp/τ	4	3.5	3	2.5	2	1.5	1	0.5	0.25	0.15
tp/t_i	50	43.75	37.5	31.25	25	18.75	12.5	6.25	3.125	1.875
J_C^*	0.199	0.227	0.255	0.292	0.354	0.426	0.540	0.717	0.866	0.944
Uu	0.975	0.974	0.971	0.970	0.967	0.937	0.917	0.824	0.751	0.758
Uc	0.976	0.975	0.968	0.966	0.960	0.929	0.899	0.793	0.708	0.715
P_{max} *[Pa]*	172.3	172.5	177.4	182.3	181.4	192.0	213.5	297.0	472.2	668.9
P_{min} *[Pa]*	4.6	5.7	7.8	10.7	16.6	27.0	49.0	142.8	350.0	596.5
Steady flow										
Experiment #	**01- 78**	**01-79**	**01-80**	**01-81**	**01-82**	**01-83**	**01-84**	**01-85**	**01-86**	**01-87**
$P_{eq.steady}$ *[Pa]*	34.3	39.2	45.3	53.2	64.3	81.8	115.3	212.8	409.1	631.4
Uu	0.792	0.834	0.852	0.858	0.864	0.858	0.837	0.742	0.639	0.486
Uc	0.762	0.811	0.834	0.838	0.843	0.838	0.815	0.706	0.587	0.408

Table C.3 Reactor volume flow field uniformity as a function of the pulse cycle length – subset 3 experimental data

t_i= 0.8 s		$P_{supply\ gage}$= 400 kPa								
Pulse flow										
Experiment #	**01-90**	**01-91**	**01-92**	**01-93**	**01-94**	**01-95**	**01-96**	**01-97**	**01-98**	**01-99**
tp [s]	20.0 0	15.00	10.00	7.50	5.00	3.75	2.50	1.75	1.25	1.00
tp/τ	4	3	2	1.5	1	0.75	0.5	0.35	0.25	0.2
tp/t_i	25	18.75	12.5	9.375	6.25	4.687 5	3.125	2.187 5	1.562 5	1.25
J_C^*	0.19 1	0.249	0.348	0.431	0.559	0.649	0.755	0.864	0.932	0.969
Uu	0.97 6	0.956	0.920	0.910	0.830	0.790	0.710	0.760	0.788	0.541
Uc	0.96 8	0.940	0.900	0.880	0.800	0.750	0.660	0.690	0.727	0.441
P_{max} *[Pa]*	308. 4	311.2	324.0	334.2	370.9	414.6	529.3	680.2	811.6	604.6
P_{min} *[Pa]*	5.9	10.5	25.0	43.2	92.3	152.6	282.8	495.0	695.0	564.0
Steady flow										
Experiment #	**01-61**	**01-83**	**01-84**	**01-63**	**01-85**	**01-64**	**01-86**	**01-100**	**01-101**	**01-100**
$P_{eq.steady}$ *[Pa]*	58.9	77.6	112.8	143.9	207.4	268.9	399.5	587.5	756.8	585.7
Uu	0.86 6	0.858	0.837	0.805	0.742	0.673	0.639	0.867	0.864	0.867
Uc	0.84 3	0.838	0.815	0.762	0.706	0.611	0.587	0.850	0.850	0.850

Table C.4 Reactor volume flow field uniformity as a function of the pulse cycle length – subset 4 experimental data

t_i= 1 s		$P_{supply\ gage}$= 400 kPa							
Pulse flow									
Experiment #	**01-102**	**01-103**	**01-104**	**01-105**	**01-106**	**01-107**	**01-108**	**01-109**	**01-110**
tp [s]	25.00	20.00	15.00	10.00	5.00	3.75	2.50	1.75	1.25
tp/τ	5	4	3	2	1	0.75	0.5	0.35	0.25
tp/t_i	25.00	20.00	15.00	10.00	5.00	3.75	2.50	1.75	1.25
J_C^*	0.160	0.200	0.260	0.353	0.574	0.671	0.796	0.891	0.963
Uu	0.967	0.963	0.939	0.905	0.797	0.751	0.717	0.757	0.546
Uc	0.964	0.954	0.920	0.882	0.756	0.701	0.656	0.701	0.464
P_{max} *[Pa]*	361.9	369.7	380.2	371.0	435.2	489.9	600.6	759.5	629.9
P_{min} *[Pa]*	5.1	7.7	13.8	27.0	115.0	192.0	358.0	586.0	576.0
Steady flow									
Experiment #	**01-61**	**01-61'**	**01-62**	**01-62'**	**01-64**	**01-111**	**01-112**	**01-87**	**01-113**
$P_{eq.steady}$ *[Pa]*	57.9	74.1	98.7	131.0	249.8	328.6	477.9	676.6	606.7
Uu	0.866	0.867	0.845	0.810	0.673			0.486	
Uc	0.843	0.849	0.818	0.770	0.611			0.408	

Table C.5 Reactor volume flow field uniformity as a function of the pulse cycle maximum pressure experimental data

t_i = 0.5 s; τ = 6.6 s; $t_p = 4\tau$ = 26.4 s								
Pulse flow								
Experiment #	**02-207**	**02-206**	**02-205**	**02-204**	**02-203**	**02-202**	**02-201**	**02-200**
Jc*	0.114	0.113	0.111	0.107	0.109	0.109	0.109	0.107
Uu	0.903	0.894	0.887	0.878	0.866	0.862	0.837	0.832
Uc	0.888	0.874	0.860	0.836	0.835	0.827	0.787	0.784
P_{max} [Pa]	4112.2	5520.7	7158.7	9063.7	9990.3	11587.4	13243.1	13709.2
P_{min} [Pa]	10.1	10.5	10.7	10.8	11.0	11.5	12.1	12.2
Steady flow								
Experiment #	**02-210**	**02-211**	**02-212**	**02-213**	**02-214**	**02-215**	**02-216**	**02-217**
$P_{eq.steady}$ [Pa]	467	623	793	974	1090	1265	1445	1470
Uu	0.498	0.441	0.479	0.491	0.473	0.450	0.491	0.478
Uc	0.409	0.355	0.396	0.417	0.397	0.365	0.411	0.391

Table C.6 Stacked wafer experimental data

t_i = 0.5 s; τ = 6.6 s; t_p = 26.4 s								
Pulse flow								
Experiment #	**03-307**	**03-306**	**03-305**	**03-304**	**03-303**	**03-302**	**03-301**	**03-300**
Jc*	0.112	0.110	0.110	0.105	0.108	0.108	0.108	0.103
Uu	0.905	0.902	0.914	0.900	0.882	0.884	0.883	0.879
Uc	0.903	0.891	0.915	0.896	0.872	0.874	0.871	0.865
P_{max} [Pa]	3935.3	5390.0	6882.8	8869.1	9397.7	10872.8	12380.0	14766.5
P_{min} [Pa]	10.5	10.8	11.1	10.8	12.0	12.3	12.3	12.0
Steady flow								
Experiment #	**03-310**	**03-311**	**03-312**	**03-313**	**03-314**	**03-315**	**03-316**	**03-317**
$P_{eq.steady}$ [Pa]	440.0	593.5	757.5	933.2	1017.7	1173.5	1338.7	1522.1
Uu	0.915	0.904	0.910	0.895	0.893	0.891	0.888	0.875
Uc	0.884	0.862	0.873	0.844	0.842	0.841	0.834	0.826

C.1 Reactor volume flow field uniformity as a function of the pulse cycle length

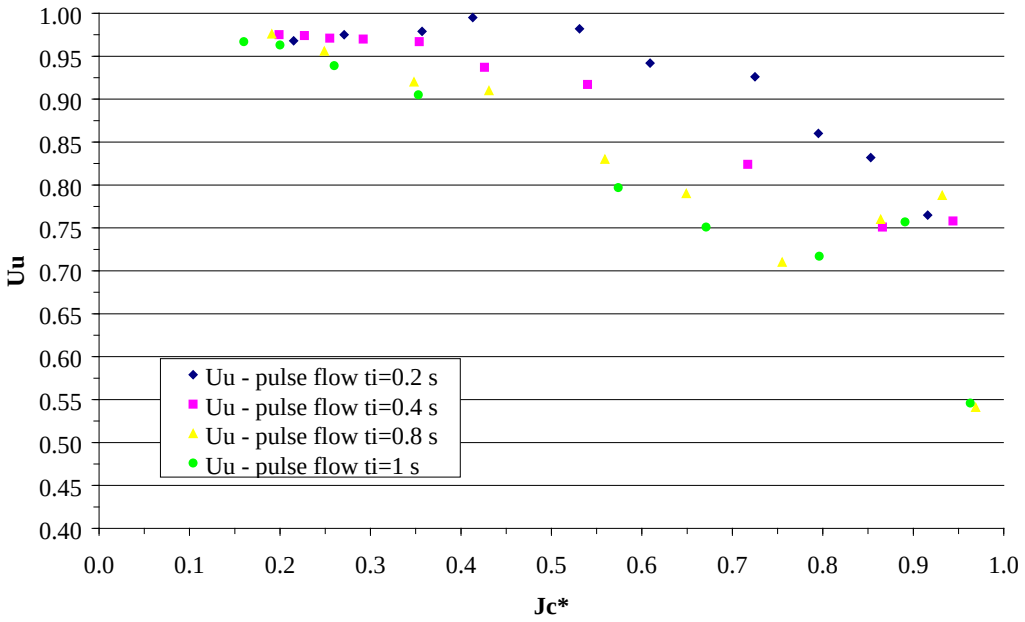

Figure C.1 Uncompensated sublimation uniformity Uu comparison between pulse flow experiments at injection times of 0.2 s, 0.4 s, 0.8 s, and 1 s, at cycle times of 5τ down to 0.15τ

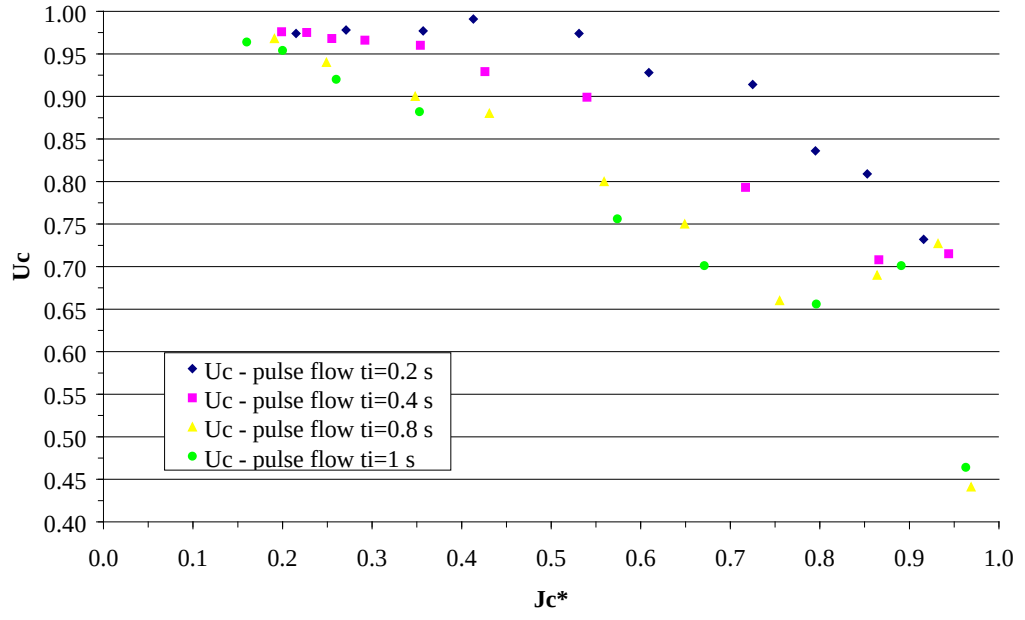

Figure C.2 Compensated sublimation uniformity Uc comparison between pulse flow experiments at injection times of 0.2 s, 0.4 s, 0.8 s, and 1 s, at cycle times of 5τ down to 0.15τ

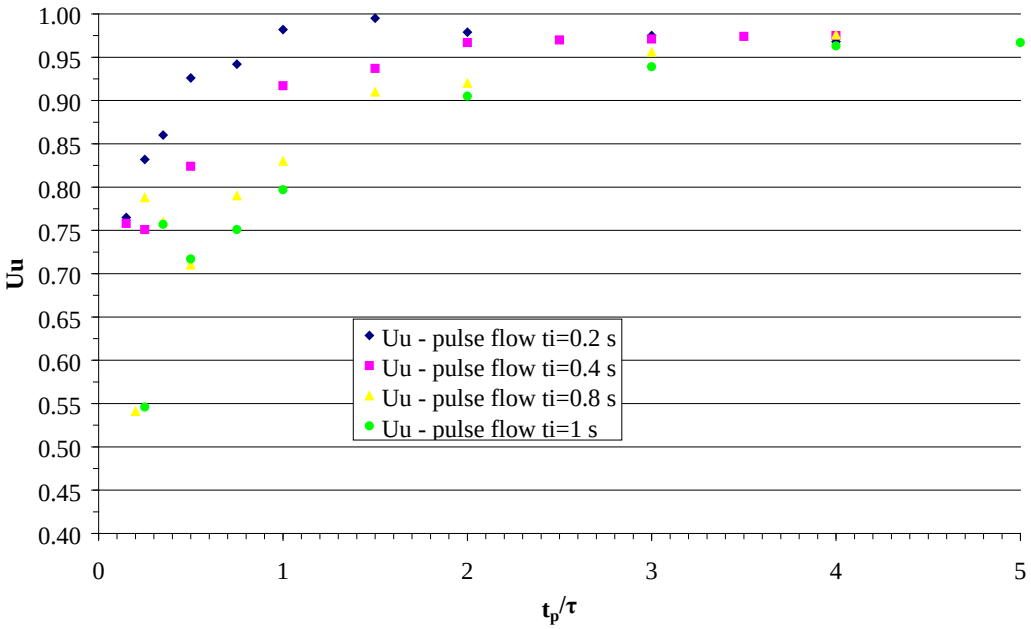

Figure C.3 Uncompensated sublimation uniformity Uu comparison between pulse flow experiments at injection times of 0.2 s, 0.4 s, 0.8 s, and 1 s, at cycle times of 5τ down to 0.15τ as a function of cycle length

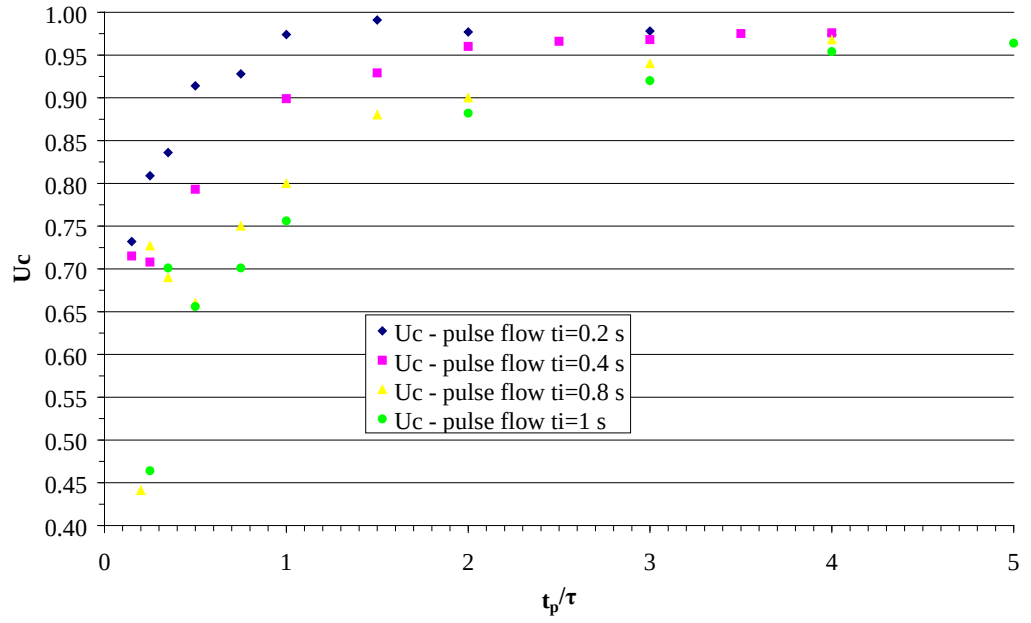

Figure C.4 Compensated sublimation uniformity Uc comparison between pulse flow experiments at injection times of 0.2 s, 0.4 s, 0.8 s, and 1 s, at cycle times of 5τ down to 0.15τ as a function of cycle length

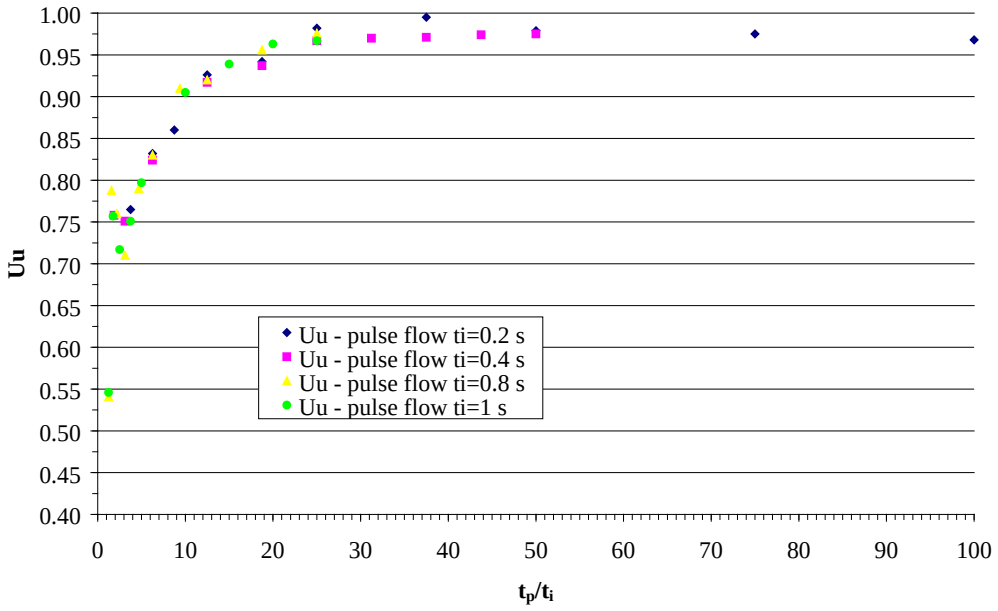

Figure C.5 Uncompensated sublimation uniformity comparison between pulse flow experiments at injection times of 0.2 s, 0.4 s, 0.8 s, and 1 s, at cycle times of 5τ down to 0.15τ function of the ratio between the cycle time and the injection time

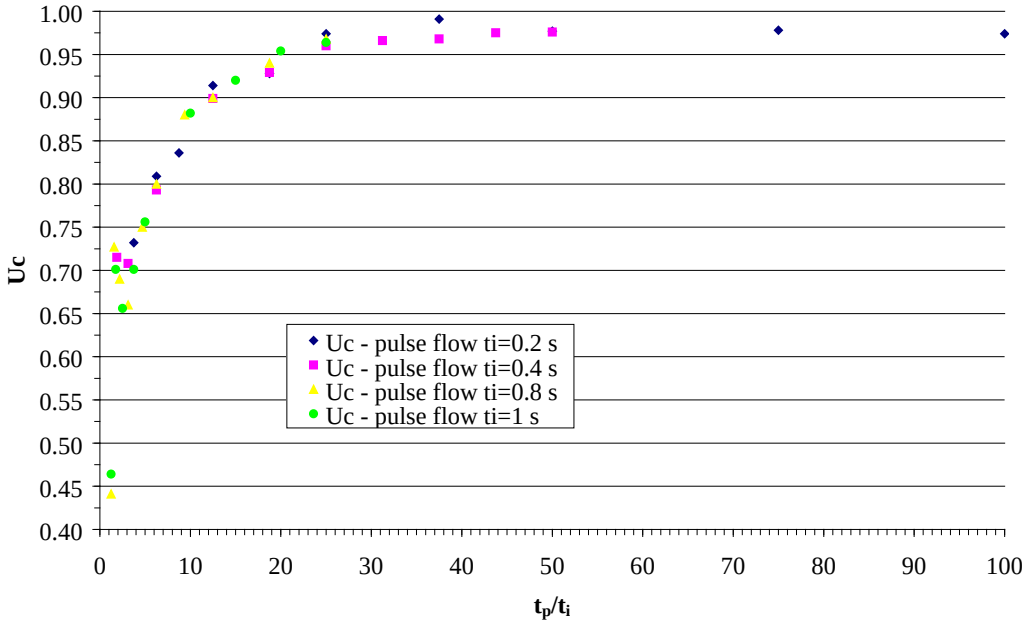

Figure C.6 Compensated sublimation uniformity comparison between pulse flow experiments at injection times of 0.2 s, 0.4 s, 0.8 s, and 1 s, at cycle times of 5τ down to 0.15τ function of the ratio between the cycle time and the injection time

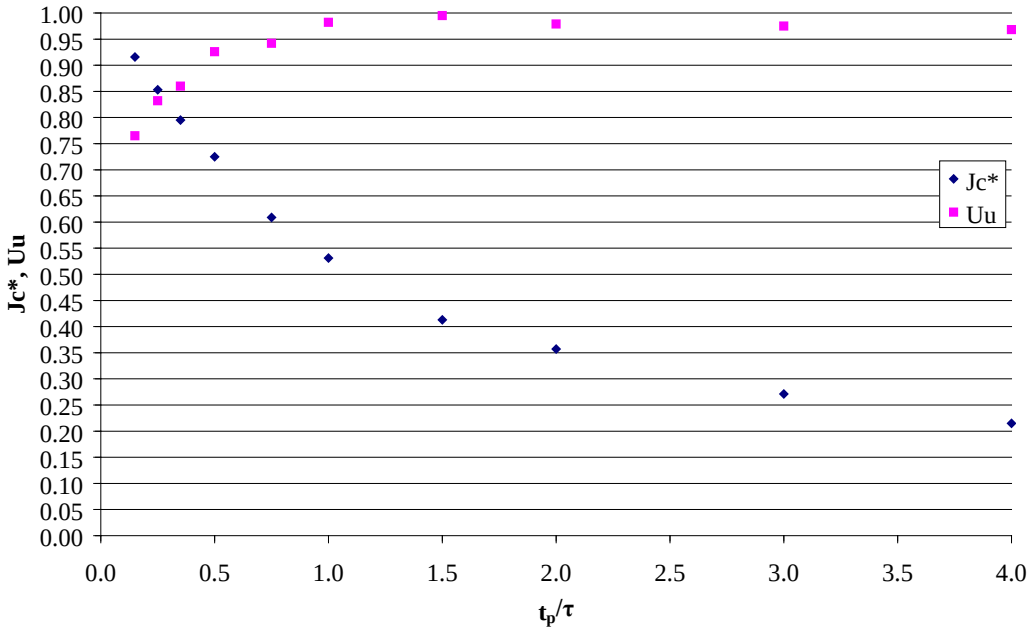

Figure C.7 The non-dimensional molecular flux J_C* and the uncompensated sublimation uniformity Uu, versus t_p/τ, for an injection time t_i = 0.2 s pulse flow experiments

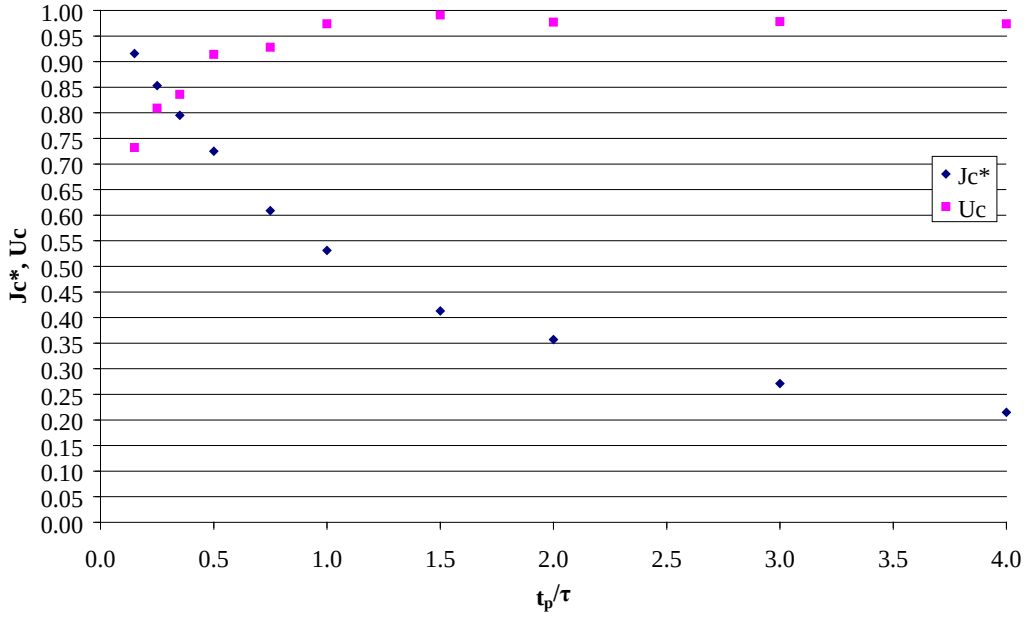

Figure C.8 The non-dimensional molecular flux J_C* and the compensated sublimation uniformity Uc, versus t_p/τ, for an injection time t_i = 0.2 s pulse flow experiments

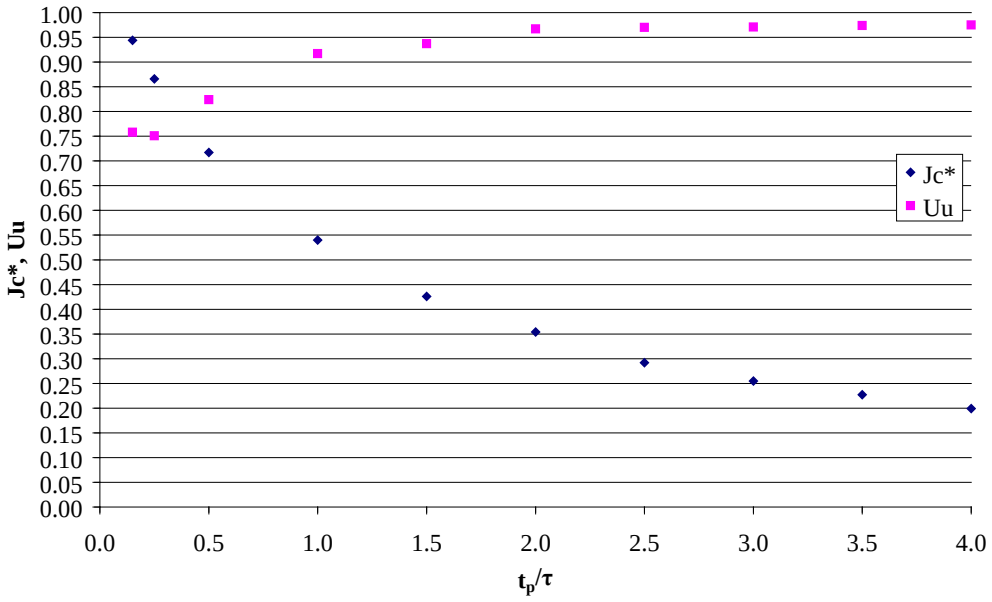

Figure C.9 The non-dimensional molecular flux J_C* and the uncompensated sublimation uniformity Uu, versus t_p/τ, for an injection time t_i = 0.4 s pulse flow experiments

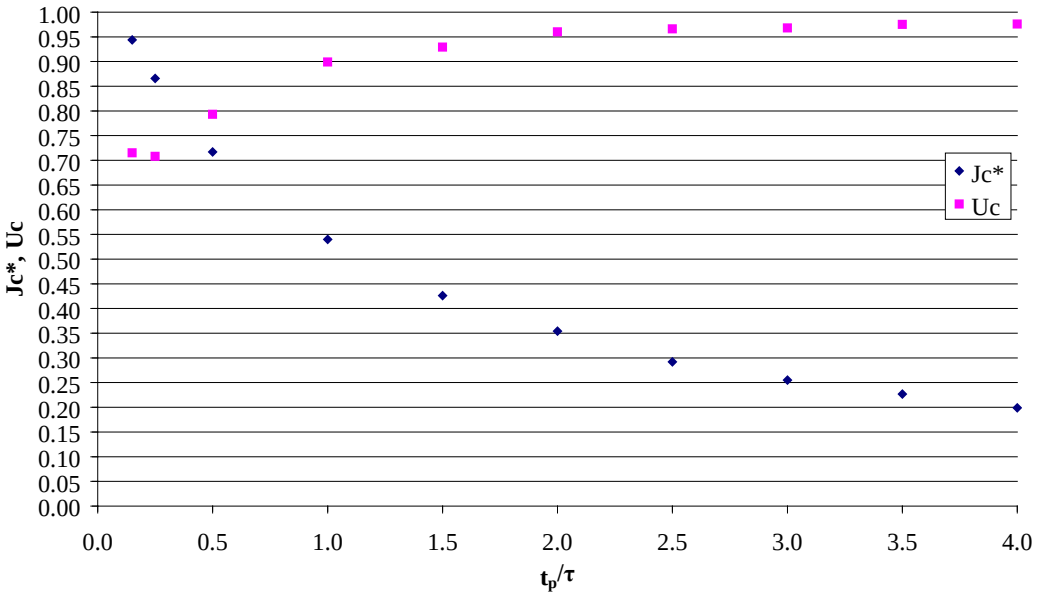

Figure C.10 The non-dimensional molecular flux J_C* and the compensated sublimation uniformity Uc, versus t_p/τ, for an injection time t_i = 0.4 s pulse flow experiments

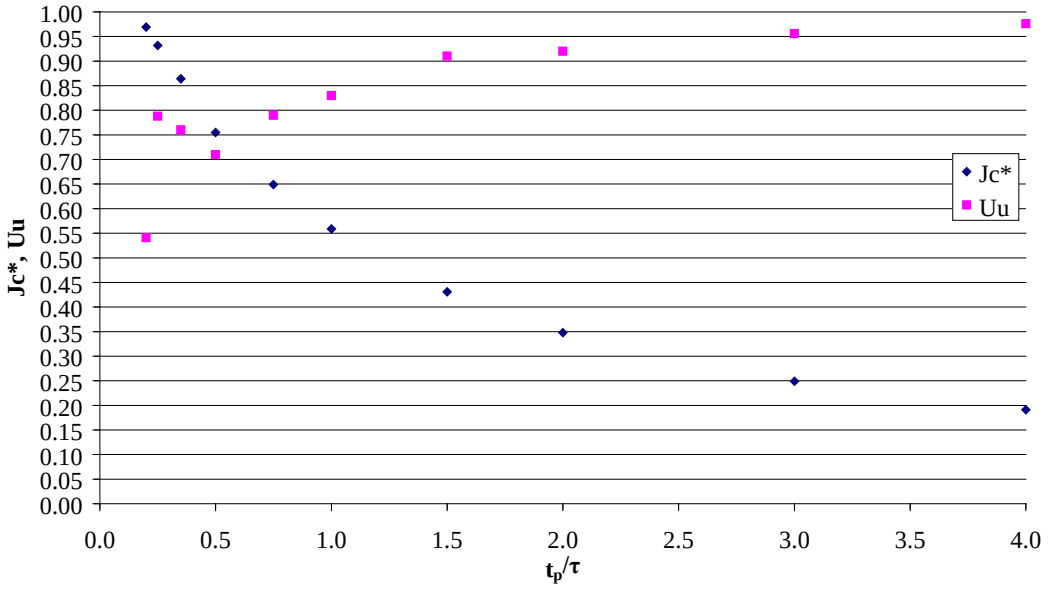

Figure C.11 The non-dimensional molecular flux J_C* and the uncompensated sublimation uniformity Uu, versus t_p/τ, for an injection time t_i= 0.8 s pulse flow experiments

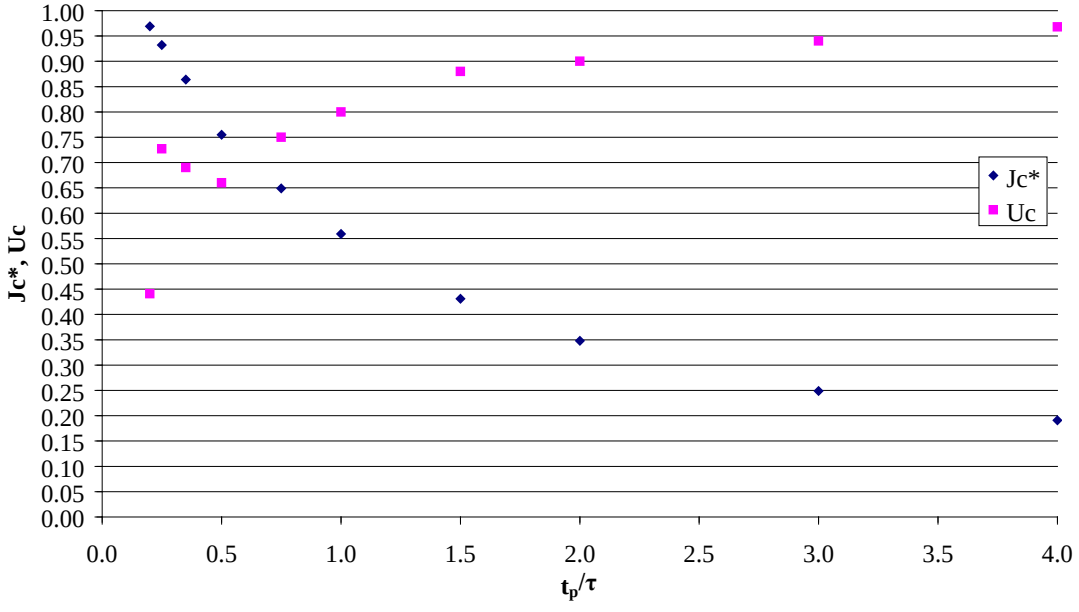

Figure C.12 The non-dimensional molecular flux J_C* and the compensated sublimation uniformity Uc, versus t_p/τ, for an injection time t_i = 0.8 s pulse flow experiments

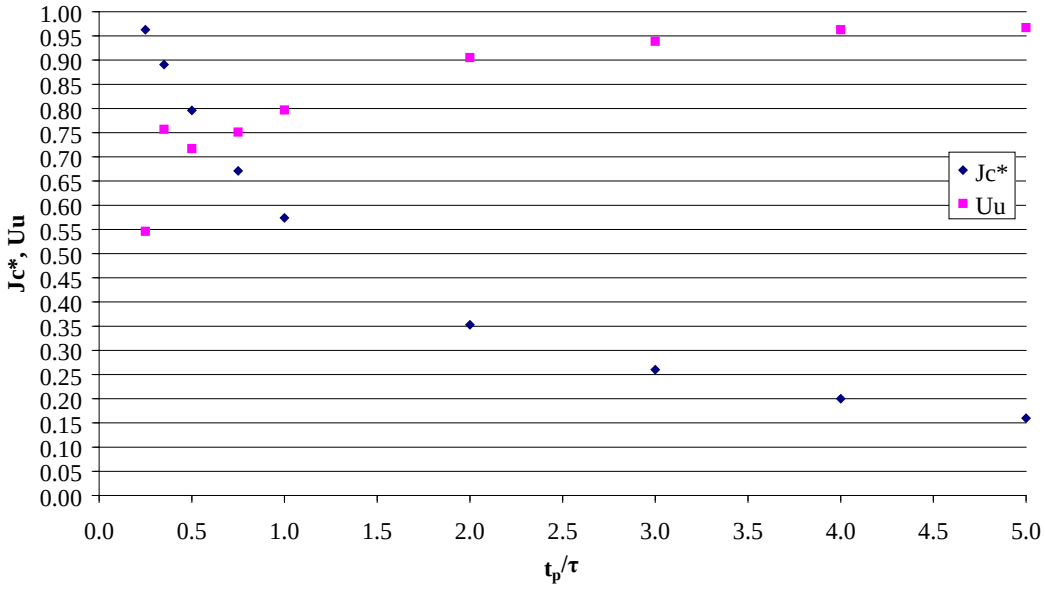

Figure C.13 The non-dimensional molecular flux J_C* and the uncompensated sublimation uniformity Uu, versus t_p/τ, for an injection time t_i = 1 s pulse flow experiments

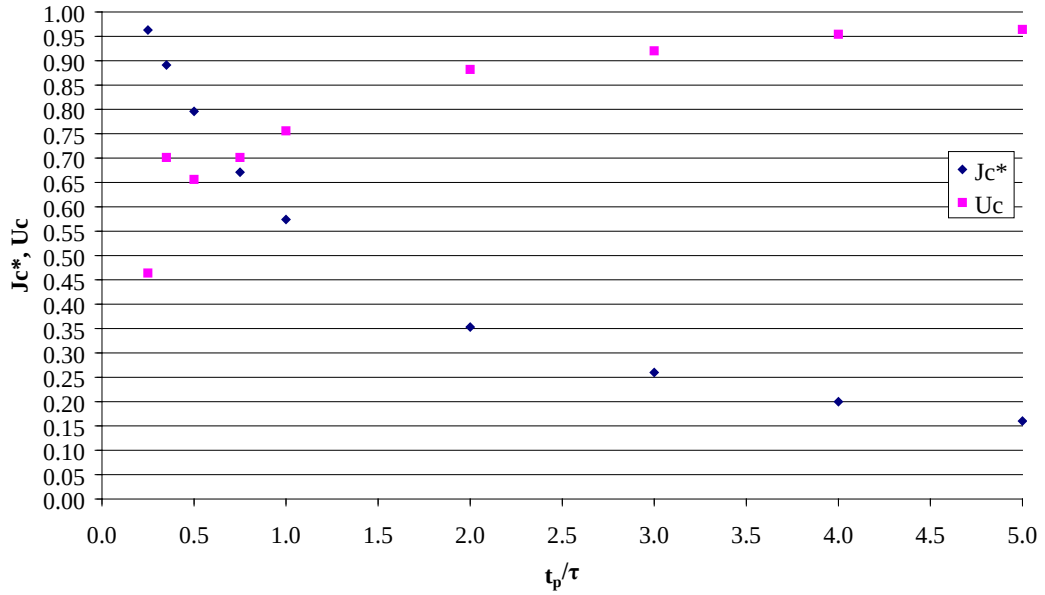

Figure C.14 The non-dimensional molecular flux J_C* and the compensated sublimation uniformity Uc, versus t_p/τ, for an injection time t_i = 1 s pulse flow experiments

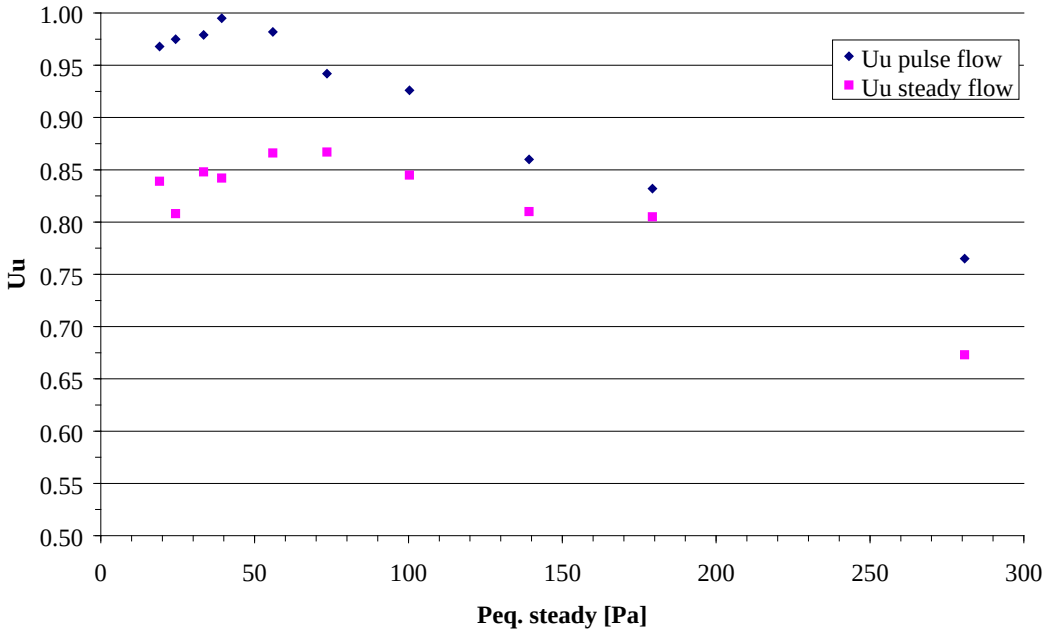

Figure C.15 Uncompensated sublimation uniformity Uu comparison between pulse flow experiments at an injection time t_i = 0.2 s, and equivalent steady flow experiments

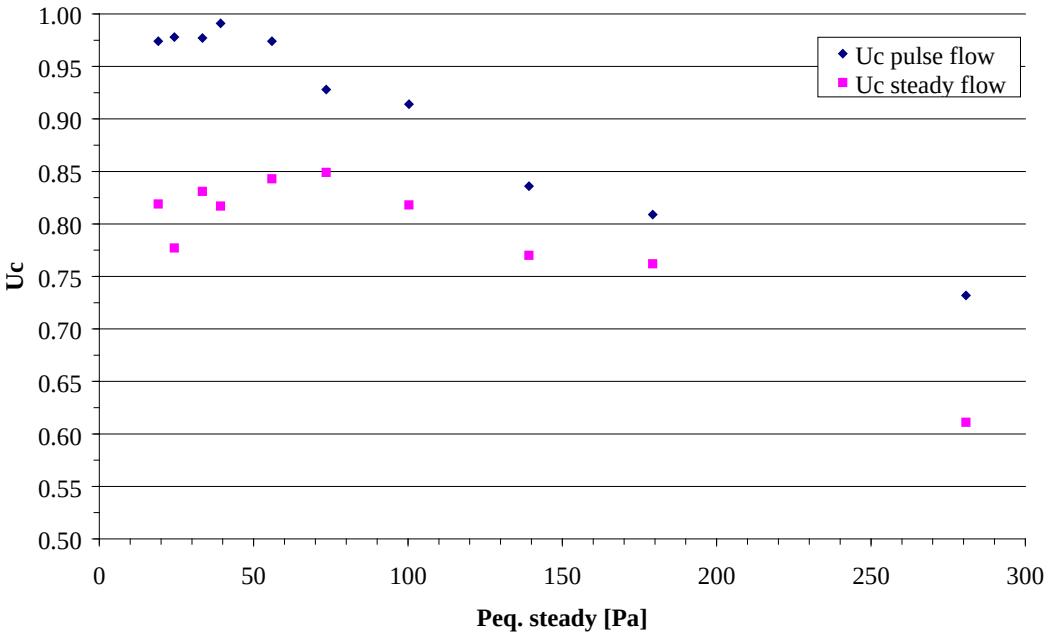

Figure C.16 Compensated sublimation uniformity Uc comparison between pulse flow experiments at an injection time t_i = 0.2 s and equivalent steady flow experiments

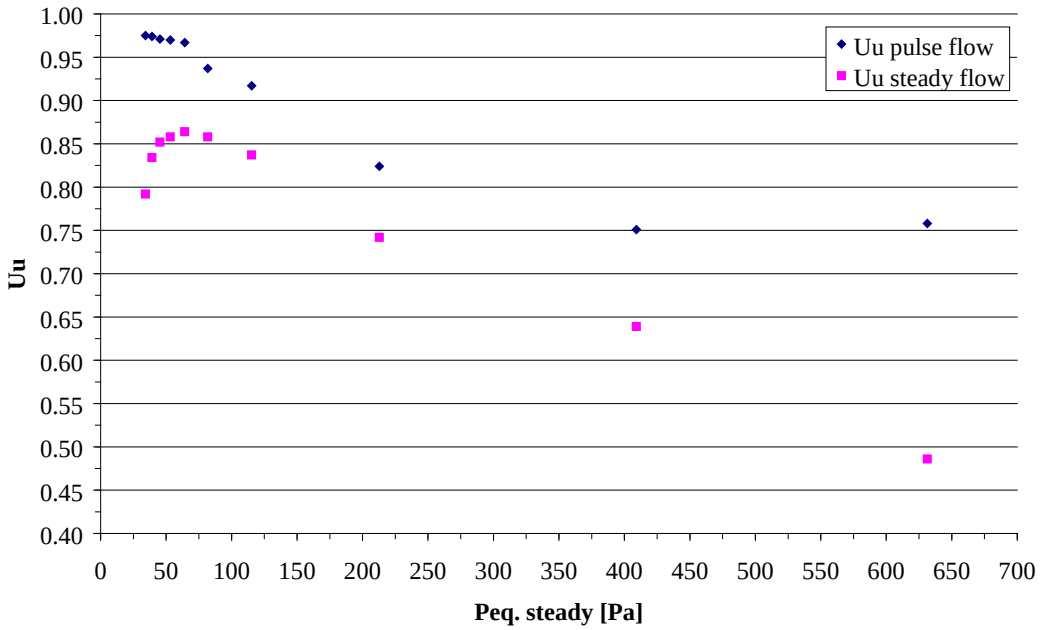

Figure C.17 Uncompensated sublimation uniformity Uu comparison between pulse flow experiments at an injection time t_i = 0.4 s, and equivalent steady flow experiments

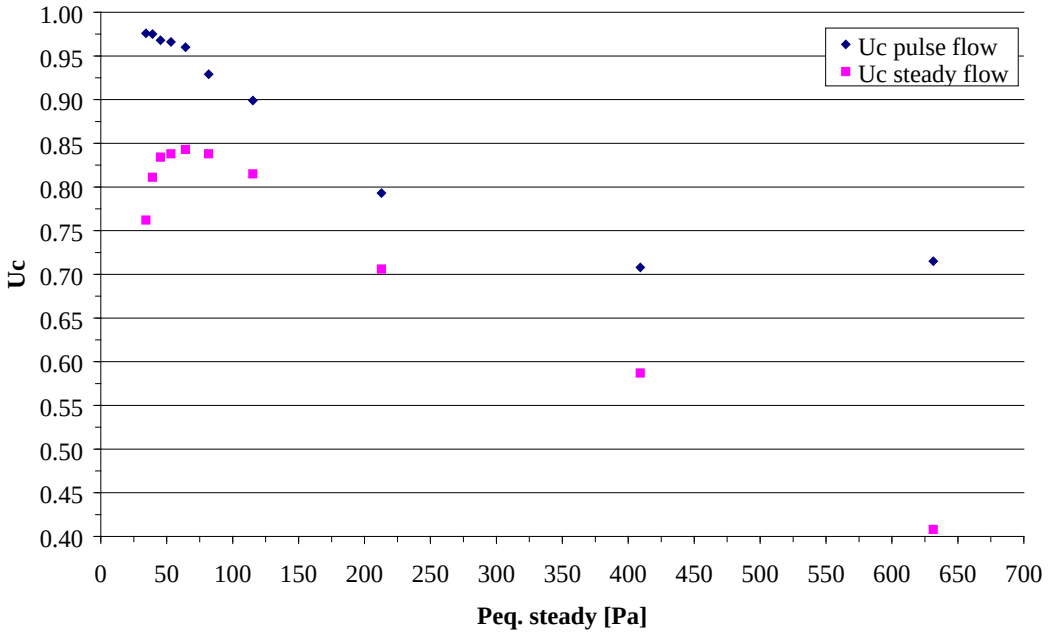

Figure C.18 Compensated sublimation uniformity Uc comparison between pulse flow experiments at an injection time t_i = 0.4 s and equivalent steady flow experiments

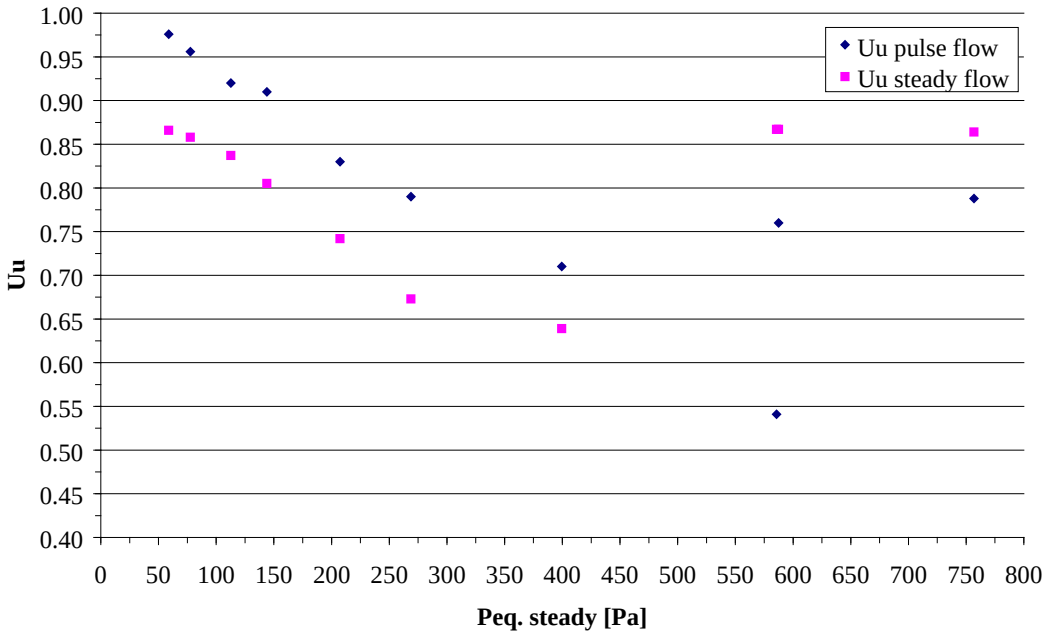

Figure C.19 Uncompensated sublimation uniformity Uu comparison between pulse flow experiments at an injection time t_i = 0.8 s, and equivalent steady flow experiments

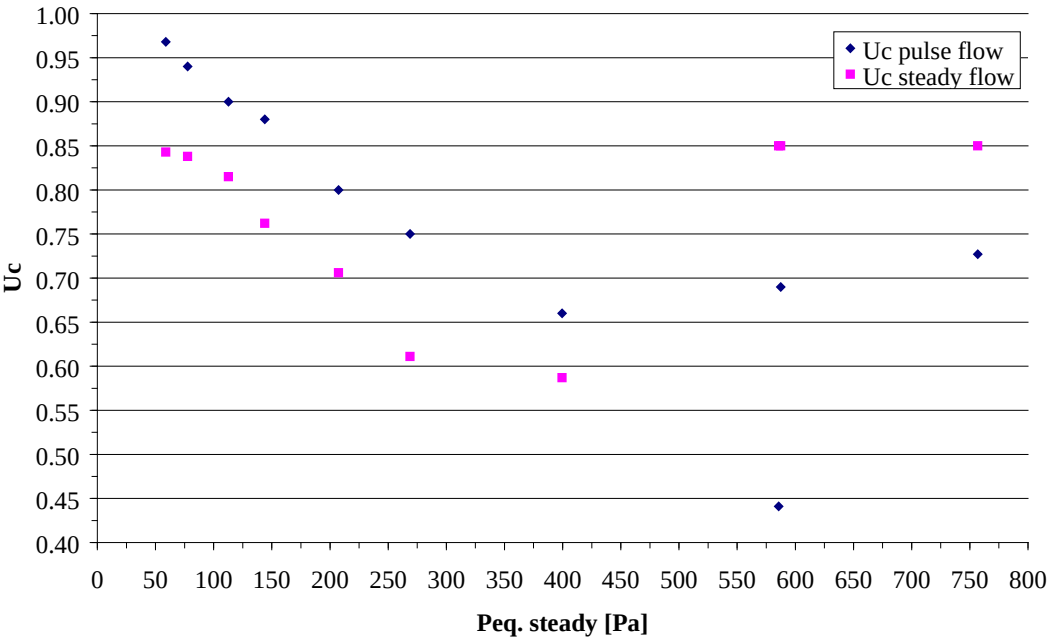

Figure C.20 Compensated sublimation uniformity Uc comparison between pulse flow experiments at an injection time t_i = 0.8 s and equivalent steady flow experiments

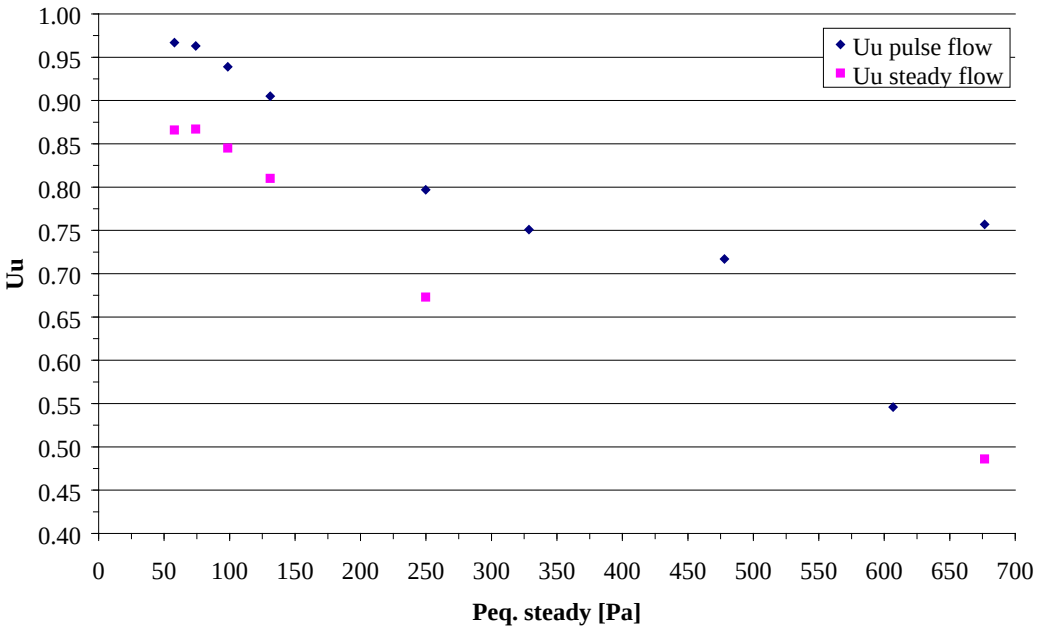

Figure C.21 Uncompensated sublimation uniformity Uu comparison between pulse flow experiments at an injection time t_i = 1 s, and equivalent steady flow experiments

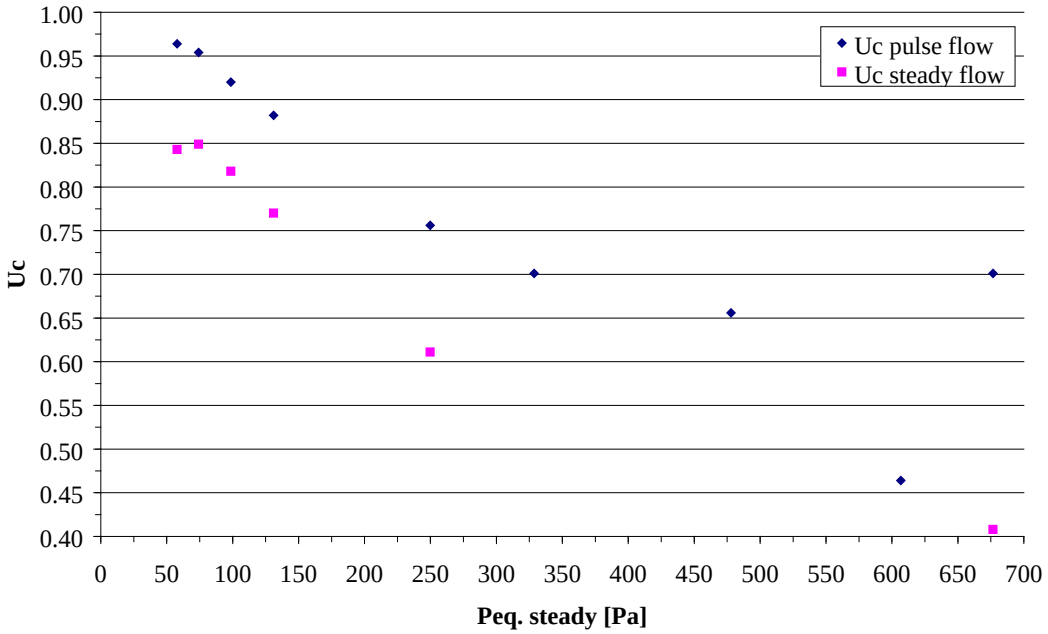

Figure C.22 Compensated sublimation uniformity Uc comparison between pulse flow experiments at an injection time t_i = 1 s and equivalent steady flow experiments

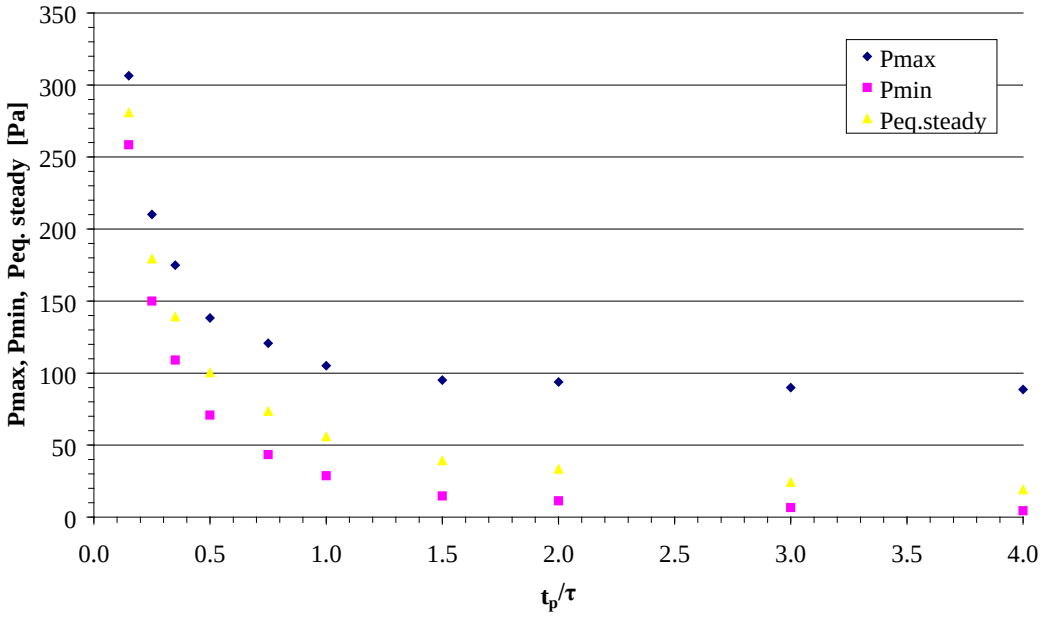

Figure C.23 Reactor maximum, minimum, and equivalent pressures for value of t_p increasing from 0.15τ, to 4τ, at an injection time t_i = 0.2 s pulse flow experiments

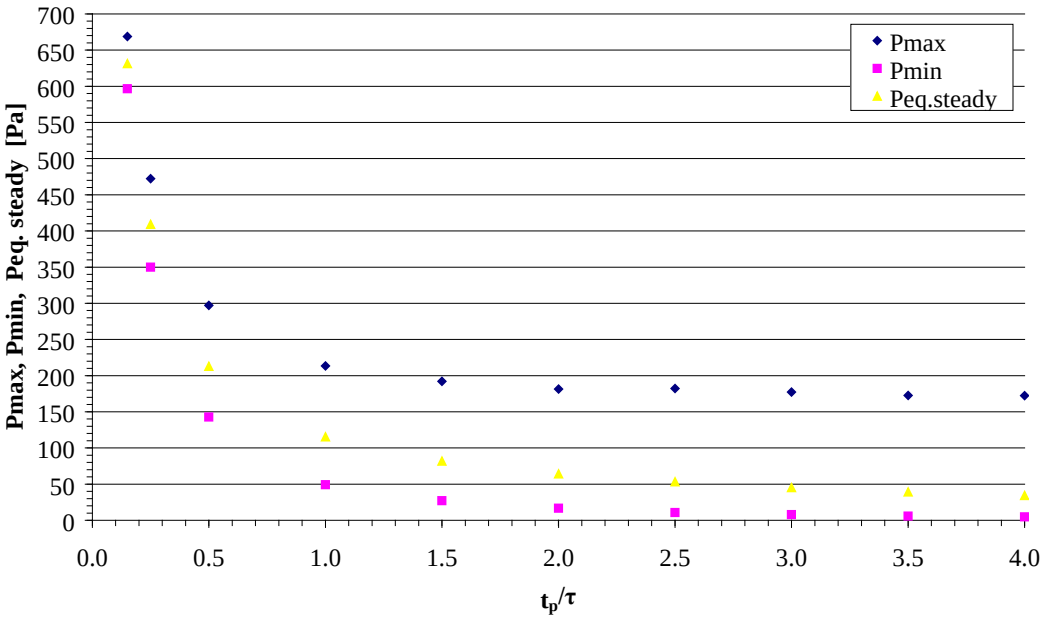

Figure C.24 Reactor maximum, minimum, and equivalent pressures for value of tp increasing from 0.15τ, to 4τ, at an injection time t_i = 0.4 s pulse flow experiments

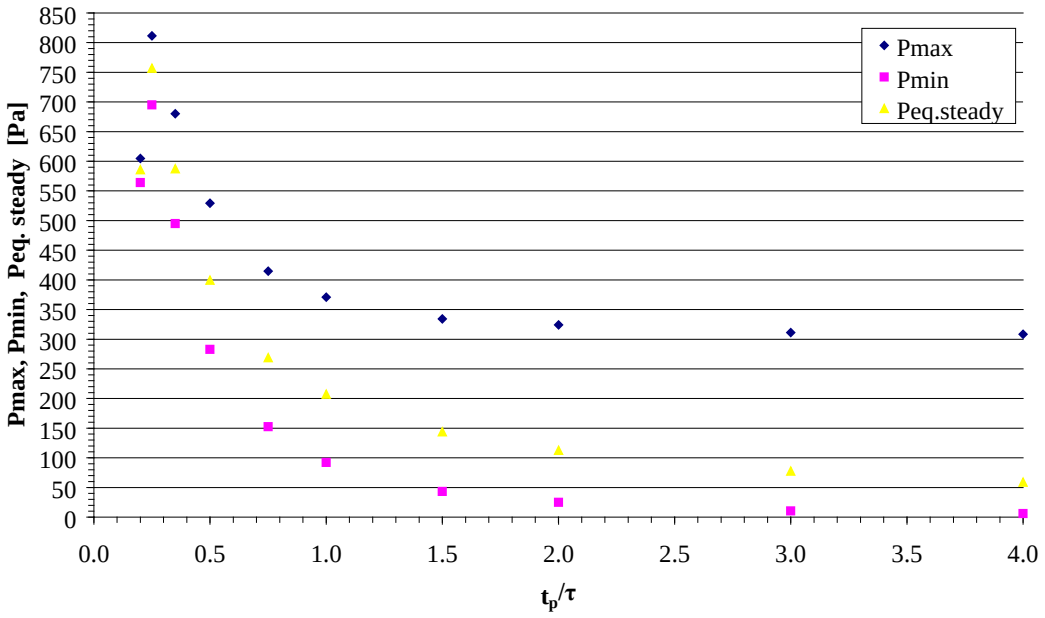

Figure C.25 Reactor maximum, minimum, and equivalent pressures for value of t_p increasing from 0.2τ, to 4τ, at an injection time $t_i = 0.8$ s pulse flow experiments

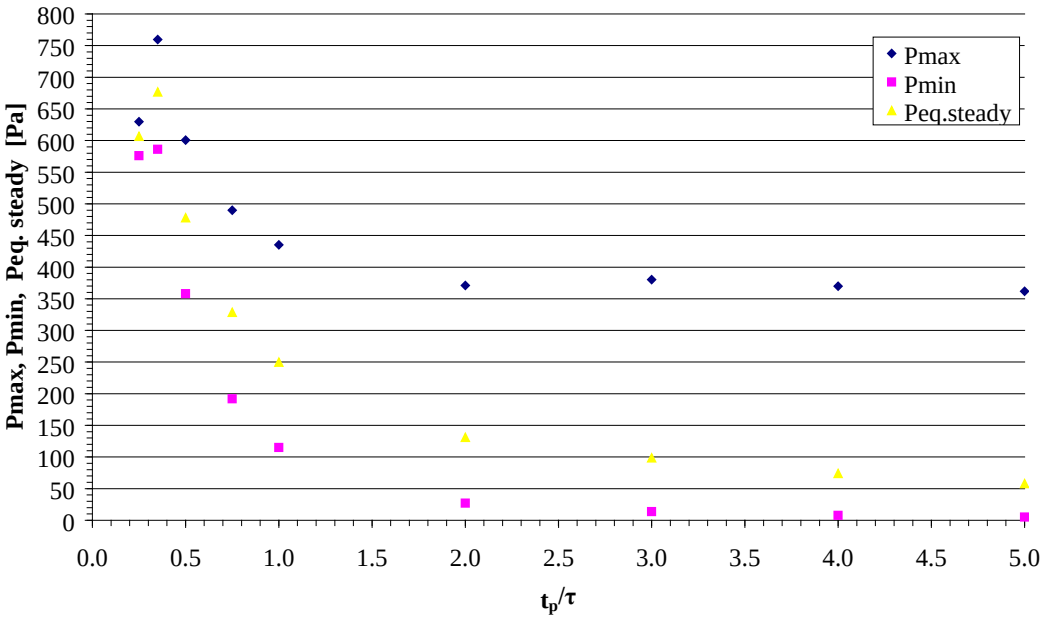

Figure C.26 Reactor maximum, minimum, and equivalent pressures for value of t_p increasing from 0.25τ, to 5τ, at an injection time $t_i = 1$ s pulse flow experiments

C.2 Reactor volume flow field uniformity as a function of the pulse cycle maximum pressure

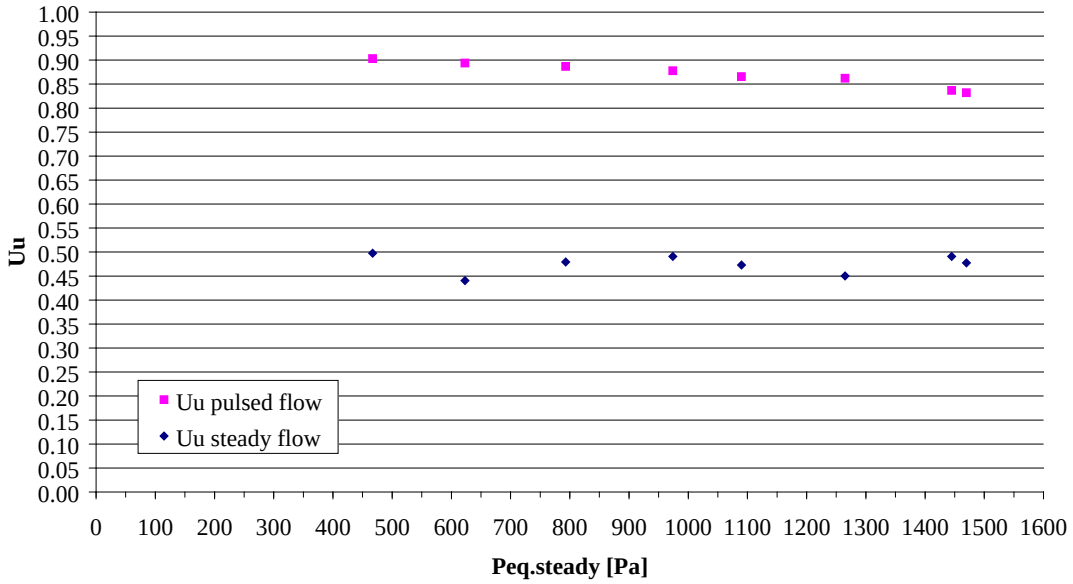

Figure C.27 Uncompensated sublimation uniformity Uu comparison between pulse flow experiments and equivalent steady flow experiments for increased reactor pressures

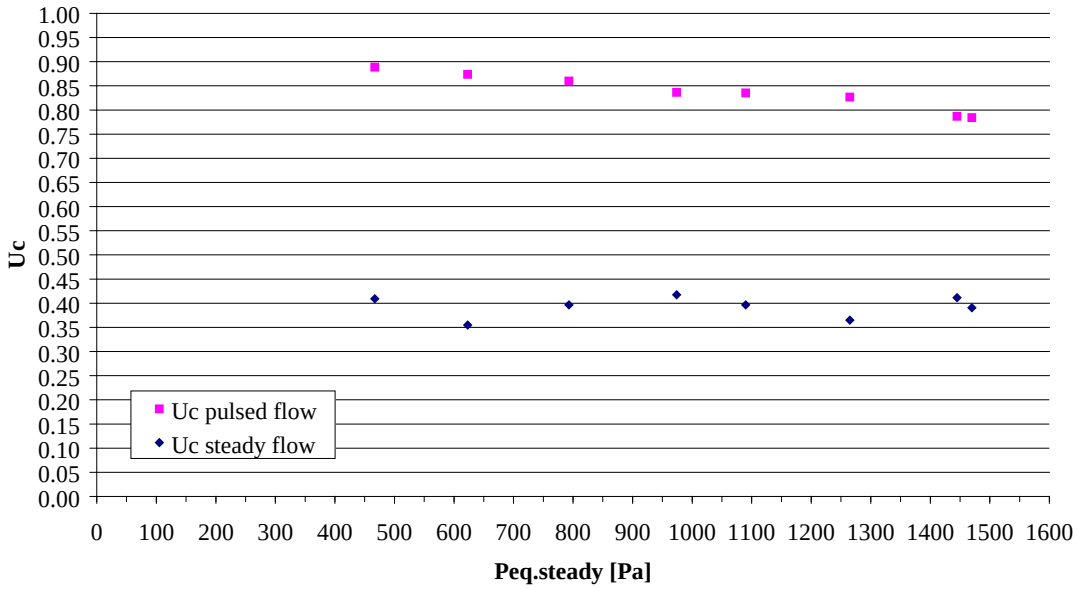

Figure C.28 Compensated sublimation uniformity Uc comparison between pulse flow experiments and equivalent steady flow experiments for increased reactor pressures

C.3 Stacked wafer flow uniformity

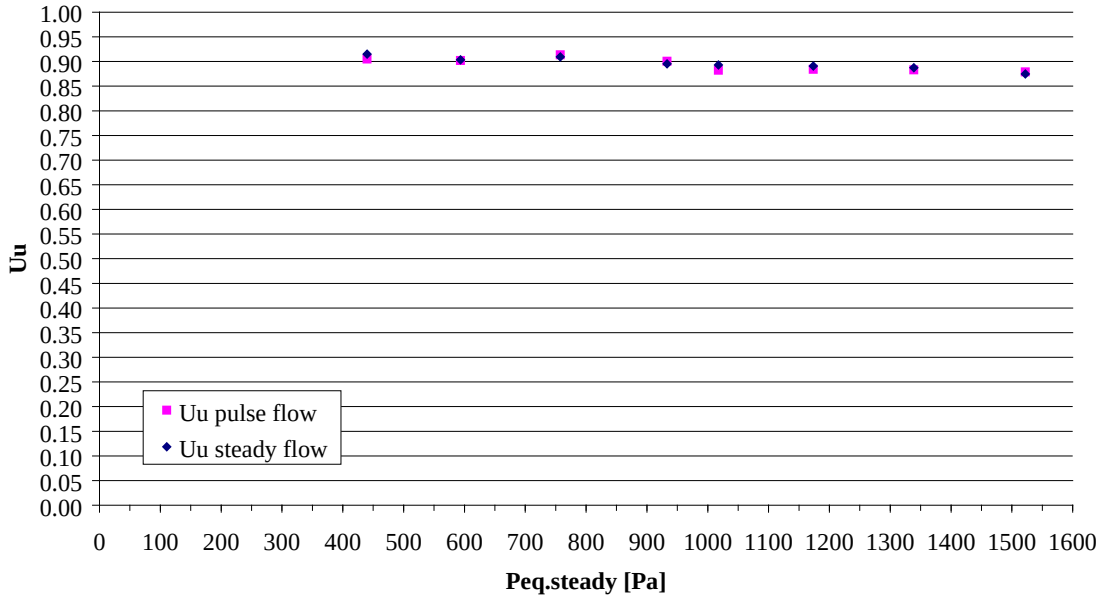

Figure C.29 Uncompensated sublimation uniformity Uu of samples positioned between horizontal wafers, comparison between pulse flow experiments and equivalent steady flow experiments for increased reactor pressures

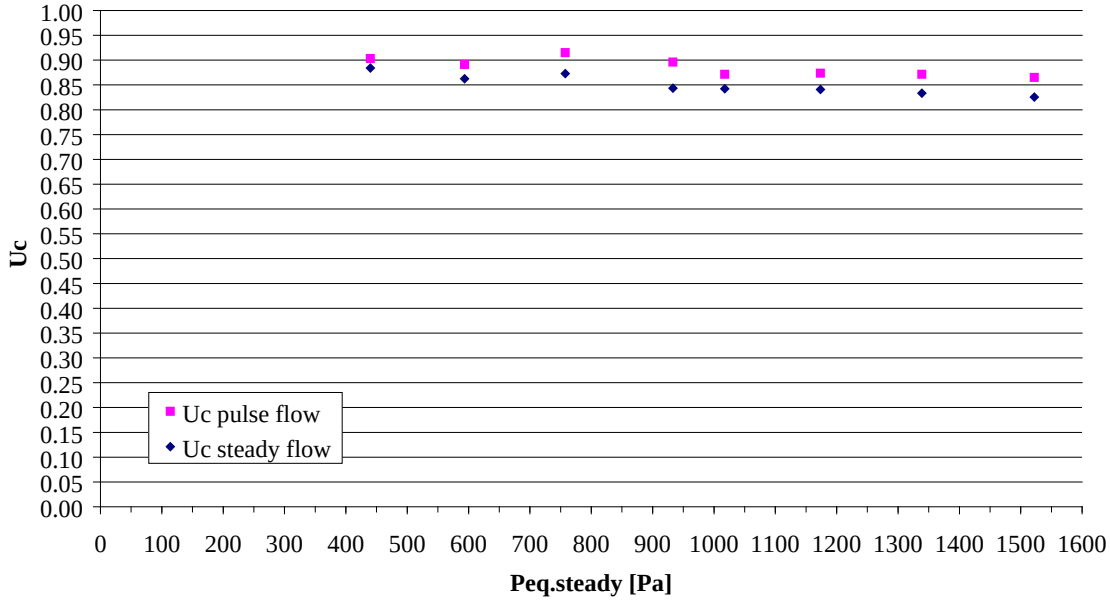

Figure C.30 Compensated sublimation uniformity Uc of samples positioned between horizontal wafers, comparison between pulse flow experiments and equivalent steady flow experiments for increased reactor pressures